COMPUTATIONAL STUDIES OF PYRITE- AND MARCASITE-TYPE STRUCTURES;

$OsAs_2$, OsS_2, $RuAs_2$ AND RuS_2

By

RAPETSOA MAMPHULE JOHANNES

RESEARCH THESIS

Submitted in fulfilment of the requirements for the degree of

MASTERS OF SCIENCE

in

PHYSICS

in the

FACULTY OF SCIENCE and AGRICULTURE

(School of Physical and Mineral Sciences)

at the

UNIVERSITY OF LIMPOPO

SUPERVISOR: Prof P.E. Ngoepe

Co-Supervisor: Dr H.R. Chauke

2009

ABSTRACT

Calculations were carried out on transition-metal sulphides (TMS) and transition-metal arsenides (TMA), in both pyrite- and marcasite-type structures, using plane-wave (PW) pseudopotential methods within density functional theory (DFT) in the local density approximation (LDA). The structural, electronic and optical properties for both pyrite- and marcasite-type structures (naturally occurring and converted) have been investigated. The equilibrium lattice parameters were investigated and are in good agreement with the experimental values. The heats of formation calculations predict that the naturally occurring pyrite- and marcasite-type structures are more stable than the converted ones. In particular, the calculated pyrite-type RuS_2 compares well to the experimental value (with energy difference of 0.381 eV/atom). The bulk modulus and elastic properties were calculated. The predicted anisotropic ratio shows that the naturally occurring pyrite- and marcasite-type structures are more stable than the converted ones.

Moreover, the electronic density of states and band structure calculations reveal that most compositions shows semiconducting behaviour except for the converted pyrite-type structures, i.e $OsAs_2$ and $RuAs_2$ where a metallic behaviour was observed. The electronic charge density and charge density difference show charge accumulation on bonding atoms, predicting the charge gain/ loss and nature of bonding to be covalent/ weak ionic between the atoms.

Lastly, optical properties are computed at equilibrium and predict that naturally occurring structures have lower absorption and reflectivity than the converted structures. At different pressures ranging from -10 GPa to 10 GPa, the absorption and reflectivity spectra show a shift from the 0 GPa spectrum for all the structures.

DECLARATION

I declare that the thesis hereby submitted to the University of Limpopo (Turfloop Campus), for the degree of Master of Science in physics has not previously been submitted by me for a degree at this or any other university; that it is my own work in design and in execution, and that all material contained herein has been duly acknowledged.

M.J Rapetsoa(Mr) **2009**

[redacted]

ACKNOWLEDGEMENTS

I would like to pass my sincere gratitude to supervisor Professor P.E. Ngoepe for the guidance and numerous discussions during this research process. I wish to thank Dr H.R. Chauke for the discussions and support he offered to me throughout the research.

I would like to thank my fellow students in the Materials Modelling Centre (MMC) for their good working relationship, encouragement and interest during this research.

I am grateful to the National Research Foundation (NRF) for the financial support offered to me for this Master of Science (MSc) degree research.

I also thank my parents and all members of my family for their incredible support, encouragement and patience throughout my study.

DEDICATION

This work is dedicated to:

My beloved father
Sello David Rapetsoa

My beloved mother
Maleho Mamasilo Rapetsoa

TABLE OF CONTENTS

CHAPTER 1 1

INTRODUCTION 1

1.1 General background 1

1.2 Structural aspects 3

  1.2.1 Pyrite-type 3

  1.2.2 Marcasite-type 6

1.3 Literature review 7

1.4 Intentions of the study 10

1.5 Outline…. 11

CHAPTER 2 13

METHODOLOGY 13

2.1 Density functional theory 13

  2.1.1 Local density approximation 16

  2.1.2 Generalized gradient approximation 19

2.2 Plane-wave pseudopotential method 20

  2.2.1 Plane-wave basis 20

  2.2.2 The pseudopotential method 21

  2.2.3 Brillouin zone sampling 24

  2.2.4 CASTEP 25

  2.2.5 VASP 26

  2.2.6 Convergence of energy cut-off and k-points sampling 27

CHAPTER 3 31

STRUCTURAL PROPERTIES 31

3.1 Equilibrium geometry relaxation 31

3.2 Heats of formation 34

3.3 Internal parameter relaxation 35

3.4 Equilibrium bond lengths 35

3.5 Equation of states (EOS) and elastic constants 37

3.6 Pressure dependence of lattice constants. 42

    3.6.1 Lattice parameters at applied pressure 42

    3.6.2 Internal parameters 45

    3.6.3 Bond length at applied pressure 48

CHAPTER 4 51

ELECTRONIC PROPERTIES 51

4.1 Density of states and band structures at equilibrium 51

4.2 Charge density 62

CHAPTER 5 68

OPTICAL PROPERTIES 68

Background… 68

5.1 Absorption and reflectivity spectra 70

5.2 Influence of pressure on the optical properties. 77

CHAPTER 6 81

SUMMARY AND CONCLUSIONS 81

APPENDIX A 84

REFERENCES 85

LIST OF FIGURES

Figure 1.1: (a) A rock containing yellowish pyrite [http://www.minerals.net /mineral/sulfides/pyrite] and (b) a rock containing pale yellow marcasite [http://en.wikipedia.org/wiki/marcasite]..2

Figure 1.2: Crystal structure of (a) cubic pyrite MS_2 and (b) orthorhombic marcasite MAs_2 (where M is taken as Ru or Os)..5

Figure 2.1: A comparison of the methodology for solving the many-body Schrodinger equation and effective one-electron Kohn-Sham equations respectively [Mattsson et al, 2005; Chauke, 2005]...17

Figure 2.2: Comparison of a wavefunction in the coulomb (all-electron) potential of the nucleus (blue) to the one in the pseudo-potential (red). The real and the pseudo wavefunction and potentials match above a certain cut-off radius r_c [Payne et al, 1992]..23

Figure 2.3: Total energy per atom versus energy cut-off for pyrite OsS_2 and marcasite $OsAs_2$ (CASTEP calculation)...28

Figure 2.4: Total energy per atom versus k-points for pyrite OsS_2 and marcasite $OsAs_2$ (CASTEP calculation); 10 = 10 x 10 x 10 etc. 30

Figure 3.1: Total energy per atom against volume per atom for pyrite- and marcasite-type structures: (a) $RuAs_2$, (b) RuS_2, (c) $OsAs_2$ and (d) OsS_2....................................32

Figure 3.2: Equations of states for pyrite- and marcasite-type (a) $OsAs_2$ and OsS_2, and (b) $RuAs_2$ and RuS_2 structures..39

Figure 3.3: Lattice parameter as a function of applied hydrostatic pressure for the pyrite-type structures. 43

Figure 3.4: Lattice parameter as a function of applied hydrostatic pressure for the marcasite-type structures. The lattice parameter a, b and c are indicated for each structure explicitly. 44

Figure 3.5: Internal parameter u as a function of pressure for the pyrite-type structures. 46

Figure 3.6: Internal parameters u and v as a function of pressure for the marcasite-type structures. 47

Figure 3.7: Bond length as a function of pressure for the pyrite- and marcasite-type structures. 50

Figure 4.1: (a) Total and partial density of states and (b) energy band structure for pyrite-type $OsAs_2$. The Fermi level is taken as energy zero ($E_F = 0$). 52

Figure 4.2: (a) Total and partial density of states and (b) energy band structure for marcasite-type $OsAs_2$. The Fermi level is taken as energy zero ($E_F = 0$). 52

Figure 4.3: (a) Total and partial density of states and (b) energy band structure for pyrite-type OsS_2. The Fermi level is taken as energy zero ($E_F = 0$). 54

Figure 4.4: (a) Total and partial density of states and (b) energy band structure for marcasite-type OsS_2. The Fermi level is taken as energy zero ($E_F = 0$). 54

Figure 4.5: (a) Total and partial density of states and (b) energy band structure for pyrite-type $RuAs_2$. The Fermi level is taken as energy zero ($E_F = 0$). 56

Figure 4.6: (a) Total and partial density of states and (b) energy band structure for marcasite-type $RuAs_2$. The Fermi level is taken as energy zero ($E_F = 0$). 56

Figure 4.7: (a) Total and partial density of states and (b) energy band structure for pyrite-type RuS_2. The Fermi level is taken as energy zero ($E_F = 0$). 58

Figure 4.8: (a) Total and partial density of states and (b) energy band structure for marcasite-type RuS_2. The Fermi level is taken as energy zero ($E_F = 0$). 58

Figure 4.9: Total density of states for pyrite- and marcasite-type structures. The Fermi level is taken as energy zero ($E_F = 0$). 61

Figure 4.10: Electronic (a) charge density and (b) charge density difference for pyrite-type RuS_2 projected in the (110) plane. 64

Figure 4.11: Electronic (a) charge density and (b) charge density difference for pyrite-type $OsAs_2$ projected in the (110) plane. 64

Figure 4.12: Electronic (a) charge density and (b) charge density difference for marcasite-type $OsAs_2$ projected in the (001) plane...66

Figure 4.13: Electronic (a) charge density and (b) charge density difference for marcasite-type OsS_2 projected in the (001) plane. 66

Figure 5.1: Absorption spectra in units of cm^{-1} against frequency (eV) for pyrite-type structures. 71

Figure 5.2: Reflectivity spectra in units of 10^2 % against frequency (eV) for pyrite-type structures. 73

Figure 5.3: (a) Absorption coefficient in units of cm^{-1} and (b) reflectivity in units of 10^2 % against frequency energy for the marcasite-type...76

Figure 5.4: (a) Absorption coefficient in units of cm^{-1} and (b) reflectivity in units of 10^2 % against frequency for the pyrite-type at applied hydrostatic pressures. 78

Figure 5.5: (a) Absorption coefficient in units of cm^{-1} and (b) reflectivity in units of 10^2 % against frequency for the marcasite-type at applied hydrostatic pressures. 80

LIST OF TABLES

Table 1.1: General atomic positions for the pyrite- and marcasite-type structures 4

Table 3.1: Equilibrium lattice parameters, volumes and heats of formation, ΔH_f for pyrite- and marcasite-type structures. The experimental value is given in parenthesis. 33

Table 3.2: Equilibrium internal parameters and bond lengths for pyrite- and marcasite-type compounds. 36

Table 3.3: Elastic constants, Bulk modulus (B), Young's modulus (Y) and Shear modulus (C) of pyrite- and marcasite-type structures for TMA and TMS. 40

Table 4.1: Energy band gaps for TMA and TMS using CASTEP code, compared with available data where possible...59

CHAPTER 1

INTRODUCTION

In this introductory chapter, we give a general background on the transition-metal sulphide (TMS) and transition-metal arsenide (TMA) systems. The structural aspects based on the pyrite- and marcasite-type, literature review, the objectives of the study and lastly the outline of the thesis will be given.

1.1 General background

The pyrite group minerals of transition-metal dichalcogenides MX_2 (M = Au, Co, Cu, Fe, Mn, Ni, Os, Pd, Pt, Ru and X = As, Bi, S, Sb, Se, Te) and the marcasite group minerals MX_2 (M = Fe, Co, Ni, Ru, Os and X = S, Se, Te, As, Sb) have undergone intensive investigations previously [Wilson, 1972; Goodenough, 1972; Bullett, 1982; Raybaud et al 1997]. The FeS_2 is the naturally occurring phase and the most common metal sulphide and crystallizes into two forms i.e. cubic pyrite and orthorhombic marcasite. Pyrite thus far is the most common and the most often mistaken for gold among other shiny brassy yellow minerals and is a favourite among rock collectors because of its beautiful luster and interesting crystals. It is so common in the earth’s crust that it is found in almost every possible environment [http://www.minerals.net /mineral/sulfides/pyrite]. On the other hand, marcasite is often mistakenly confused with pyrite, but it is lighter and more brittle. Primarily, marcasite can be found in low temperature hydrothermal veins and it is pale yellow to almost white on fresh surfaces [http://www.minerals.net/mineral/sulfides/marcasite]. The rock containing pyrite from one of the South African mines and marcasite rock are shown in Figure 1.1. The other known TMS are Erlichmanite (OsS_2) and Laurite (RuS_2) classified as the pyrite-type

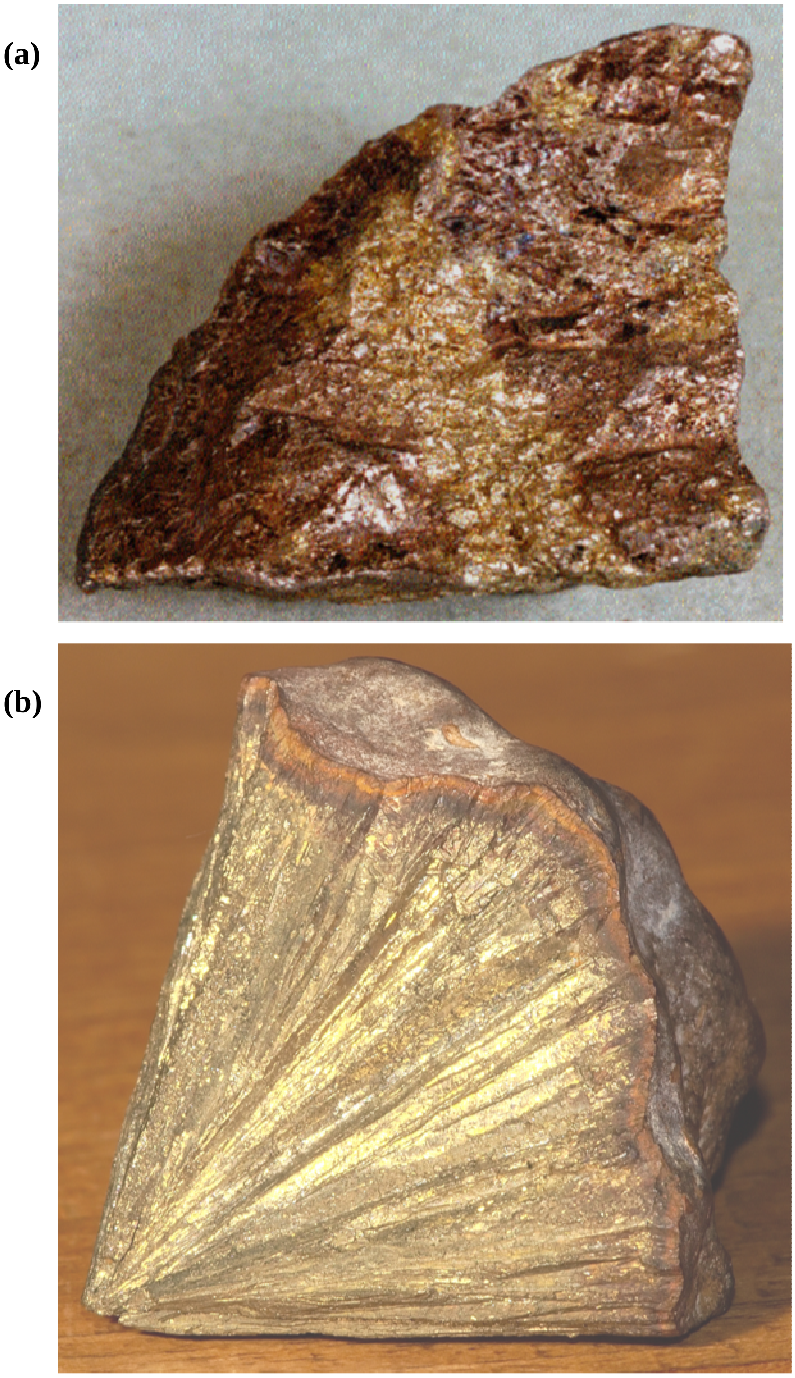

Figure 1.1: (a) A rock containing yellowish pyrite [http://www.minerals.net /mineral/sulfides/pyrite] and (b) a rock containing pale yellow marcasite [http://en.wikipedia.org/wiki/marcasite].

minerals and among the TMA is the Omeiite ($OsAs_2$) and Anduoite ($RuAs_2$) classified as the marcasite-type minerals.

However, RuS_2 belongs to one of the families of transition metal dichalcogenides crystallizing in the pyrite structure and is an interesting material from both fundamental and technological point of view [Sutarno, 1967]. It went through hydrotreating catalysts and appeared to be one of the most promising new structures.

Unfortunately, there is little information about these systems from literature. In this thesis, we will focus on these systems, in particular the structural stabilities which are necessary to clarify why RuS_2 exists as pyrite not as marcasite and their structural aspects are discussed briefly in the next section as pyrite- and marcasite-type.

We will also investigate the naturally occurring structures against the converted pyrite- and marcasite-type structures with respect to their lowest energies and properties.

In the next section, we discuss the structural aspects of TMS and TMA in pyrite- and marcasite-type.

1.2 Structural aspects

1.2.1 Pyrite-type

The pyrite-type OsS_2 and RuS_2 like FeS_2, have the cubic crystal structure with space group T_h^6 ($Pa\bar{3}$) and space group number 205. The structure is characterized with the four metal atoms located at 4(a) positions: (0,0,0);$(0,\frac{1}{2},\frac{1}{2})$; $(\frac{1}{2},0,\frac{1}{2})$ and $(\frac{1}{2},\frac{1}{2},0)$ and eight S atoms in the 8(c) positions: $\pm(u, u, u)$; $\pm(u+\frac{1}{2},\frac{1}{2}-u,-u)$; $\pm(-u, u+\frac{1}{2},\frac{1}{2}-u)$ and $\pm(\frac{1}{2}-u,-u, u+\frac{1}{2})$. There are additional symmetry positions (24d) (x, y, z) where $u \approx 0.388$ for $0 \leq x, y, z \leq \frac{1}{2}$ [Hann, 1989]. Each TM atom is coordinated by six S atoms in a slightly distorted octahedron, and each S atom is tetrahedrally coordinated to three TM atoms and its dimer pair [Sithole et al, 2003]. The crystal structure of the pyrite-type is shown in Figure 1.2 and the crystal structural positions are given in table 1.1. The OsS_2 and RuS_2 are metallic in nature with comparable lattice constants of 5.6196 Å and 5.6095 Å, respectively [Sutar, 1967]. These minerals have the S atoms appearing in S_2 pairs in the structure and gives strong S-S bonding like the FeS_2 which has the dimer pair S-S, in contrast to other minerals like MoS_2 where only weak Van der Waals S-S bonds between the S-Mo-S sandwiches in the layered structure exist [Grillo et al, 1999]. RuS_2 and OsS_2 have the highest catalytic activity as pyrite-type disulphides [Raybaud et al, 1997] with RuS_2 being the most active catalyst for the hydrodesulfurization (HDS) of thiophene [Lacroix et al, 1989].

Table 1.1: General atomic positions for the pyrite- and marcasite-type structures

	Space group	**Atomic positions***
Pyrite	$Pa\bar{3}$	4(a): $(0,0,0);(0,\frac{1}{2},\frac{1}{2});(\frac{1}{2},0,\frac{1}{2})$ and $(\frac{1}{2},\frac{1}{2},0)$ 8(c): $\pm(u,u,u); \pm(u+\frac{1}{2},\frac{1}{2}-u,-u); \pm(-u,u+\frac{1}{2},\frac{1}{2}-u)$ and $\pm(\frac{1}{2}-u,-u,u+\frac{1}{2})$ 24(d): $\pm(u,v,w); \pm(w,u,v); \pm(v,w,u); \pm(-u+\frac{1}{2},-v,w+\frac{1}{2});$ $\pm(w+\frac{1}{2},-u+\frac{1}{2},-v); \pm(-v,w+\frac{1}{2},-u+\frac{1}{2}); \pm(v+\frac{1}{2},-w+\frac{1}{2},-u);$ $\pm(-w+\frac{1}{2},-u,v+\frac{1}{2}); \pm(-u,v+\frac{1}{2},-w+\frac{1}{2}); \pm(u+\frac{1}{2},-v+\frac{1}{2},-w);$ $\pm(-w,u+\frac{1}{2},-v+\frac{1}{2})$ and $\pm(u+\frac{1}{2},-v+\frac{1}{2},-w)$
Marcasite	*Pnnm*	2(a): (000) and $(\frac{1}{2},\frac{1}{2},\frac{1}{2})$ 2(c): $(0,\frac{1}{2},0)$ and $(\frac{1}{2},0,\frac{1}{2})$ 2(d): $(0,\frac{1}{2},\frac{1}{2})$ and $(\frac{1}{2},0,0)$ 4(g): $(u,v,0); (-u,-v,0); (-u+\frac{1}{2},v+\frac{1}{2},\frac{1}{2})$ and $(u+\frac{1}{2},-v+\frac{1}{2},\frac{1}{2})$ 8(h): $\pm(u,v,w); \pm(-u,-v,w); \pm(-u+\frac{1}{2},v+\frac{1}{2},-w+\frac{1}{2})$ and $\pm(u+\frac{1}{2},-v+\frac{1}{2},-w+\frac{1}{2})$

* [Hann, 1989]

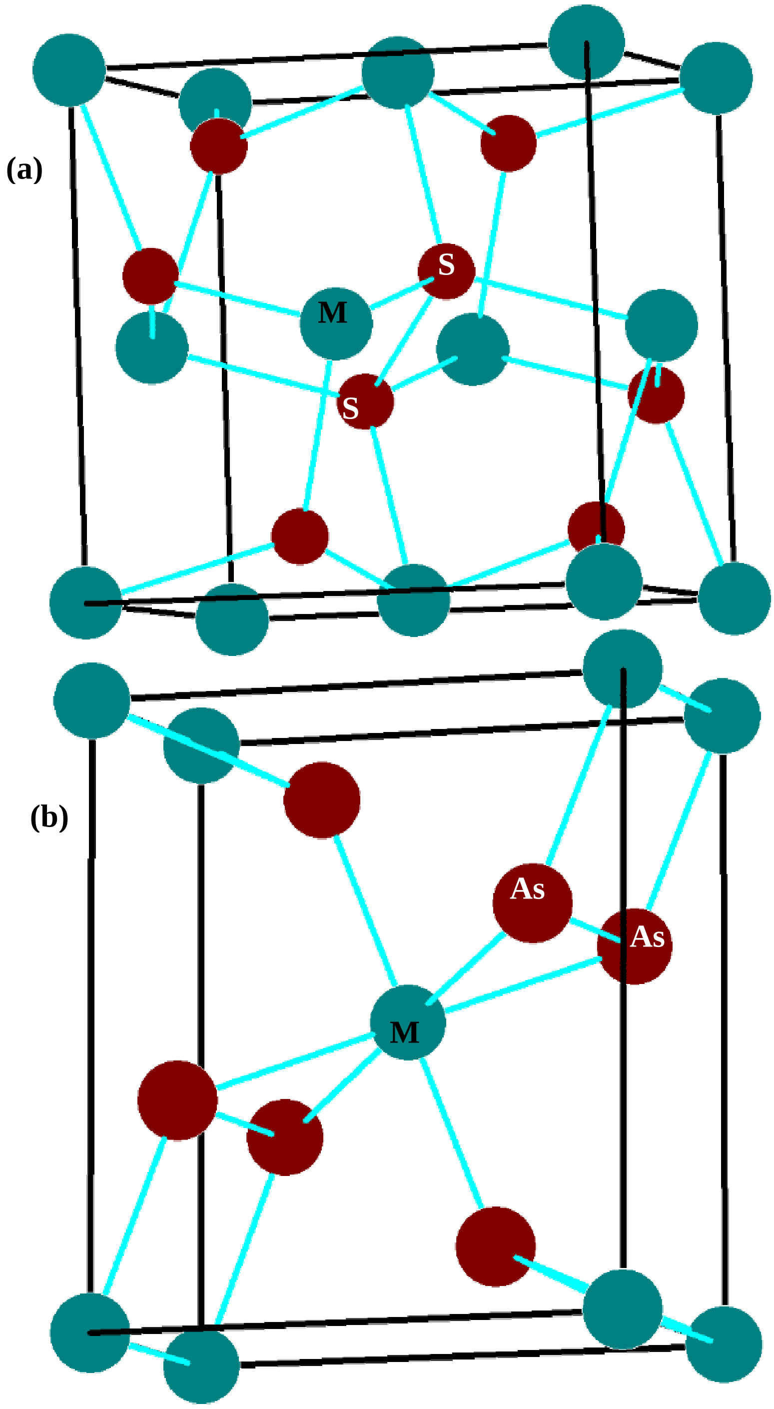

Figure 1.2: Crystal structure of (a) cubic pyrite MS_2 and (b) orthorhombic marcasite MAs_2 (where M is taken as Ru or Os).

This high reactivity in RuS_2 has driven a large interest in the fundamental understanding of its catalytic behaviour [Grillo et al, 1999]. However, bond strength has been redefined as the cohesive energy of the TMS per TM-S bond and reported that TMS with too low or too high TM-S bond strengths are practically inactive, whereas those with intermediate TM-S bond strength are catalytically active [Toulhoat et al, 1997].

1.2.2 Marcasite-type

The marcasite-type $OsAs_2$ and $RuAs_2$ are characterized by the orthorhombic crystal structure with space group D_{2h}^{12} (Pnnm) and space group number 58. The structure consists of two metal atoms (Os/Ru) at 2a position: (0, 0, 0) and the four As atoms at 4g position: (u, v, 0). Additional fourteen positions are generated from the three different symmetry points (2d) ($\frac{1}{2}$, 0, 0); (4g) (u1, v1, 0) and (8h) (x, y, z), where $u \approx 0.170$, $v \approx 0.378$ and $0 \leq x, y, z \leq \frac{1}{2}$. The $OsAs_2$ and $RuAs_2$ are also metallic in nature with lattice constants of a = 5.4129 Å, b = 6.1910 Å, c = 3.0126 Å and a = 5.4302 Å, b = 6.1834 Å, c = 2.9714 Å, respectively [Holse, 1968]. The crystal structure of the marcasite-type with the dimer pair As-As is shown in Figure 1.2 and the experimental crystal structure positions are indicated in table 1.1.

$OsAs_2$ and $RuAs_2$ have the lollingite ($FeAs_2$) or rammelsbergite ($NiAs_2$) formation, where the As atoms form close-packed layers arranged in hexagonal stacking sequence, with metal atoms located at the centres of all the octahedral interstices. The relationship between pyrite and marcasite is often mistakenly confused. The large difference in the atomic arrangement of the orthorhombic marcasite structure to the cubic pyrite structure is that, on the marcasites the edge-sharing of cation octahedral also occurs in linear chains parallel to the orthorhombic axis [Bullet et al, 1982]. Most of the marcasite minerals have dimorphs in the pyrite group i.e. they can crystallize as marcasite and pyrite. Moreover the stability relations between marcasite- and pyrite-type are unclear. However, the thermal stability of pyrite- and marcasite-type depends mainly on the difference in atomic arrangement on the crystal structure [Huang et al, 2001].

1.3 Literature review

This section gives literature on the structural, electronic and optical properties of the pyrite and marcasite in the form of FeS_2 together with RuS_2 which is the only mineral previously studied among the structures OsS_2, $OsAs_2$ and $RuAs_2$. Compounds with the pyrite and marcasite structure more especially FeS_2 have been studied extensively both experimentally [Deer et al, 1992; Eyert et al, 1998; Jaegerman et al, 1993, Ennaoui et al, 1984] and theoretically [Temmerman et al, 1993; Zhao et al, 1993; Sithole et al, 2003]. Among the sulphides minerals, FeS_2 in the form of pyrite and marcasite is the most common, and serve as the useful model system for understanding the chemical and physical properties of this class of minerals [Muscat et al, 2002].

Structural properties of the pyrite and the closely related marcasite, FeS_2 mineral were previously studied to better understand the relationship between the two forms. The crystal structure of the pyrite was the main focus, but other experiments looked at the internal parameters to investigate how the structure is related to the marcasite [Pauling et al, 1934; Buerger et al, 1931 and 1937; Brostigen et al, 1969]. In the two forms, each Transition–Metal (TM) atom is surrounded by six nearest-neighbour sulphur atoms in a distorted octahedral environment while each S atom sits at the centre of a distorted tetrahedron formed by one S and three TM atoms. Direct sulphur neighbours exist only in the pyrite and marcasite structures in the form of S pairs which are the characteristic features [Raybaud et al, 1997]. In addition to the crystal structure, the types of bonds between the S-S and Fe-S were also looked at as one of the differences between the pyrite and marcasite [Sithole, 2000]. Topological methods were carried out by Hyde et al (1996) and pointed to the difference in the edge-sharing octahedral and corner-sharing respectively [Hyde et al, 1996].

Among the disulphides, the dominant structure types are the pyrite structure formed by the 4d compounds RuS_2 and RhS_2 and the 5d compounds OsS_2 and IrS_2 [Raybaud et al,1997]. Of these structures, the RuS_2 belongs to the family of transition-metal dichalcogenide crystallizing in the pyrite structure and has been previously studied using different methods [Sutarno et al, 1967; Pecoraro et al, 1981]. It is a promising material for the thermal catalytic processing of organic sulphur and nitrogen compounds in petroleum refining. In electrochemical investigations, the ruthenium compounds have attracted interest as electrode or photo-electrode materials because of their catalytic properties and favourable stability. In particular, much attention has been paid to RuS_2 because of its potential application in photo-electrochemical devices [Ezzaouia et al, 1983]. Despite its technological importance, the theoretical and experimental understanding of its solid-state properties is still relatively incomplete [Holzwarth et al, 1985]. The lattice constant for RuS_2 was determined to be 5.6095 Å with the bond lengths Ru-S and S-S reported to be 2.351 Å and 2.179 Å respectively by Sutarno, Knop and Reid [Sutarno et al, 1967]. The investigations on the structural properties of the pyrite- and marcasite-type structures is still of great interest based on the variety of data reported.

Electronic structure calculations for this class of compounds have first been performed by Li et al (1974), Tossel et al (1977), Khan (1974), Bullett (1982) and Raybaud et al, (1997). However, detailed experimental and theoretical studies have been conducted mainly on pyrite FeS_2 [Sithole, 2000]. In most cases on the study of pyrite FeS_2, it was anticipated to be a semiconductor, with Fermi level falling between the t_{2g} and e_g by assuming that the ligand-field energy is much greater than the Hund's rule coupling [Bullet, 1982]. The main characteristics of the electronic band structure may be derived from the assumption that the sulphur pairs may be considered as divalent molecular anions, S_2^{2-} with empty antibonding pσ* states. In the distorted octahedral surrounding the T-M d-band splits into t_{2g} and e_g manifolds [Raybaud et al, 1997]. Considering RuS_2 which is much related to FeS_2, density of states (DOS) analysis requires knowledge of the contribution by the states from the Ru atoms and the S atoms which are said to be partial DOS (PDOS) to yield the total DOS. The semiconducting behaviour of this diamagnetic compound was verified on polycrystalline samples [Hulliger et al, 1963].

The essential difference in the electronic structure of the marcasite phase and the pyrite phase on FeS_2 is that the marcasite phase has the increased splitting of the t_{2g} orbitals in the less regular octahedral environment [Hulliger et al, 1965]. Also Bullet (1982) performed the first calculations and obtained a large band gap for pyrite than marcasite.

The energy band structure is one of the most important factors in determining the solid-state properties of a material [Yang-Fang Chen et al, 1987]. The single crystal RuS_2 study was reported to have the band gap in the range 1.9 eV to 5.1 eV using the electrolyte-electro reflectance (EER) method [Yang-Fang Chen et al, 1987]. The calculated charge densities in a plane containing the (110) and (100) axes which has the nearest-neighbour S-S and Ru-S bonds using the self-consistent valance charge density of RuS_2 were reported previously by Holzwarth et al (1985). Thus the charge density calculations scan best describe the type of bonding between the atoms.

Optical properties of iron pyrite (FeS_2) particularly show unusual properties. According to magnetic measurements, Fe in FeS_2 seems to have no magnetic moments as reported by Benoit (1955), Bither et al (1968) and by Miyahara and Teranishi (1968) [Schlegel et al, 1976]. Fe in FeS_2 is therefore believed to be in the low-spin state and divalent with six electrons filling the 3d t_{2g} band in accordance with Hulliger et al [Hulliger et al, 1965]. There has been a great controversy as to the energy gap value reported in literature. Among other scientists Vartelaus et al [Vaterlaus et al, 1985] determined the energy gap for RuS_2 to be 1.22 eV by optical transmission and reflectivity measurements and Hulliger reported the energy gap to be 1.8 eV [Hulliger, 1963] . However, no detailed analysis of the absorption and reflection edges was reported for RuS_2.

1.4 Intentions of the study

In this thesis, we investigate the properties of the TMS (OsS_2 and RuS_2) and TMA ($OsAs_2$ and $RuAs_2$) systems in both pyrite- and marcasite-stuctures, using first principles DFT.

The main objective is to obtain a good understanding of the structural, electronic and optical properties and compare the results with experiments where possible.

The equilibrium lattice parameters, heats of formations, internal parameters (u, v), bond lengths and equation of states (EOS) together with the elastic constants will be investigated.

The predicted equilibrium structure (most stable) will be used to calculate the electronic properties such as density of states (DOS), charge densities and energy band structures. The DOS and PDOS in particular will show the orbitals contribution of different/ individual atoms in the unit cell and are assigned to particular features. The energy band structure will be determined to understand the origin of the energy gap in the structures which categorizes the material into three main groups, namely: metals, semiconductors and insulators. We will also observe the type of bonding which occurs between interacting atoms from the charge distributions and charge density differences plots.

Furthermore, optical properties will be studied to gain further insights on the structures by showing the type of transitions occurring in the structures. This will show how the material can absorb (absorption curve) and reflect (reflectivity curve) at different photon energies.

Lastly, the effect of pressure on structural, electronic and optical properties will be investigated.

1.5 Outline

The thesis is divided into six chapters: This first chapter presented the general background, structural aspects and literature review of the TMS and TMA structures as well as the intentions of the study.

The second chapter deals with the quantum mechanical methods used in the current study: the plane-wave (PW) pseudopotential methods i.e. Cambridge Sequential Total Energy Package (CASTEP) [Payne et al, 1992; Milman et al, 2000] and Vienna Ab-initio Simulation Package (VASP) [Kresse et al, 2002] within DFT.

Chapter 3 is focused on DFT results and discussion on structural properties such as lattice parameters, internal parameters (u and v) and bond lengths compared with the experimental data. The structural stability of these systems will be discussed from the heats of formation, ΔH_f per atom.

Chapter 4 presents the electronic properties (DOS, PDOS, energy band structures and charge densities) and the experimental data indicated for comparison.

Chapter 5 gives the optical properties (absorption and reflection) of the TMS and TMA and are compared with the experimental data where possible.

In chapter 6, we give the summary and conclusions of the study and finally the references are presented.

CHAPTER 2

METHODOLOGY

This chapter gives details of the methods employed in this study. The work is based on ab initio quantum-mechanical density functional theory [Hohenberg et al, 1964 and Kohn et al, 1965]. This theory is solved using the plane-wave (PW) pseudopotential method within the CASTEP program [Payne et al, 1992; Milman et al, 2000]. The plane-wave pseudopotential method is necessary for performing full geometry optimization of the structures, in particular the internal parameter relaxation of the unit cell. The VASP code [Kresse et al, 2002], in particular is used to calculate the elastic constants and validate the heats of formation where no experimental data is available.

Recent work has demonstrated that computer simulations based on ab initio techniques can provide remarkable insights into a diverse range of industrially important systems [Pasquarello et al, 1998] and the chemistry of water on catalytically important metal oxides [Lindan et al, 1998]. In the same way, DFT has been used by several scientists, among others, P. Raybaud, G. Kresse, H. Toulhoat to investigate with distinction the properties of TMS and TMA [Raybaud et al, 1997].

In the next section, we discuss the quantum mechanical DFT which allows the prediction of the ground state energy of many-body systems.

2.1 Density functional theory

The microscopic description of physical and chemical properties of matter is a complex problem because it deals with a collection of interacting atoms, which may also be affected by some external field [Kohanoff et al, 2003]. This ensemble of particles may be in different phases i.e. gas, solid, liquid, etc.

At the beginning of quantum mechanics, the major issue was to solve the many-body electronic Schrödinger equation for a set of fixed nuclei positions in the structure of matter for a system of N interacting electrons in the external columbic field created by a collection of atomic nuclei (and may be some other external field) [Kohanoff et al, 2003].

However, the effort of devising schemes to solve the problem is really worthwhile since the knowledge of the electronic ground state of the system gives access to many of its properties, for example, stability of structures; equilibrium structural information; elastic, lattice, electronic and optical properties [Kohanoff et al, 2003].

Hartree then proposed the first approximation in the early 1928 at the beginning of quantum mechanics, which postulated that many-electron wavefuction ψ can be written as a simple product of one-electron wave functions [Hartree, 1928]. At about the same time as Hartree (1927-1928), Thomas and Fermi proposed that the full electronic density was the fundamental variable of the many-body problem and derived a differential equation for the density without resorting to one-electron orbitals [Thomas, 1927; Fermi, 1928]. The Thomas-Fermi approximation was actually too crude because it did not include exchange and correlation effects and was also unable to sustain bound states because of the approximation used for the kinetic energy of the electrons [Kohanoff et al, 2003]. However, it has set up the basis for the later development of density functional theory, which has been the way of choice in electronic structure calculations in condensed matter physics during the past and recently it was also accepted by the quantum chemistry community because of its computational advantages compared to Hartree-Fock based methods [Born et al, 1927]. In advance from Thomas-Fermi, Hartree approximation treats the electrons as distinguishable particles and as such a step forward was to introduce Pauli Exclusion

Principle by proposing an antisymmetrized many-electron wave function ψ in the form of a Slater determinant which introduces particles to exchange in an exact manner [Fock, 1930; Slater, 1930]. After the introduction of Pauli Exclusion Principle, the approximation was known to be Hartree-Fock or self-consistent field, which has been the way of chemists for calculating the structure of molecules for a long period of time [Kohanoff et al, 2003].

In 1964, Hohenberg and Kohn [Hohenberg et al, 1964] formulated and proved a theorem which validates that the external potential is univocally determined by the electronic density ρ, except for a trivial additive constant and corollary, since ρ univocally determines the potential, it also determines the ground state wave function ψ [Kohanoff et al, 2003]. The combination of the theorems forms the basis of density functional theory. The theorems proved that the total ground state energy of a many-electron system is a functional of the electron density $\rho(\mathbf{r})$ given as,

$$E = E\,[\rho(\mathbf{r})]. \tag{2.1}$$

In 1965, Kohn and Sham [Kohn et al, 1965] proposed the idea of replacing the kinetic energy of the interacting electrons with that of an equivalent non-interacting system. Moreover, they derived an effective one-electron Schrödinger equation by first comparing the functional as the sum of two terms, written as

$$E\,[\rho] = T_o\,[\rho] + U\,[\rho], \tag{2.2}$$

where T_o is the kinetic energy of non-interacting electrons; $U\,[\rho]$ is the coulomb energy which contains the electrostatic energy arising from the columbic attraction between electrons and nuclei, the repulsion between all electronic charges, and the repulsion between nuclei. This coulomb energy can be written as,

$$U\,[\rho] = U_{en}\,[\rho] + U_{ee}\,[\rho] + U_{\text{ion-ion}}. \tag{2.3}$$

The set of wave functions that minimize the Kohn-Sham energy functional are given by the self-consistent solutions of the equation:

$$\left[-\frac{\hbar^2}{2m}\nabla^2 + V_{ion}(r) + V_H(r) + V_{XC}(r)\right]_i \psi(r) = \varepsilon_i \psi_i(r), \qquad (2.4)$$

where ψ_i is the wave function of electronic state *i*; ε_i is the Kohn-Sham eigenvalue, V_{ion} is the static total electron-ion potential and V_H is the Hartree-Fock potential of the electron which is given by

$$V_H(r) = e^2 \int \frac{\rho(r')}{|r-r'|} d^3 r'. \qquad (2.5)$$

The exchange-correlation potential, V_{XC}, is given by the functional derivative

$$V_{XC}(r) = \frac{\delta E_{XC}[\rho(r)]}{\delta \rho(r)} \quad , \qquad (2.6)$$

$\rho(\mathbf{r})$, the electron density, is given by

$$\rho(r) = 2\sum_i \int |\psi_i(r)|^2 . \qquad (2.7)$$

Therefore, the Kohn-Sham total-energy functional can be written as follows:

$$E = 2\sum_{occ} \varepsilon_i + U_{ion-ion} - \frac{e^2}{2} \iint \frac{\rho(r)\rho(r')}{|r-r'|} dr dr' + E_{XC}[\rho(r)] - \int \rho(r) V_{XC} dr . \qquad (2.8)$$

The methodology used for solving the Schrödinger equation and the DFT Kohn-Sham equation, respectively are compared in Figure 2.1.

2.1.1 Local density approximation

From the discussion above, the exchange-correlation potential cannot be obtained explicitly, because the exact exchange-correlation energy is not known. This problem is solved by way of approximation methods such as the local density approximation (LDA) [Chauke, 2005; Becke, 1988], where the exchange-correlation energy density is assumed to be that of a homogeneous electron gas with the same density as that

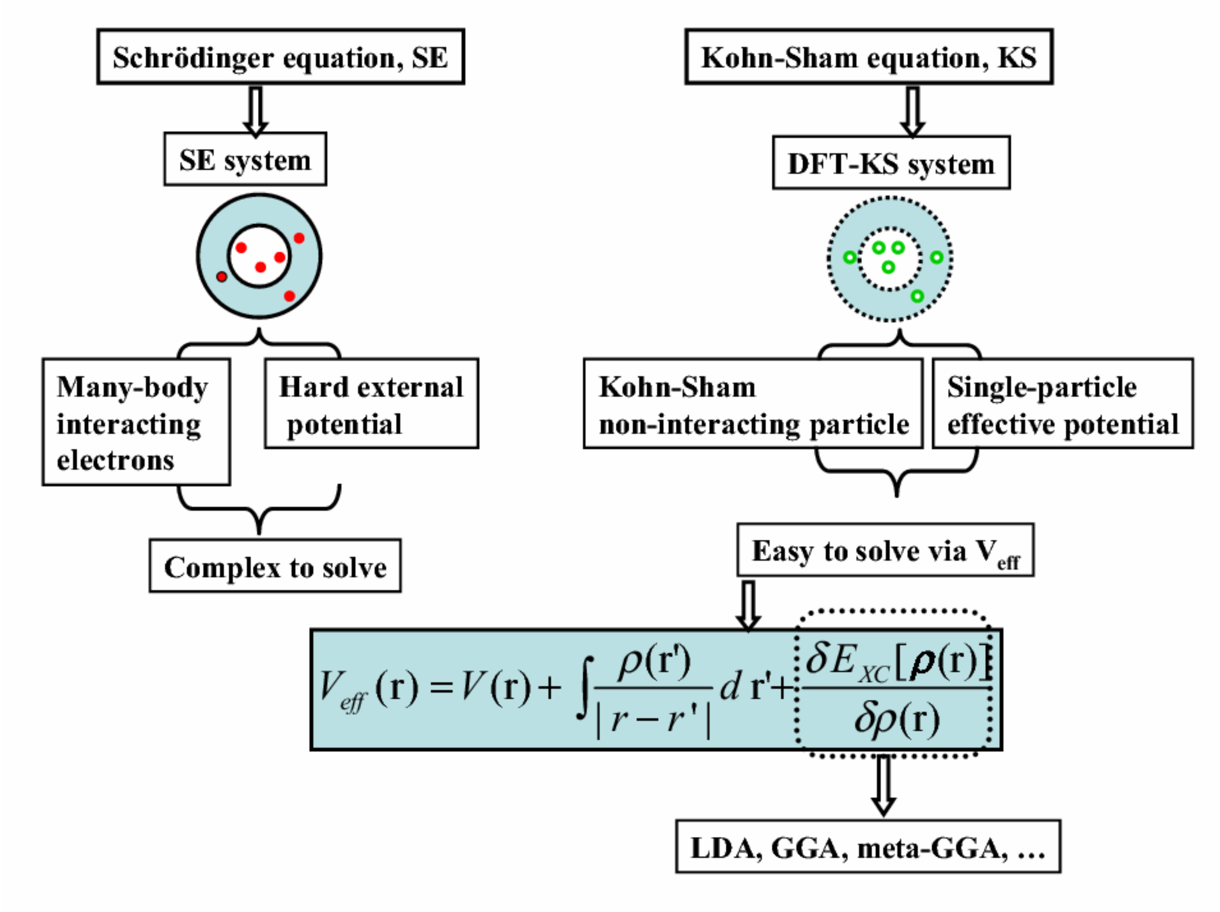

Figure 2.1: A comparison of the methodology for solving the many-body Schrodinger equation and effective one-electron Kohn-Sham equations respectively [Mattsson et al, 2005; Chauke, 2005].

seen locally by the electron. LDA has been for a long time the most widely used approximation to the exchange-correlation energy. Within this approximation the exchange-correlation energy density is defined as

$$E_{XC}^{LDA}[\rho(r)] = \frac{1}{2}\int \frac{\rho_{XC}^{LDA}(r, r')}{|r - r'|} dr' . \tag{2.9}$$

When the electron density varies arbitrarily, it will make it complicated to get the exact expression for the $E_{XC}^{LDA}(\rho(r))$. However, the slowly variation of $\rho(\mathbf{r})$ will give the expression for the exchange-correlation energy as

$$E_{XC}^{LDA}[\rho(r)] = \int \rho(r)\, \varepsilon_{XC}^{LDA}(\rho(r)) d^3(r) \quad , \tag{2.10}$$

and the exchange-correlation potential may be written as,

$$\frac{\delta E_{XC}^{LDA}[\rho(r)]}{\delta\rho(r)} = \frac{\partial[\rho(r)\varepsilon_{XC}^{LDA}(r)]}{\partial\rho(r)} \quad , \tag{2.11}$$

with

$$\varepsilon_{XC}^{LDA}(r) = \varepsilon_{XC}^{LDA}[\rho(r)] \ , \tag{2.12}$$

where $\varepsilon_{XC}^{LDA}(\rho)$ represents the exchange and correlation energy per electron of a uniform electron gas of density ρ.

The approximation above is referred to as the local density approximation (LDA) which turned out to be computationally convenient and accurate. The LDA typically underestimates equilibrium bond lengths and cell parameters by 1-2 % [Becke, 1988]. Though it can approximate the energy band in semiconductors to be very small [Kohanoff et al, 2003], it remains the choice for the exchange-correlation energy which is taken from the known results of the many-electron interactions in an electron system of constant density (homogeneous electron gas).

2.1.2 Generalized gradient approximation

The introduction of a dependence on the gradient of the density and the class of corrected exchange-correlation functional in an inhomogeneous system led to the development of the gradient correction or generalized gradient approximation (GGA) which has been introduced by Perdew and Wang [Perdew et al, 1986]. The GGA functional adds the gradient of the density, $|\nabla\rho(r)|$, as an independent variable, and the description of the exchange and correlation in an inhomogeneous system is non-local with respect to the electrons it surrounds. The basic idea of GGA is to express the exchange-correlation energy in the following form:

$$E_{XC}[\rho(r)] = \int \rho(r)\, \varepsilon_{XC}[\rho(r)] d^3(r) + \int F_{XC}[\rho(r), \nabla\rho(r)] dr \qquad (2.13)$$

where the function F_{XC} satisfies a number of formal conditions for the exchange-correlation hole.

There are a number of different GGA functional, for example, the Perdew-Wang' 86 (PW86) correctional functional [Perdew, 1986], PW91 [Perdew et al, 1991] the Perdew-Bercke-Ernzerhof (PBE) exchange-correlation functional [Perdew et al, 1996; Perdew et al,1997], are commonly used in physics and are called 'parameter free', whereas BLYP [Becke, 1998] is commonly used in chemistry and referred to be empirical.

The use of GGA has little influence on local properties and tends to overestimate the bond lengths and cell parameters, but does lead usually to a significant improvement in global changes in the total energy, such as those that result when two atoms combine to make a molecule. In the case of 4d-5d transition metals, the improvement of the GGA over the LDA is not clear and will depend on how well the LDA perform in the particular case [Kohanoff et al, 2003].

2.2 Plane-wave pseudopotential method

The plane-wave pseudopotentials technique is a good method used to calculate the variation self-consistent solution to the density functional theory. It is applied in big systems subjected to 3D periodic boundary conditions. In this method the wave function is expanded in terms of the plane-wave basis and giving a good pseudopotential representation of the ions in the crystal.

2.2.1 Plane-wave basis

The use of a plane wave (PW) basis set offers a number of advantages, including the simplicity of the basis functions, which make no preconceptions regarding the form of the solution, the absence of basis set superposition error, and the ability to efficiently calculate the forces on atoms [Segall, 1997]. In general, a continuous, and hence infinite basis set is required in the representation of an arbitrary orbital in terms of a PW basis set which expand the electronic wave functions of the system. A good description of the PW basis method is by the use of Bloch's theorem [Ashcroft, 1976] which allows the expansion of electronic wave functions in terms of a discrete set of plane waves. The expression for the electronic wavefunctions for a periodic solid according to Bloch's theorem can be written as follows

$$\psi_{ki}(r) = \exp[ik.r] f_i(r), \qquad (2.14)$$

and enables us to expand the crystal wavefunction in terms of plane waves, $f_i(r)$, written as

$$f_i(r) = \sum_G C_{i,G} \exp[iG.r], \qquad (2.15)$$

where G is the reciprocal lattice vector of the periodic cell. Thus each electronic wave function can be written as a sum of plane waves,

$$\psi_{i,k}(r) = \sum_G C_{i,k+G} \exp[i(k+G).r] \tag{2.16}$$

where k is a symmetry label which lies within the first Brillouin zone and $C_{i,k+G}$ are the coefficients for the plane waves and depend entirely on the specific kinetic energy, $\left(\frac{\hbar^2}{2m}\right)|k+G_c|^2$. This parameter controls the convergence of the expansion by choosing the kinetic energy cut-off. In practice, the plane wave basis set is restricted to a sphere in reciprocal space most conveniently represented in terms of a cut-off energy, E_{cut}, such that for all values of G, the kinetic energies are less than or equal to some particular cut-off energy, E_{cut}. Thus only for plane waves obeying

$$\frac{\hbar^2}{2m}|k+G_c|^2 \leq E_{cut} \tag{2.17}$$

are included in the basis. However, one can describe more rapidly varying features and infinitely large number of basis set could be achieved when the number of plane waves is increased. Thus when finite cut-off energy is introduced to the discrete plane-wave basis set, a finite basis set is obtained. Although this may lead to some errors in the computation of the total energy, cut-off energy should be increased until the calculated energy has converged.

Substitution of equation 2.16 into equation 2.4, the Kohn-Sham expression takes the form,

$$\sum_{G'} \left[\frac{\hbar^2}{2m}|k+G|^2 \delta_{GG'} + V_{ion}(G-G') + V_H(G-G') + V_{XC}(G-G') \right] C_{i,k+G'} = \varepsilon_i C_{i,k+G'} \tag{2.18}$$

and the various potentials are described in terms of their Fourier transformations.

2.2.2 The pseudopotential method

The psuedopotential method is constructed for each atomic species which takes into account the effects of the nucleus and core electrons with their states assumed to be fixed [Cohen et al, 1970; Phillip, 1958; Yin et al, 1982]. In this method, the important features of a valence electron moving through a crystal including relativistic effects are described by weaker pseudopotentials, which replaced the core electrons and the strong attractive coulomb potential inside the ionic core [Cohen et al, 1970; Payne et al, 1992]. Thus the original solid is replaced by pseudo-valence electron and pseudo-ion cores. These pseudoelectrons have a much weaker potential inside the core region but experiences similar potential outside the core region as the original electrons. The ionic potential (Z/r), valence wave function (Ψ_v), the corresponding pseudopotential (V_{pseudo}) and pseudo wave function (Ψ_{pseudo}) are indicated in Figure 2.2 [Payne et al, 1992]. The utilization of pseudopotential approximation method is advantageous, because it allows the electronic wave function to be expanded using a much smaller number of plane-wave basis states, and a less amount of computational time would be required in the calculations. The most general form for pseudopotential is given by

$$V_{NL} = \sum_{lm} |lm\rangle V_l \langle lm| , \tag{2.19}$$

where $|lm\rangle$ and $\langle lm|$ are the spherical harmonics and V_l is the pseudopotential for angular momentum *l*. However, a pseudopotential using the same potential for all the angular momentum components of the wave function is called a local pseudopotential, which is a function that only depends on the distance dependence of the potential. An example of the non-local pseudopotential is the norm-conserving pseudopotential (NCP) by Kleinmann and Bylander [Kleinmann et al, 1982], and uses a different potential for each angular momentum components of the wave function. The ultrasoft pseudopotential (USP) which has been introduced by Vanderbilt recently [Vanderbilt, 1990] is used in plane-wave calculations and the pseudo-wave functions are allowed to be as soft as possible within the core region in this scheme. A wide range of atoms including the transition metals are covered by USP. In this thesis

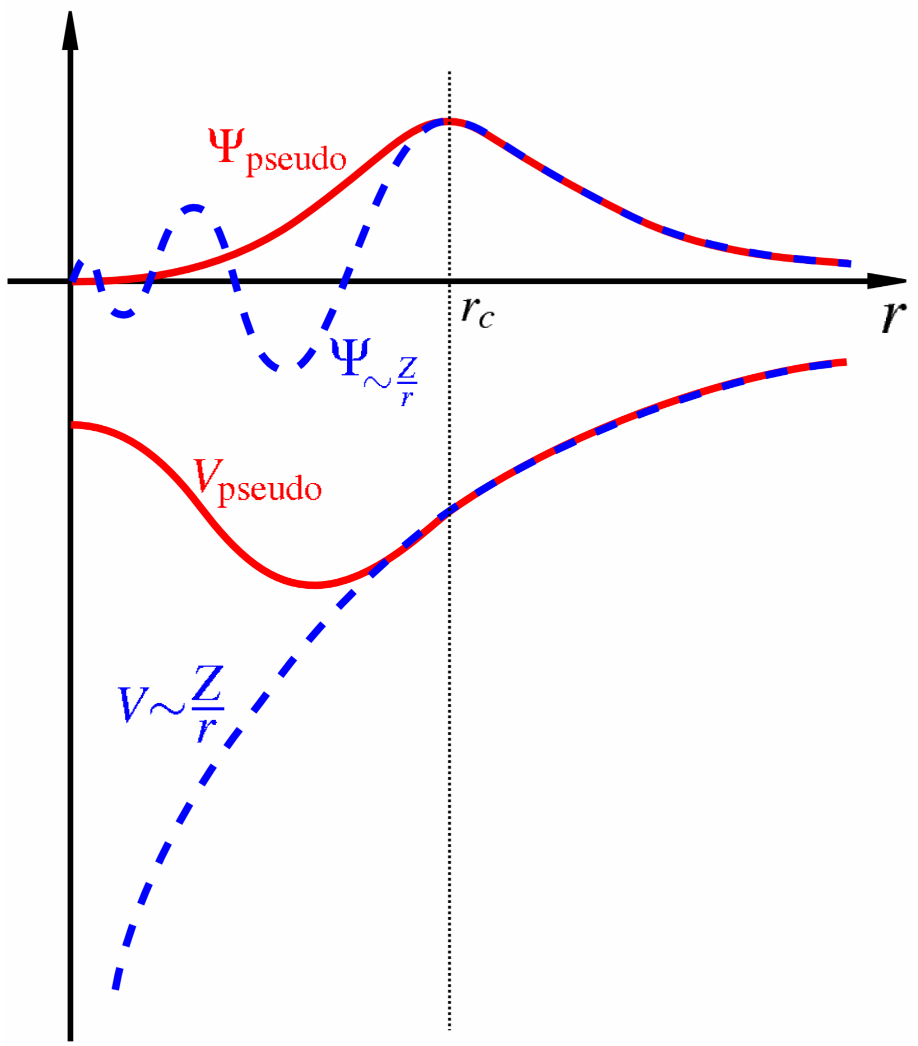

Figure 2.2: Comparison of a wavefunction in the coulomb (all-electron) potential of the nucleus (blue) to the one in the pseudo-potential (red). The real and the pseudo wavefunction and potentials match above a certain cut-off radius r_c [Payne et al, 1992].

we use the USP by Vanderbilt [Vanderbilt, 1990] for total energy calculations within the CASTEP program [Milmann et al, 2000; Segall et al, 2002] for the TMS and TMA under study.

2.2.3 Brillouin zone sampling

For a periodic system, the k-points appearing in the wave function belong to the first Brillouin zone (BZ), by virtue of the Bloch's theorem, Equation (2.14) [Saada, 2000]. Via this theorem, the electronic structure in the periodic system can be treated applying translational symmetry, i.e. an infinite number of atoms and electronic states is transformed into a finite number of atoms and states in a translationally invariant unit cell but with an infinite number of wave-vectors (k-points) in the Brillouin zone.

In order to compute the properties of the materials such as the total energy, forces and stress accurately, it is necessary to integration over all the occupied electronic states. In calculation of the energy band, or the charge density for example, the sum over these k-points has to be calculated and the choice of a sufficiently dense mesh of summation is crucial for the convergence of the results [Saada, 2000].

However, the computational cost increases linearly with the number of k-points within the BZ. This computational cost are reduced by special k-point schemes which have been developed to use the fewest possible k-points for a given accuracy, such as the Monkhorst-pack scheme [Monkhorst et al, 1976] as proposed by Monkhorst and Pack. This coupling scheme is to date, proposed and is the most commonly used to generate efficient and accurate sets of special points where the k-points are distributed homogeneously in the BZ according to

$$k = x_1 b_1 + x_2 b_2 + x_3 b_3 \tag{2.20}$$

where b_1,b_2,b_3 are the reciprocal lattice vectors, and

$$x_i = \frac{l}{n_i}, \qquad l = 1, \ldots, n_i \qquad (2.21)$$

where n_i are the folding parameters. The density functional codes approximate these k-space integrals with a finite sampling of k-points. Other alternative methods for choosing k-point mesh has been proposed by Chadi and Cohen [Chadi et al, 1973] on the basis of “shells” analysis, Joannopoulos and Cohen [Joannopoulos et al, 1973].

2.2.4 CASTEP

The first version of Cambridge Sequential Total Energy Package (CASTEP) was introduced by Mike Payne in 1986 [Payne et al, 1992]. By 1992, many features were added to the code by several scientists. Those features among others are arbitrary cell shape, stresses, partial occupancies for metals, non-local pseudopotentials and real-space pseudopotentials evaluation [Segall et al, 2002; Gibson et al, 2006]. Within a couple of years afterwards, more developments were made including gradient-correlated functionals and ultrasoft pseudopotentials [Segall et al, 2002; Xiong et al, 2005].

This code employs a plane-wave technique to deal with materials with weak pseudopotentials. The code usually best addresses problems in semi-conductors since pseudopotential can be either local or non local (inseparable Kleinmann-Bylander form). Although CASTEP is primarily intended for use on large-scale periodic systems, it can also be applied to supercells constructed to study defects, surfaces/interfaces, and molecules. This module offers a choice of methods for electronic relaxation to ground state for metals, insulators or semiconductors with a more traditional scheme, involving minimization of the total energy. This minimization can be achieved either by using band-by-band technique, where each wavefunction is optimized independently, or by a modern all-bands method that allows simultaneous update of all wavefunctions (only the all-bands scheme is supported for ultrasoft potentials). The scheme uses a preconditioned conjugate gradients technique, as described by Mike Payne [Payne et al, 1992]. Plane-wave uses special k-points sampling for integration over the Brillouin Zone, fast Fourier transforms (FFT) to evaluate matrix elements, and wave function symmetrization for crystals with point-group symmetry higher than P1. For metallic systems, CASTEP introduces partial occupancies for levels close to the Fermi energy [De Vita et al, 1992]. It suffers from all the typical problems associated with LDA (or more generally with the use of density functional theory). An appropriate choice of the k-points set is important for achieving balance between accuracy and efficiency. An increased k-point set reduces the finite basis set correction and makes cell relaxation more accurate at a fixed energy cut-off. A variety of k-points sampling can be chosen using the CASTEP code for different systems. In this thesis, we use CASTEP to investigate the properties of the TMS and TMA under study.

2.2.5 VASP

The Vienna Ab-initio Simulation Package (VASP) code has been developed over the past years to assist in atomistic density functional simulations [Kresse et al, 2002; Hafner et al, 2006]. Presently VASP allows us to perform large scale ab-initio quantum-mechanical simul-ations and finite temperature molecular dynamic (MD). The approach taken is based on a finite-temperature local-density approximation (LDA) with the free energy as variational quantity and an exact evaluation of the instantaneous electronic ground state at each MD-step using matrix diagonalization schemes (based on iterative methods) and efficient charge density mixing techniques [Kresse et al, 2002,]. These techniques avoid the problems occurring in the original Car-Parrinello method based on the simultaneous integration of electronic and ionic equations of motion [Kresse et al, 2002; Ouyang et al, 2004]. In VASP, the interaction between the ions and electrons is described using ultrasoft vanderbilt pseudopotentials (US-PP) or the projector augmented wave method (PAW) [Blöch, 1994; Kresse et al, 2002]. The two techniques will allow a considerable reduction of the size of the basis set (i.e. the number of plane-waves per atom) for transition metals and first row elements on the periodic table. This approach allows the VASP code to treat larger problems than usual ones. It can also predicts the forces acting on atoms and stress on the unit cell using different techniques. Also an appropriate sampling of k-points set is important for achieving balance between accuracy and efficiency.

The VASP code was employed in the calculations of formation energies and the elastic constants for both TMS and TMA systems of the current study.

2.2.6 Convergence of energy cut-off and k-points sampling

The energy cut-off and number of k-points are important as they determine the number of plane waves required to perform the calculations.

It has been assured that the accurate ground state energy of the pyrite and marcasite structures is obtained, thus by performing convergence test on energy cut-off with respect to k-points.

With the CASTEP code cut-off energy of 500 eV was sufficient for the convergence of the total energy for the pyrite-type OsS_2 and marcasite-type $OsAs_2$ structures respectively as shown in Figure 2.3. The plots show that the variation of total energy with cut-off is relatively negligible from the energy cut-off of 500 eV. This cut-off energy gives a Fast Fourier Transformation (FFT) grid of 36 x 36 x 36 for OsS_2 and RuS_2, and 40 x 40x 40 for $OsAs_2$ and $RuAs_2$ pyrite-type structures whereas marcasite-type structures $OsAs_2$ and OsS_2 gives 36 x 40 x 20, and $RuAs_2$ and RuS_2 indicated 36 x 40 x 18.

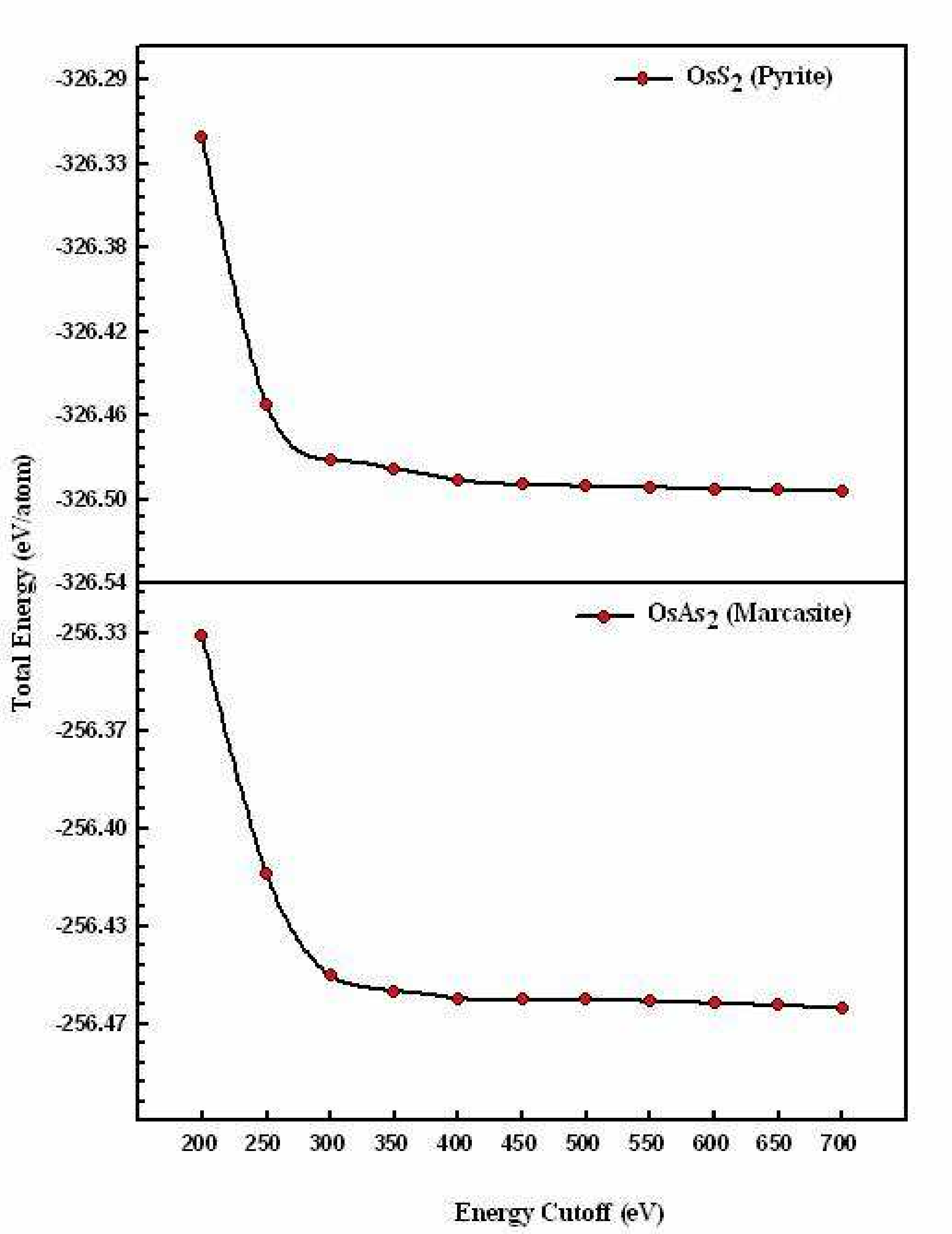

Figure 2.3: Total energy per atom versus energy cut-off for pyrite OsS_2 and marcasite $OsAs_2$ (CASTEP calculation).

This Monkhorst-Pack scheme [Monkhorst et al, 1976] of FFT was employed to select an optimal set of special k-points of the first Brillouin zone such that the greatest possible accuracy is achieved from the number of points used. A k-point mesh of 10 x 10 x 10 was chosen since we noticed that at 8 x 8 x 8 the structure has already converged to a meV as shown in Figure 2.4 for the pyrite-type OsS_2 and marcasite-type $OsAs_2$ structures. The other structures also show similar trends as that in figure 2.4. This k-point mesh corresponds to 45 irreducible k-points for the pyrite-type structures and a k-points mesh of 6 x 6 x 11 which corresponds to 54 irreducible k-points for the marcasite-type structures was used in the first Brillouin zone.

The same cut-off energy and equivalent k-point mesh was used within VASP to ensure accuracy and consistency. The requested k-spacing was 0.11 per Angstrom, which leads to a 10 x 10 x 10 mesh corresponding to 45 symmetry-unique k-points for pyrite-type compositions. Whereas k-spacing for the marcasite-type structures was 0.2 per Angstrom, which leads to a 6 x 6 x 11 mesh corresponding to 54 symmetry-unique k-points.

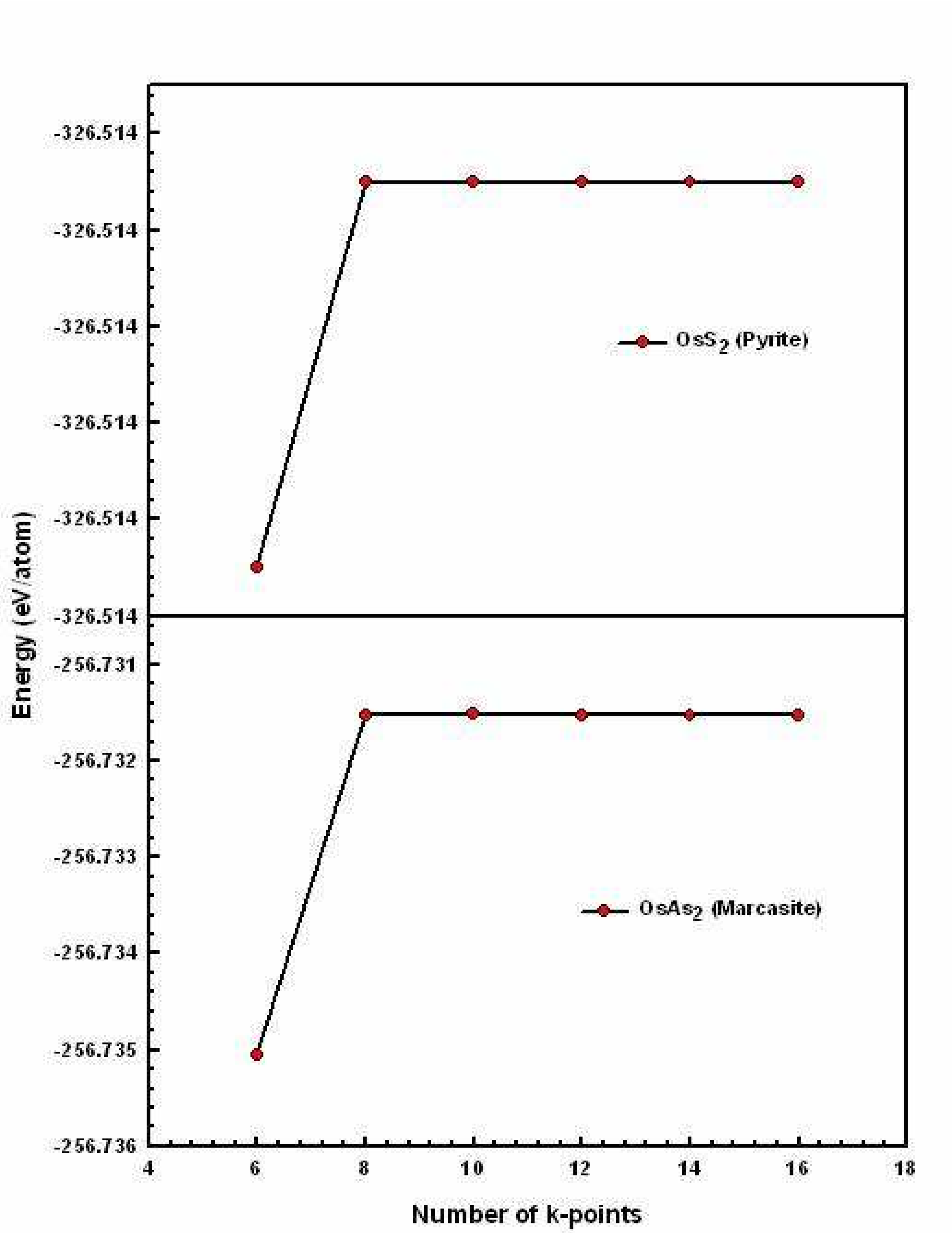

Figure 2.4: Total energy per atom versus k-points for pyrite OsS_2 and marcasite $OsAs_2$ (CASTEP calculation); 10 = 10 x 10 x 10 etc.

CHAPTER 3

STRUCTURAL PROPERTIES

This chapter gives the results and discussions on structural and equilibrium properties of $OsAs_2$, $RuAs_2$, OsS_2 and RuS_2 using plane-wave pseudopotential methods within CASTEP and VASP codes as discussed in the previous chapter.

3.1 Equilibrium geometry relaxation

We performed geometry optimization calculations for the TMS (OsS_2, RuS_2) and TMA ($OsAs_2$, $RuAs_2$) structures in both pyrite- and marcasite-type, within LDA to compare their equilibrium structural properties. The lattice and internal parameters for these systems were allowed to vary, thereby minimizing the structure to its most stable form. Furthermore, we have performed a series of single point energy calculations to determine the minimum energy as a function of the lattice constants for the TMS and TMA systems. The results are depicted in the plots of energy versus volume in Figure 3.1 and are summarized in table 3.1. These plots have a minimum point corresponding to the equilibrium lattice parameter and volume. For example, we observe similar trends for all the parabolic curves and they reach a minimum where the energy is lowest corresponding to a particular lattice constant. The energy difference per atom between the pyrite-type and marcasite-type vary, i.e. the TMA has a larger change in energy, ΔE (≈ 0.46 eV/atom) compared to TMS (≈ 0.06 eV/atom). This is due to the atomic size difference between As and S with As being the largest. Their values are shown in table 3.1 together with the experimental parameters for comparison. The short lines in the table indicate that experimental data is not available. The equilibrium lattice parameters compare well with the experimental values, for example the lattice parameter for RuS_2 pyrite ($a = 5.565$ Å)

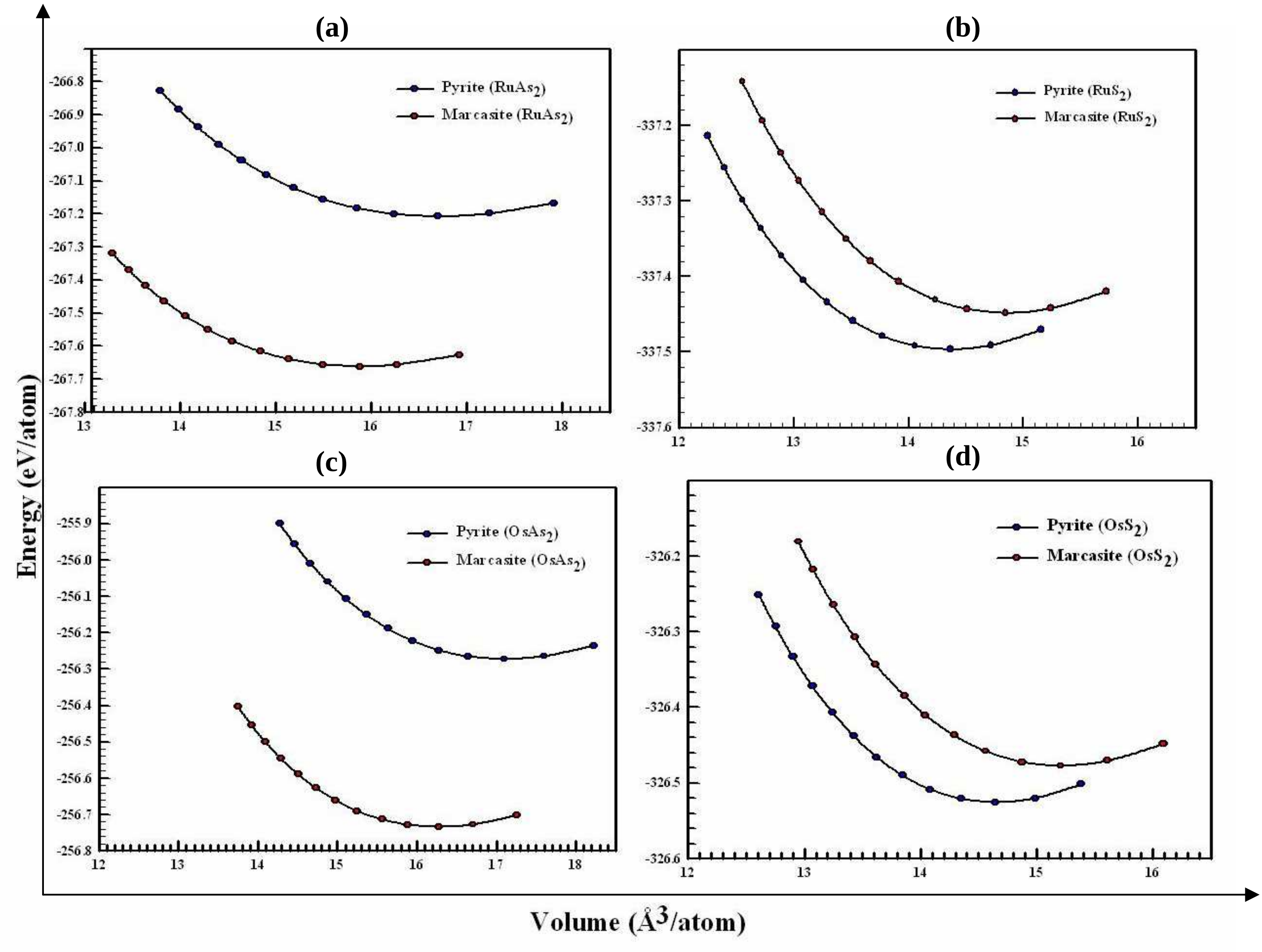

Figure 3.1: Total energy per atom against volume per atom for pyrite- and marcasite-type structures: (a) $RuAs_2$, (b) RuS_2, (c) $OsAs_2$ and (d) OsS_2.

agree to within 1 % with the experimental value while the marcasite $RuAs_2$ is within 2 % in agreement with experimental lattice parameters. The predicted equilibrium volume for RuS_2 pyrite is 14.3651 Å^3/atom which compare well with the experimental volume of 14.720 Å^3/atom and $RuAs_2$ marcasite structure predicted the equilibrium volume to be 15.8910 Å^3/atom which gives a good correlation with the experimental value of 16.843 Å^3/atom. From our calculations, it is clear that LDA underestimates the parameters for the systems. The converted structures as pyrite- or marcasite-type

Table 3.1: Equilibrium lattice parameters, volumes and heats of formation, ΔH_f for pyrite- and marcasite-type structures. The experimental value is given in parenthesis.

Structure	Lattice parameter (Å)		Volume ($Å^3$/atom)		Heats of formation, ΔH_f (eV/atom)
	Calculated	Expt.	Calculated	Expt.	Calculated
$OsAs_2$ (Mar)	a 5.413	5.4129[*]	16.826	16.829[*]	-0.626
	b 6.191	6.1910[*]			
	c 3.013	3.0126[*]			
(Pyr)	a 5.896	——	17.079	——	-0.168
$RuAs_2$ (Mar)	a 5.338	5.4302[#]	15.904	16.843[#]	-0.752
	b 6.082	6.1834[#]			
	c 2.938	3.9714[#]			
(Pyr)	a 5.849	——	16.676	——	-0.302
OsS_2 (Mar)	a 4.488	——	15.207	——	-2.289
	b 5.619	——			
	c 3.618	——			
(Pyr)	a 5.602	5.6196[@]	14.650	14.792[@]	-2.338
RuS_2 (Mar)	a 4.484	——	14.850	——	-2.458
	b 5.584	——			
	c 3.559	——			
(Pyr)	a 5.565	5.6095[&]	14.366	14.713[&]	-2.507(-2.1264)[ξ]

[*, #] [Holse, 1968]
[@, &] [Sutar, 1967]
[ξ] [Chianelli, 2006]

—— No experimental value

also show a good correlation with the naturally occurring ones.

3.2 Heats of formation

The heat of formation, $\Delta H_{f,}$ is convenient for studying the relative structural stability of the competing structures. We have calculated the ΔH_f for both pyrite- and marcasite-type structures by subtracting the elementary total energies of individual atoms from that of the bulk as,

$$\Delta H_f(OsS_2) = \frac{1}{N}\left[E_{Total}(OsS_2) - E_{Total}(Os) - E_{Total}(S)\right] \qquad (3.1)$$

where N is the total number of the atoms, E_{Total} is the total energy. The equation above has been shown for OsS_2 only. However, the same procedure has been used to determine the ΔH_f for the other TMS and TMA systems and the results are given in table 3.1. The experimental value is given only for RuS_2 and thus far nothing has been reported for the other systems to our knowledge.

We note that the heats of formation for the naturally occurring pyrite- and marcasite-types are energetically favorable than the converted forms as expected, for example the naturally occurring pyrite-type RuS_2 is the most stable structure with the lowest ΔH_f of -2.507 eV/atom and compares reasonably well with the experimental value of -2.126 eV/atom [Chianelli, 2006]. However, the converted RuS_2 marcasite-type structure gives -2.458 eV/atom and is higher in energy than the pyrite-type structure (-2.507 eV/atom). The case of pyrite OsS_2 system also shows similar trend.

The converted pyrite-type structures $OsAs_2$ and $RuAs_2$ depict higher energy values of -0.168 and -0.302 eV/atom, respectively whereas the naturally occurring marcasite-type structures $OsAs_2$ and $RuAs_2$ predicted lower energy values of -0.626 and -0.752 eV/atom respectively. This suggests that the naturally occurring marcasite-type structures $OsAs_2$ and $RuAs_2$ are more stable than their converted pyrite-type structures.

3.3 Internal parameter relaxation

The equilibrium internal parameters are shown in table 3.2 for the TMS and TMA systems. The predicted internal parameter u, for the naturally occurring pyrite-type OsS_2 and RuS_2 are 0.3866 and 0.3881 respectively. These u parameters are in excellent agreement to within 0 % to the experimental data, respectively. The internal parameter u, for the converted pyrite-type structures $OsAs_2$ and $RuAs_2$ with 0.3788 and 0.3789, respectively, are also predicted. We see that this converted structure agrees well with the real pyrite-type systems.

The predicted internal parameter u, v for the naturally occurring marcasite-type $OsAs_2$ and $RuAs_2$ are given by 0.1692, 0.3599 and 0.1704, 0.3657 respectively, which are in good agreement with the experimental values 0.170, 0.366 and 0.168, 0.379 respectively. These parameters fall within 1 % of the experimental values. Again the converted marcasite-type OsS_2 and RuS_2 phases are also reasonable and are predicted to be 0.2020, 0.3811 and 0.1965, 0.3831, respectively.

3.4 Equilibrium bond lengths

The equilibrium bond lengths for both pyrite- and marcasite-type structures are given in table 3.2. The calculated bond lengths for the naturally occurring marcasite-type $OsAs_2$ and $RuAs_2$ shows a good correlation between the Os-As and Ru-As distances, with As-As distances showing similar values for both compositions.

The predicted Os-As distance is overestimated to within 1 % and Ru-As bond length is in agreement with the experimental value. The As-As bond lengths for $OsAs_2$ and $RuAs_2$ compare well with the experimental values to within 1 %. In the converted

Table 3.2: Equilibrium internal parameters and bond lengths for pyrite- and marcasite-type compounds.

Structure	Internal Parameters			Bond length (Å)		
		Calculated	**Expt.**		**Calculated**	**Expt.**
OsAs$_2$ (Mar)	u	0.1692	0.170[$]	Os-As	2.4139	2.403[$]
	v	0.3599	0.366[$]	As-As	2.4419	2.463[$]
(Pyr)	u	0.3788	———	Os-As	2.4514	———
				As-As	2.4749	———
RuAs$_2$ (Mar)	u	0.1704	0.168[$]	Ru-As	2.4025	2.403[$]
	v	0.3657	0.379[$]	As-As	2.4442	2.472[$]
(Pyr)	u	0.3789	———	Ru-As	2.4320	———
				As-As	2.4547	———
OsS$_2$ (Mar)	u	0.2020	———	Os-S	2.3250	———
	v	0.3811	———	S-S	2.2526	———
(Pyr)	u	0.3866	0.3865[ξ]	Os-S	2.3447	2.352[@]
				S-S	2.2007	2.210[@]
RuS$_2$ (Mar)	u	0.1964	———	Ru-S	2.3132	———
	v	0.3831	———	S-S	2.1929	———
(Pyr)	u	0.3881	0.3879[ξ]	Ru-S	2.3327	2.350[@]
				S-S	2.1567	2.170[@]

[$] [Holse, 1968]

[ξ] [Sutar, 1967]

[@] [Raybaud et al, 1997]

—— No experimental value

marcasite-type OsS_2 and RuS_2 the S-S bond distances vary by 0.0601 Å.

The calculated bond lengths for the pyrite–type OsS_2 and RuS_2 are also shown in table 3.2. The predicted Os-S and Ru-S distances are underestimated within 0.1 % error and 1.0 % of the experimental values respectively. The calculated S-S bond lengths for OsS_2 and RuS_2 are within 0 % and 1 % of the experimental value respectively. Furthermore, the converted pyrite-type structures $OsAs_2$ and $RuAs_2$ were also investigated and results show that the Os-As, Ru-As and As-As bond lengths are predicted. In summary, the predicted bond lengths for both pyrite- and marcasite-types reveal that the bond strength increases in the order: Ru < Os, with the dimer pairs S-S for the TMS depicting shorter bond lengths than the As-As dimer pairs.

3.5 Equation of states (EOS) and elastic constants

The equations of state were predicted from planewave pseudopotential method by employing the CASTEP code, which are analysed by fitting the Birch-Murnaghan 3rd order equation [Murnaghan, 1944],

$$B = -V_0 \frac{\partial P}{\partial V} \quad , \qquad 3.2$$

where V_0 is the equilibrium volume and V the volume of a unit cell at pressure, P. The EOS plots are given as pressure versus volume ratio V/V_0 curves and are compared for the TMA and TMS in Figure 3.2. We have deduced the bulk moduli (B) for the various structures from Figure 3.2. Their values are shown in table 3.3 and are compared with those predicted using the VASP code. The bulk moduli for both TMS and TMA compare reasonably well for both CASTEP and VASP and are larger for pyrite OsS_2 with pyrite $RuAs_2$ showing less values. In the naturally occurring pyrite-type RuS_2 the bulk moduli are in excellent agreement and those of the naturally occurring marcasite-type $OsAs_2$ agree to within 2.5 %. The bulk moduli of the converted structures such as $RuAs_2$ pyrite-type and RuS_2 marcasite-type depict a high percentage difference of about 9 % and 10 % respectively and this could be ascribed to VASP not being able to optimize structures as precisely/accurately as CASTEP.

The one dimensional analog of the Murnaghan equation [Murnaghan, 1944] provides an approximation for describing the nonlinear relation between normalized lattice parameters and pressure P, as

$$r/r_0 = \left[\left(\frac{B'}{B}\right)P + 1\right]^{-\frac{1}{B'}} \qquad 3.3$$

Where r is the lattice constant along one of the crystal axes,

$$k = B_0^{-1} = -\left(\frac{\partial Inr}{\partial P}\right)_{P=0} \qquad 3.4$$

is the linear compressibility, and B' is the pressure derivative of B (i.e. $\frac{\partial B}{\partial P}$).

From the equation 3.3 we calculated the pressure derivatives, B' for the TMA and TMS and the results are shown in table 3.3. The pyrite-type structured $RuAs_2$ and RuS_2 show lower values of about 2.707 and 2.121 respectively with the marcasite-type structures OsS_2 and RuS_2 predicting higher values of about 6.046 and 6.190 respectively.

Furthermore, the Young's moduli (Y) and the Shear moduli (C) are determined and were predicted to be higher for the naturally occurring structures than the converted ones in both pyrite- and marcasite-type. The converted pyrite-type structures $OsAs_2$ and $RuAs_2$ show very less (Y; C) values as (106.9; 38.22) and (77.58; 27.34) respectively. Moreover, we calculated the ratio of the bulk modulus to shear modulus (C/B) for both TMS and TMA systems and the values are shown in table 3.3. Note that a high C/B ratio (> 0.57) is associated with brittleness whereas a low value

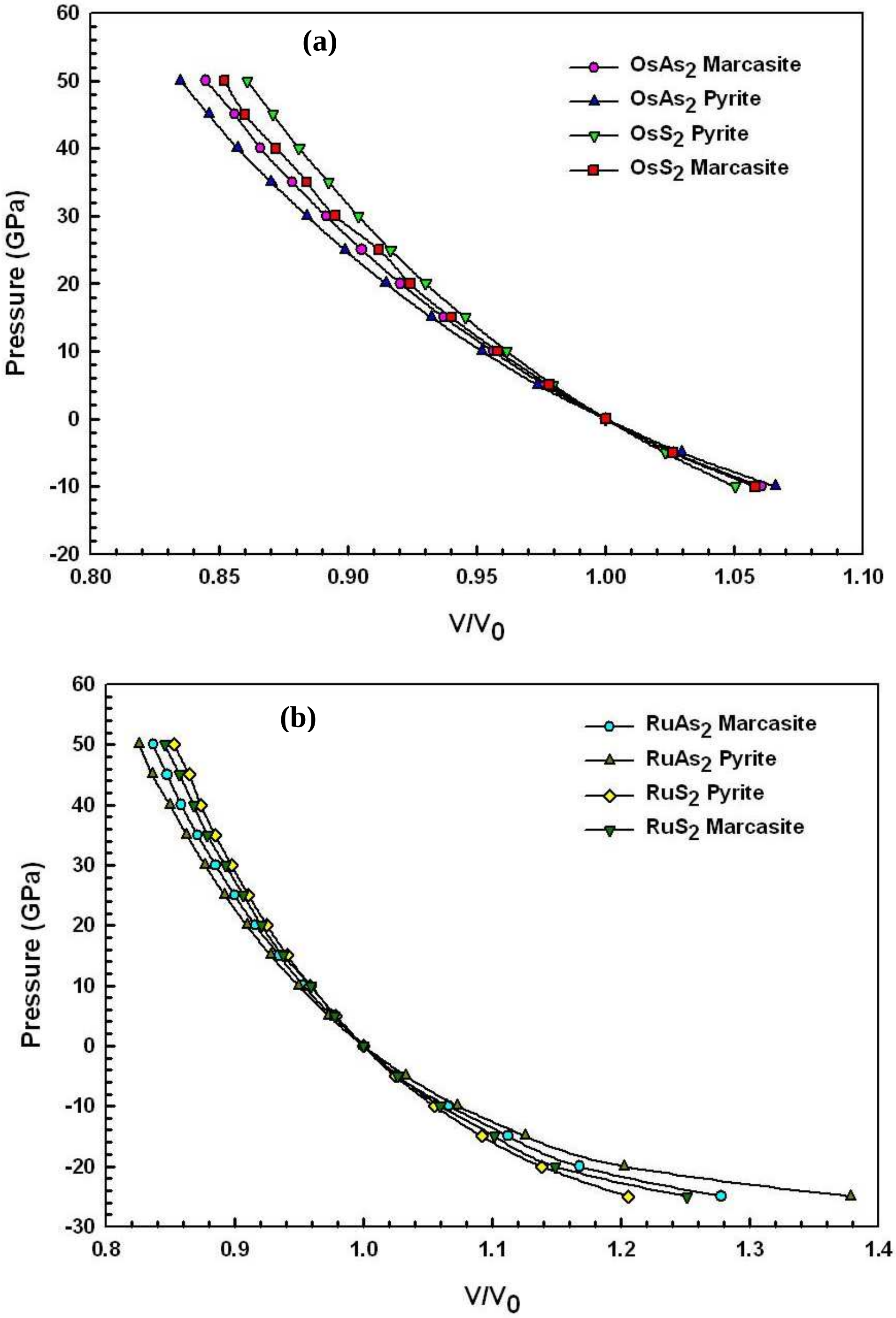

Figure 3.2: Equations of states for pyrite- and marcasite-type (a) $OsAs_2$ and OsS_2, and (b) $RuAs_2$ and RuS_2 structures.

Table 3.3: Elastic constants, Bulk modulus (B), Young's modulus (Y) and Shear modulus (C) of pyrite- and marcasite-type structures for TMA and TMS.

Moduli	**$OsAs_2$**		**$RuAs_2$**		**OsS_2**		**RuS_2**	
	(Mar)	**(Pyr)**	**(Mar)**	**(Pyr)**	**(Mar)**	**(Pyr)**	**(Mar)**	**(Pyr)**
	GPa		**GPa**		**GPa**		**GPa**	
C_{11}	354.5	220.8	334.5	177.8	289.9	517.0	296.5	469.3
C_{12}	123.7	152.1	116.4	149.7	84.20	81.50	72.80	71.70
C_{13}	118.2	——	112.9	——	166.8	——	165.3	——
C_{22}	467.0	——	420.4	——	497.0	——	458.6	——
C_{23}	48.90	——	38.90	——	89.70	——	81.20	——
C_{33}	319.0	——	310.5	——	407.5	——	346.8	——
C_{44}	91.00	40.80	73.40	36.20	91.80	124.4	84.80	107.6
C_{55}	180.4	——	162.4	——	177.2	——	166.2	——
C_{66}	167.4	——	150.0	——	165.0	——	144.4	——
B:CASTEP(EOS)	196.1	180.1	186.0	174.4	206.7	230.2	213.6	204.2
B:VASP(Voigt)	191.3	175.0	178.0	159.1	208.4	226.7	193.4	204.2
B′:CASTEP(EOS)	5.775	5.614	4.058	2.707	6.046	4.977	6.190	2.121
Y:VASP(Voigt)	346.1	106.9	314.2	77.58	350.6	392.0	321.1	350.0
C:VASP(Voigt)	144.4	38.22	130.3	27.34	143.7	161.7	131.3	144.1
C/B:VASP(Voigt)	0.755	0.218	0.732	0.172	0.690	0.713	0.679	0.706
A:VASP(Voigt)	0.833	1.188	0.700	2.576	1.009	0.571	1.085	0.541

(< 0.57) corresponds to a ductile nature [Gou et al, 2007]. Our predicted C/B values for the pyrite-type (OsS_2 and RuS_2) and the marcasite-type ($OsAs_2$, $RuAs_2$, OsS_2 and RuS_2) structures are greater than 0.57 which suggest that the material behaves in a brittle manner. Only the converted pyrite-type structures $OsAs_2$ and $RuAs_2$ are associated with a ductile behaviour with their values being 0.218 and 0.172 respectively.

We have determined the elastic constants for the TMA and TMS systems at a very small strain using VASP code. We see that the cubic pyrite-type structures give three elastic constants C_{11}, C_{44} and C_{12}, whereas the orthorhombic marcasite-type structures show nine elastic constants C_{11}, C_{12}, C_{13}, C_{22}, C_{23}, C_{33}, C_{44}, C_{55} and C_{66}. For the pyrite-type structures the C_{11} indicates higher values and the C_{44} depicts lower values, whereas the marcasite-type structures predict the least values for C_{23} and the C_{22} shows highest values. Moreover, the formulas $\frac{2C_{44}}{C_{11}-C_{12}} \approx ShearAnisotropyFactor$ for the cubic pyrite-type structures and $\frac{4C_{44}}{C_{11}+C_{33}-2C_{13}} = ShearAnisotropyFactor$ for the orthorhombic marcasite-type structures were used to measure the degree of anisotropy in bonding between atoms for the (1 0 0) plane. Our calculated shear anisotropy factor values for the structures are shown in table 3.3. The cubic pyrite-type structures $OsAs_2$, $RuAs_2$, OsS_2 and RuS_2 give the Shear Anisotropy Factor of 1.188, 2.576, 0.571 and 0.541 respectively. This reveal that RuS_2 (naturally occurring) is the most stable with less degree of anisotropy and $RuAs_2$ (converted) is the least stable with higher degree of anisotropy. The orthorhombic marcasite-type structures $OsAs_2$, $RuAs_2$, OsS_2 and RuS_2 depict the Shear Anisotropy Factors to be 0.833, 0.700, 1.009 and 1.085 respectively. It is evident that $RuAs_2$ (naturally occurring) is the most stable due to less degree of anisotropy and RuS_2 (converted) is the least stable due to higher degree of anisotropy.

Generally the naturally occurring structures are more stable than the converted structures in both pyrite- and marcasite-type.

3.6 Pressure dependence of lattice constants.

In this section we investigate the effect of applied hydrostatic pressures on lattice parameters, internal parameters and bond length for TMS and TMA structures for both naturally occurring and converted pyrite- and marcasite-type systems. The pressure variations were calculated from a minimum of -10 GPa to a maximum of 30 GPa in the intervals of 5 GPa using the CASTEP code.

3.6.1 Lattice parameters at applied pressure

Figure 3.3 shows the dependence of lattice parameters on the external hydrostatic pressure for the pyrite-type structures. We observe a considerable decrease in the lattice parameters as the pressure is increased; as such the volume of the structures is decreasing. We also note that the TMA ($OsAs_2$ and $RuAs_2$) have larger volume than the TMS (OsS_2 and RuS_2) which suggests atomic size difference of arsenic (As) and sulphur (S) atoms, where the As atom has larger radius than S atom. The pyrite-type plots for the TMA lie above the pyrite-type plots for the TMS as expected. We see that the $OsAs_2$ has the largest lattice parameter while RuS_2 is the lowest for the entire pressure variations in the plot. However, OsS_2 and RuS_2 decrease rapidly in a similar trend as the pressure is increased and so is the case for $OsAs_2$ and $RuAs_2$ structures.

Furthermore the dependence of the lattice parameters under applied external hydrostatic pressure for the orthorhombic marcasite-type structures are shown in Figures 3.4. We observe a slight decrease in lattice parameters when pressure is incre-

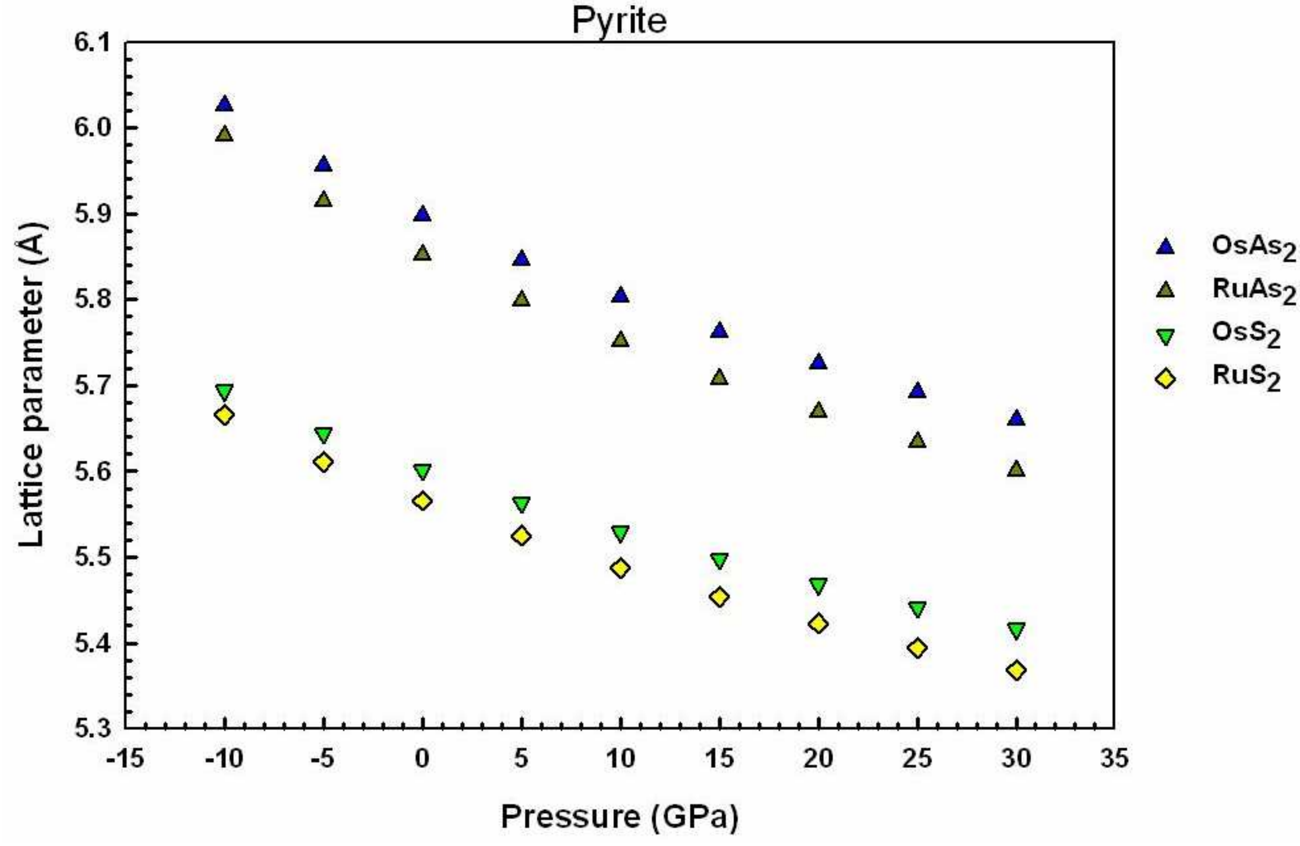

Figure 3.3: Lattice parameter as a function of applied hydrostatic pressure for the pyrite-type structures.

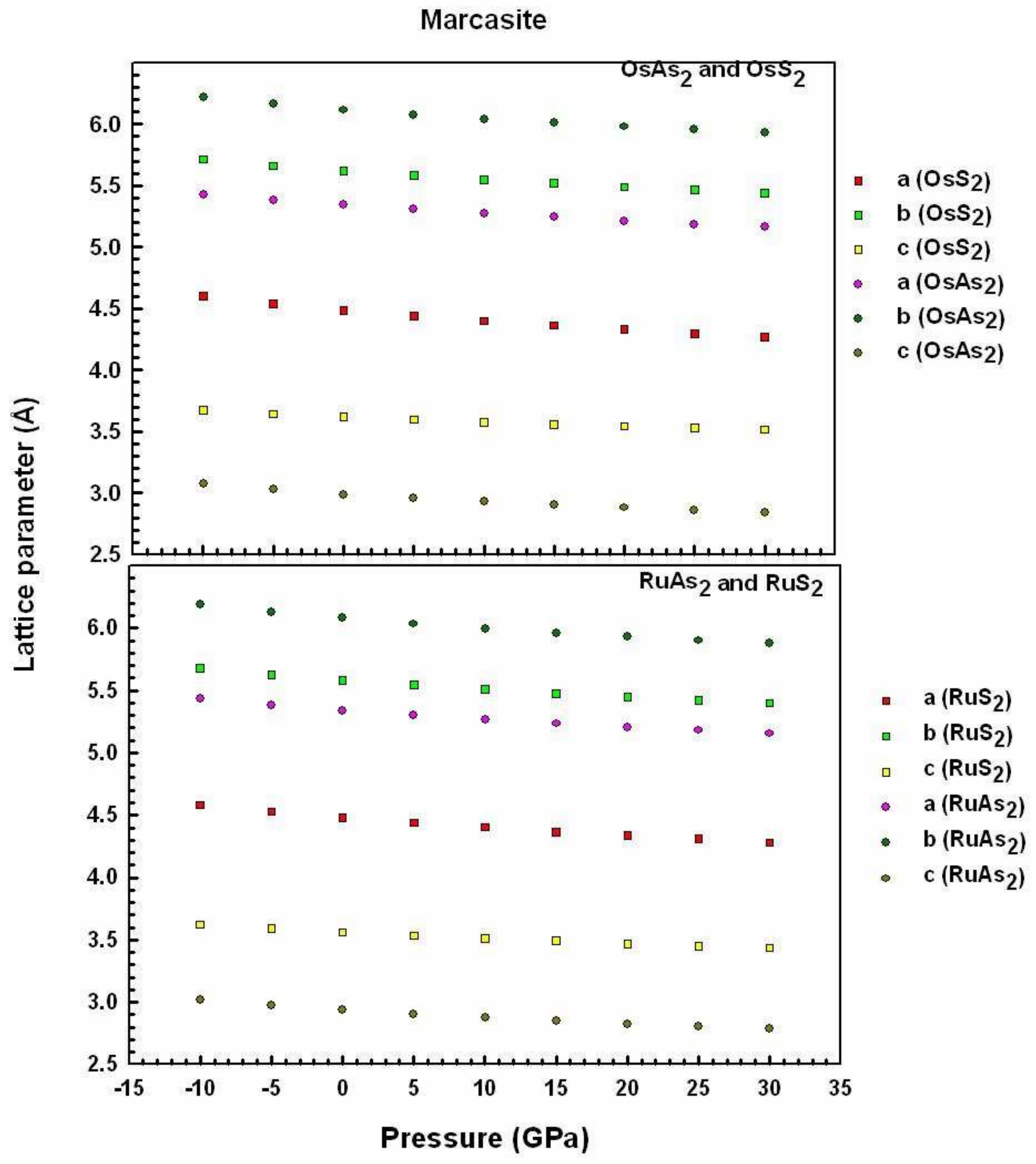

Figure 3.4: Lattice parameter as a function of applied hydrostatic pressure for the marcasite-type structures. The lattice parameter a, b and c are indicated for each structure explicitly.

ased for the structures OsS_2 and $OsAs_2$, where the lattice parameters *a* and *b* were predicted to have higher values for $OsAs_2$ than OsS_2. The plot for the lattice parameter *c* of OsS_2 lies above that of $OsAs_2$. Similarly as observed in pyrite-type (Figure 3.3), the As atoms forces the structures to increase in dimensions of *a* and *b* directions and the unit distance in the *c* direction actually decreases. The order of the parameters is observed to be $b > a > c$ in both structures. In the case of marcasite-type RuS_2 and $RuAs_2$, the plots show similar trends as those depicted for $OsAs_2$ and OsS_2, which is a clear indication that the marcasite-type structures have a similar trend under hydrostatic pressures.

3.6.2 Internal parameters

The dependence of the internal parameter, u as a function of hydrostatic pressure for the pyrite-type structures are shown in Figure 3.5. We note that the TMS have higher u values and lies top of the TMA which have small u values. The TMS (OsS_2, RuS_2) as well as the TMA ($OsAs_2$) plots show that u increases as the pressure is increased. We see that the difference in u value for TMS (OsS_2, RuS_2) is larger (≈ 0.002) at lower pressure (- 10 GPa) with the gap closing as the pressure is increased to 30 GPa. On the other hand, the converted pyrite-type TMA trend is different, the $RuAs_2$ decreases while for the $OsAs_2$ increases as the pressure is increased and the u values show large difference at higher pressure up to 50 GPa. As a result the plots coincide at about 5 GPa corresponding to u equals 0.379.

Figure 3.6 shows the dependence of internal parameters u and v as a function of the external hydrostatic pressure for marcasite-type structures. The plots for the u and v internal parameters are shown in the upper and lower panel, respectively. In a similar manner as the pyrite-types (Figure 3.3), the TMS plots are located above whereas those for the TMA are below in each panel. Recall that the TMA ($OsAs_2$, $RuAs_2$) real marcasite-types and TMS (OsS_2, RuS_2) are the converted marcasite-types.

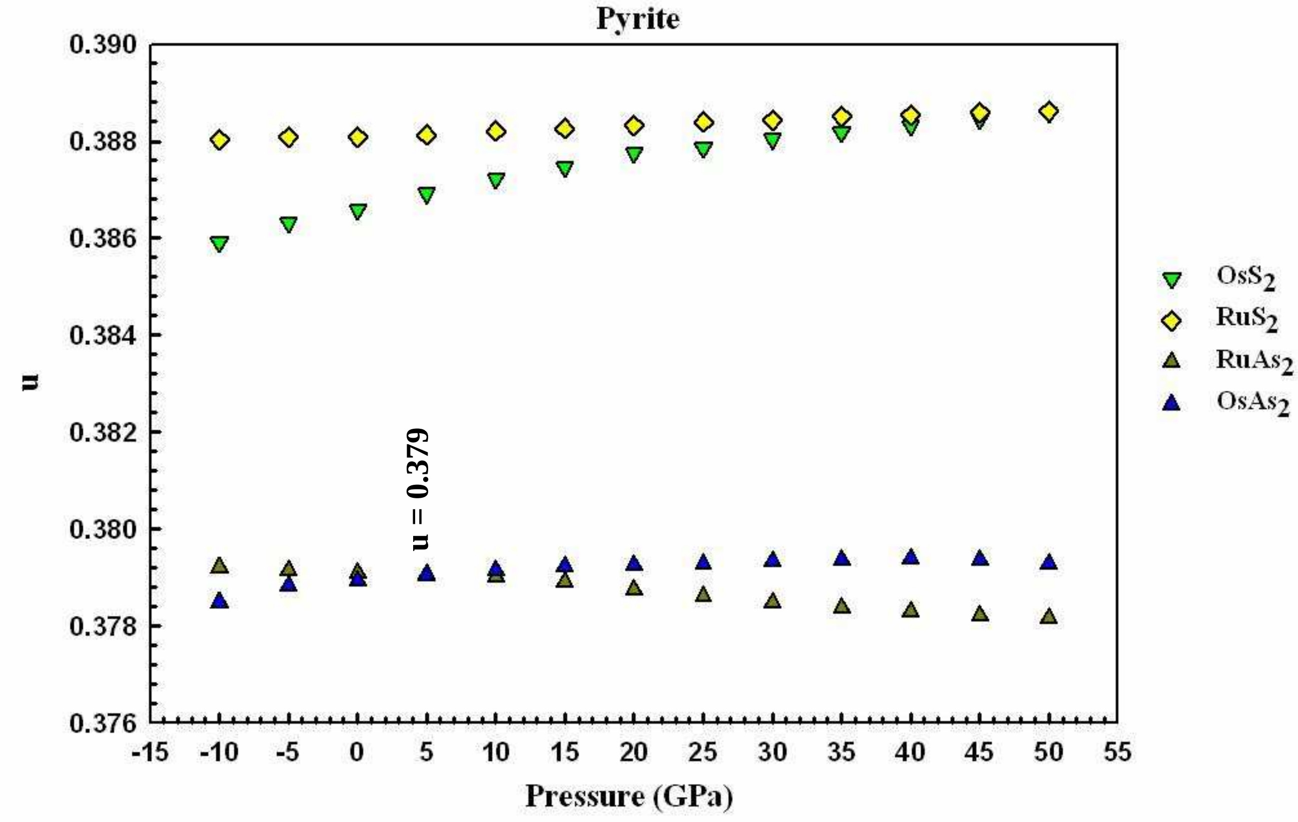

Figure 3.5: Internal parameter u as a function of pressure for the pyrite-type structures.

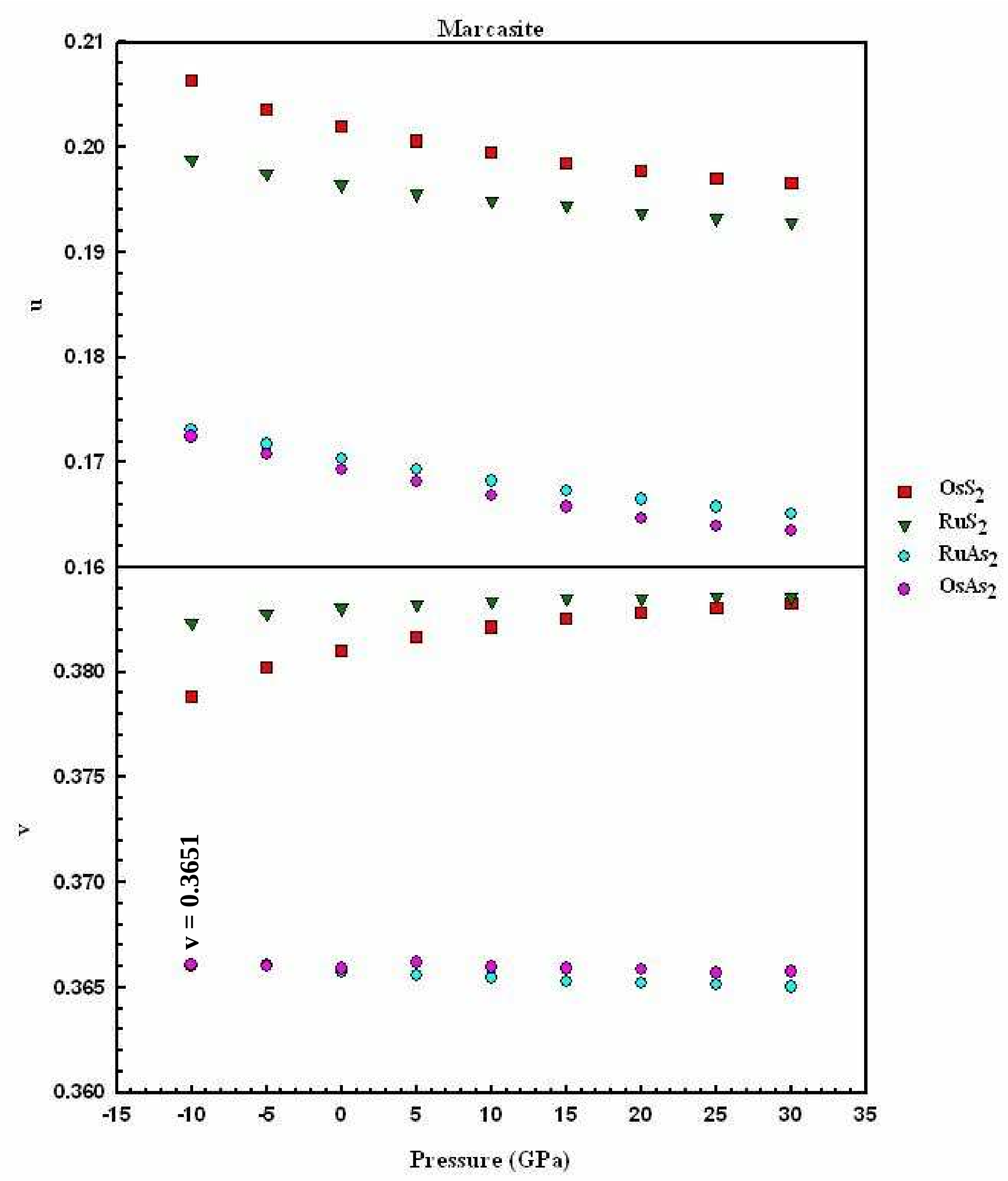

Figure 3.6: Internal parameters u and v as a function of pressure for the marcasite-type structures.

We see that in the upper panel (row), both the TMA and TMS curves show a decrease in u parameters as the pressure is increased. However, the u for the converted is further apart as compared to u for the real marcasite-type structures. The v parameter is different and we observe that the alternation of values with OsS_2 and $RuAs_2$ being the lowest. Moreover, we note that v increases with pressure for the converted TMS (OsS_2 and RuS_2) systems, whereas a slight decrease is observed for the real TMA ($OsAs_2$ and $RuAs_2$) systems. Their values coincide at lower pressure of about -10 to -5 GPa corresponding to v approximately equal to 0.3651.

3.6.3 Bond length at applied pressure

The dependence of bond length as a function of the applied external hydrostatic pressure for both pyrite- and marcasite-type structures is shown in Figure 3.7. The plots show that as pressure is increased, the bond lengths shorten for all the pyrite-type compositions. In the case of RuS_2 and OsS_2 plots, the S-S bond lengths decrease more rapidly than the Ru-S and Os-S bond lengths as pressure is increased. However, the case of $RuAs_2$ and $OsAs_2$ is different such that the As-As bond distances are always longer than the Ru-As and Os-As bond distances at various pressures. We also note the decreasing trends in the plots as pressure is increased, similar to the case of RuS_2 and OsS_2 structures.

Again, the plots show the dependence of bond lengths as a function of applied hydrostatic pressure of the marcasite-type structures. The plots predict that as pressure is increased, the bond lengths decrease for all the marcasite-type compositions. For the compositions RuS_2 and OsS_2, we see that the S-S bond distances shorten faster than the Ru-S and Os-S bond distances when pressure is increased. The Ru-S and Os-S bond distances are always greater than S-S bond distances. On the other hand, the compositions $RuAs_2$ and $OsAs_2$

predict the As-As bond lengths to decrease more rapidly than the Ru-As and Os-As bond lengths as pressure is increased, with As-As bond lengths always larger than Ru-As and Os-As bond lengths at various pressure range.

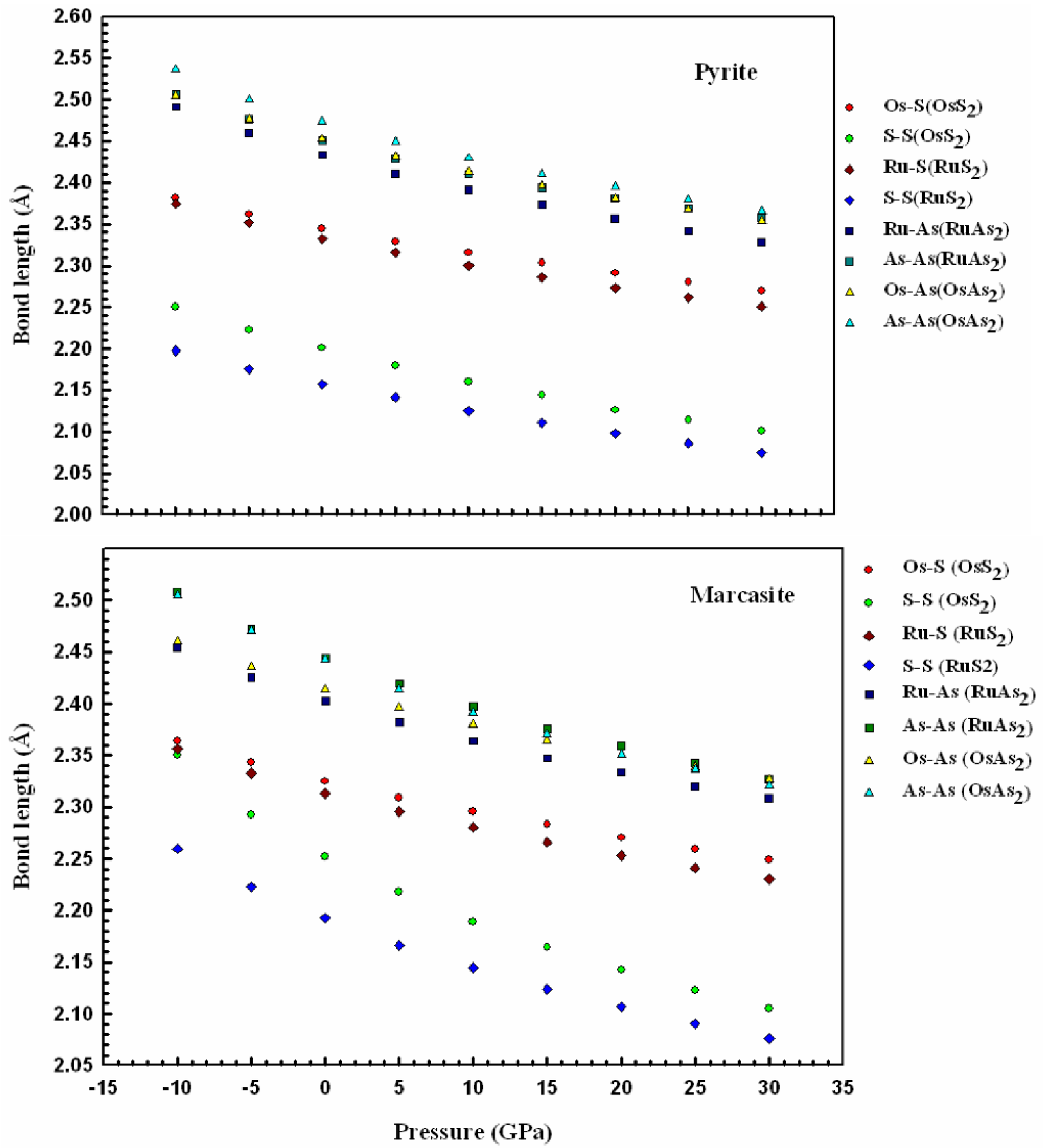

Figure 3.7: Bond length as a function of pressure for the pyrite- and marcasite-type structures.

CHAPTER 4

ELECTRONIC PROPERTIES

This chapter presents the electronic properties for TMA and TMS systems under study, in particular the total and partial densities of states and their corresponding band structures as well as the charge densities in both pyrite- and marcasite-type.

The DOS and the band structures analysis are necessary for determining whether the material is semiconducting, metallic or insulating by virtue of the size of energy gap produced between the highest occupied and the lowest unoccupied orbital. The charge density is important to determine the nature of bonding existing within these systems, in particular the dimer (S-S or As-As bond) and S(As)- M- S(As) bond.

4.1 Density of states and band structures at equilibrium

The calculated total and partial DOS and band structures for $OsAs_2$ in both pyrite- and marcasite-type structures are shown in Figures 4.1 and 4.2 respectively. The pyrite-type DOS (Figure 4.1 (a)) predict a metallic behaviour showing no energy gap (E_g) at the Fermi energy (E_F). This is as a result of strong hybridization of Os 5d and As 4p orbitals at E_F with the former being more predominant. We also note a high contribution of Os 5d states to the strong emission of the peak at energy of about -1.5 eV below the Fermi energy (E_F). The contribution of the As orbitals between the energies of about -2.9 eV and -5.5 eV is broader and gives a width of 2.6 eV associated with the 4p states. The contribution of As 4s orbitals is represented by two sharp peaks at about -10.0 eV and -12.0 eV. The corresponding band structure (Figure 4.1 (b)) clearly indicates that there is an overlap of the bands from the valence to conduction band, as a result no energy band

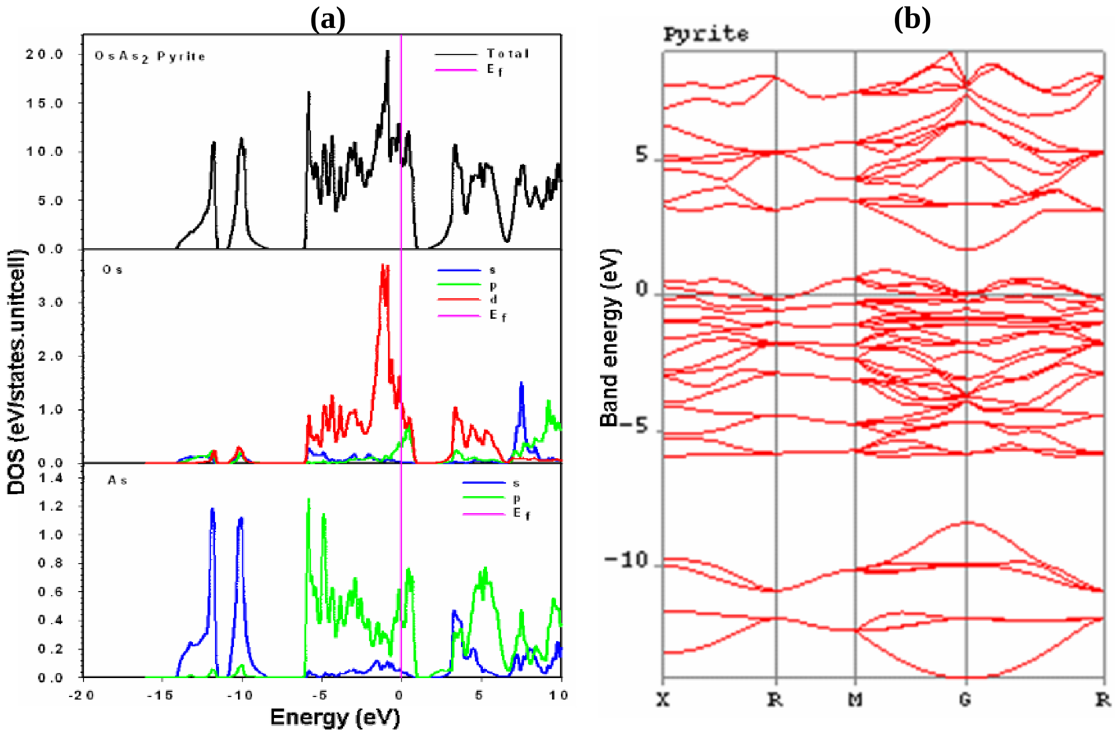

Figure 4.1: (a) Total and partial density of states and (b) energy band structure for pyrite-type OsAs$_2$. The Fermi level is taken as energy zero (E_F = 0).

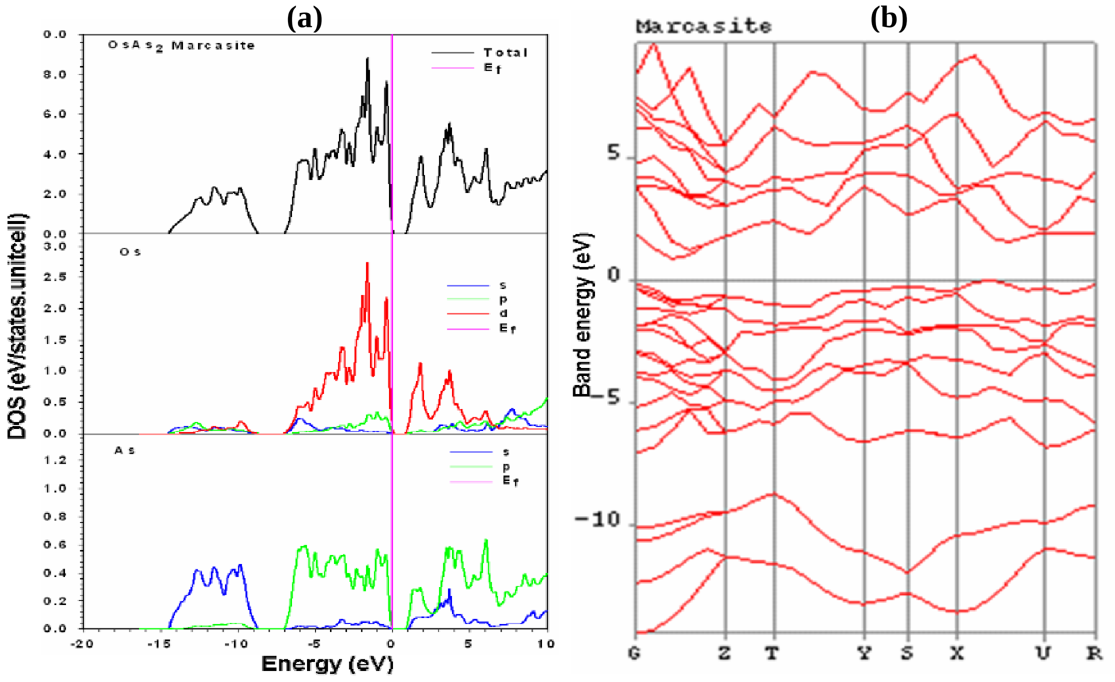

Figure 4.2: (a) Total and partial density of states and (b) energy band structure for marcasite-type OsAs$_2$. The Fermi level is taken as energy zero (E_F = 0).

gap is observed. This is consistent with our DOS analysis and confirms that the structure is metallic. Moreover, we also observe that the band structure is partitioned by about five groups of bands formed with respect to the contribution of Os and As atoms starting from band energy of 10.0 eV to -15.0 eV and are consistent with the total DOS peaks in the plot (Figure 4.1 (a)).

In Figure 4.2, we see that the marcasite-type structure $OsAs_2$ shows a semiconducting behaviour with energy gap (E_g) of 0.412 eV. We also observe the strongest emission of peak at energy of about -2.0 eV from the DOS contribution of Os 5d states below the Fermi energy (E_F). However, the 4s orbital contributions of the As atom is different from those of the pyrite-type $OsAs_2$ (Figure 4.1). At lowest energies, instead of the two sharp peaks, we note a broad band ranging from -9.0 eV to -15.0 eV giving rise to a width of 6.0 eV. Similarly, we observe about five groups of bands formed starting from band energy of -10 eV to 15 eV (Figure 4.2 (b)), except that the marcasite-type band structure shows a formation of a band gap as observed in the DOS plot (Figure 4.2 (a)) which was not seen in the pyrite-type structure DOS plot (Figure 4.1 (a)).

Figure 4.3 and 4.4 shows the total and partial DOS as well as the band structure of pyrite- and marcasite-type structures for OsS_2 respectively. The predicted DOS plot for OsS_2 pyrite-type (Figure 4.3 (a)) shows a semiconducting behaviour with the energy gap of 0.072 eV at Fermi energy. A strong emission of peaks at about -1.0 eV below the Fermi energy corresponds to the Os 5d states and the bands extending in OsS_2 pyrite-type from -7.4 eV to -2.9 eV which form a width of 4.5 eV are associated with the S 3p states, while other 3p states are shifted above the Fermi energy. Emission of peaks at about -14.8 eV and -12.3 eV correspond to the S 3s orbitals. The corresponding band structure

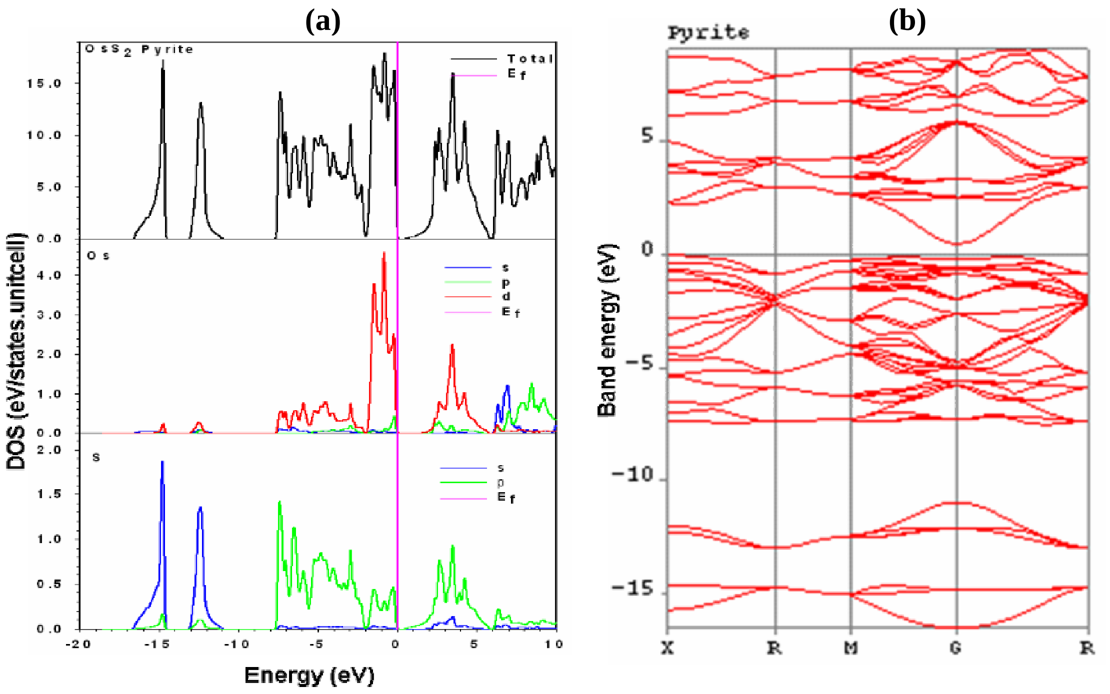

Figure 4.3: (a) Total and partial density of states and (b) energy band structure for pyrite-type OsS_2. The Fermi level is taken as energy zero ($E_F = 0$).

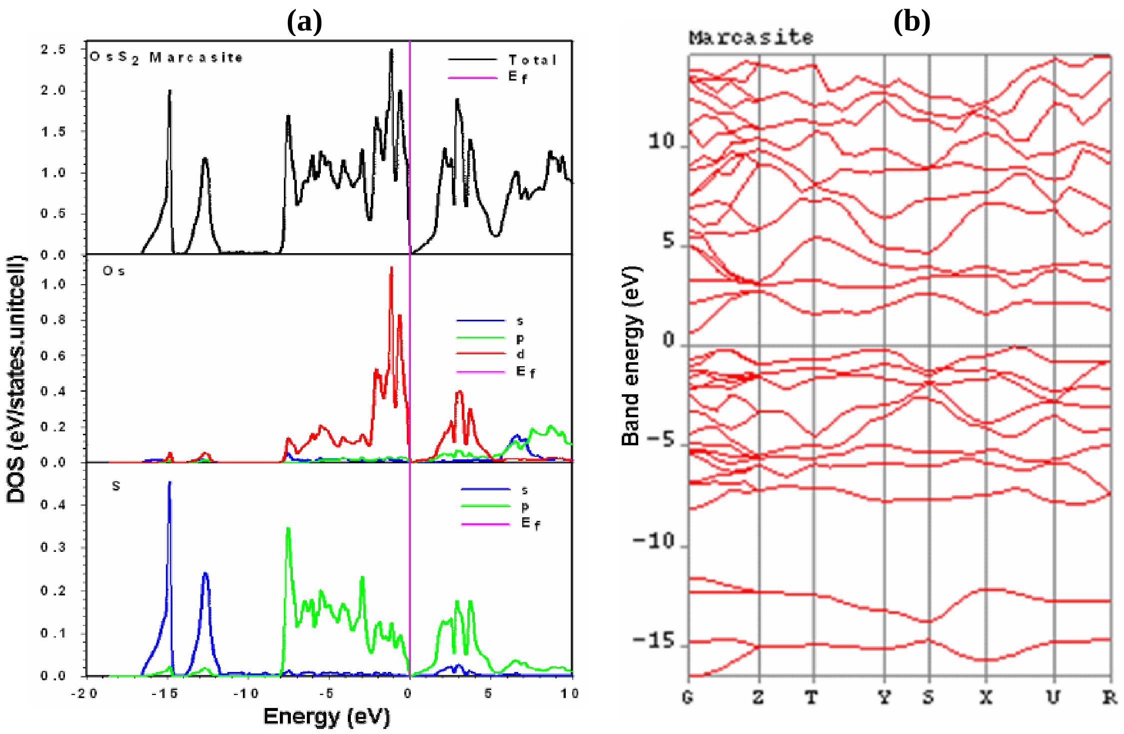

Figure 4.4: (a) Total and partial density of states and (b) energy band structure for marcasite-type OsS_2. The Fermi level is taken as energy zero ($E_F = 0$).

(Figure 4.3 (b)) confirms that the energy gap is observed; similarly the band structure is partitioned into about five groups at the band energies ranging from -10 eV to 15 eV. The marcasite-type OsS_2 DOS and band structure in Figure 4.4 shows a similar trend as those for pyrite-type OsS_2 (Figure 4.3) discussed above. However, their energy band gaps are different where the pyrite-type has smaller band gap of 0.072 eV compared to 0.477 eV for the marcasite-type structure.

The total and partial DOS as well as the band structure for $RuAs_2$ pyrite- and marcasite-type structures are shown in Figures 4.5 and 4.6 respectively. In a similar manner, the DOS of the pyrite-type (Figure 4.5 (a)) predict a metallic behaviour showing no energy gap (E_g) at the Fermi energy (E_F) as in Figure 4.1(a). The contribution of Ru 4d states give rise to the higher peak at energy of about -1.5 eV below the Fermi energy (E_F), where the contribution of As 4s orbitals is represented by two sharp peaks at about -10.0 eV and -12.0 eV. The energy band structure (Figure 4.5 (b)) shows similar behaviour as those in Figure 4.1 (b) above, and no energy band gap is observed. This is consistent with our DOS analysis and confirms that the structure is metallic.

Figure 4.6 (a) show DOS plot for marcasite-type $RuAs_2$ structure with similar trend as in Figure 4.2 (a) with energy band gap of about 0.289 eV. Higher peaks are observed at energy of about -2.0 eV below Fermi energy (E_F) which are associated with the contribution of Ru 4d states, with the contribution of As 4s orbitals different from those of the pyrite-type $RuAs_2$ (Figure 4.5 (a)) at lower energies of about -9.0 eV to -15.0 eV. The band structure for marcasite-type $RuAs_2$ (Figure 4.6 (b)) show about five groups of bands with a band gap at 0.0 eV confirming the one observed from the total DOS plot (Figure 4.6 (a)) and the pyrite-type $RuAs_2$ shows no energy band gap.

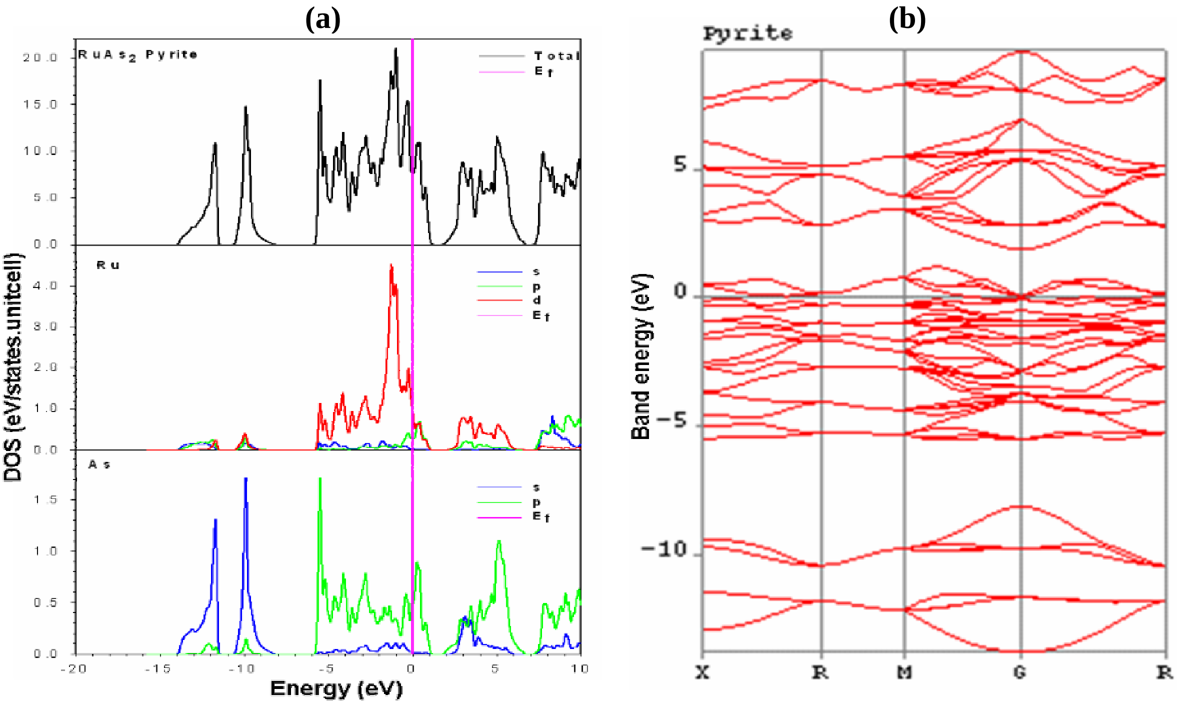

Figure 4.5: (a) Total and partial density of states and (b) energy band structure for pyrite-type RuAs$_2$. The Fermi level is taken as energy zero (E_F = 0).

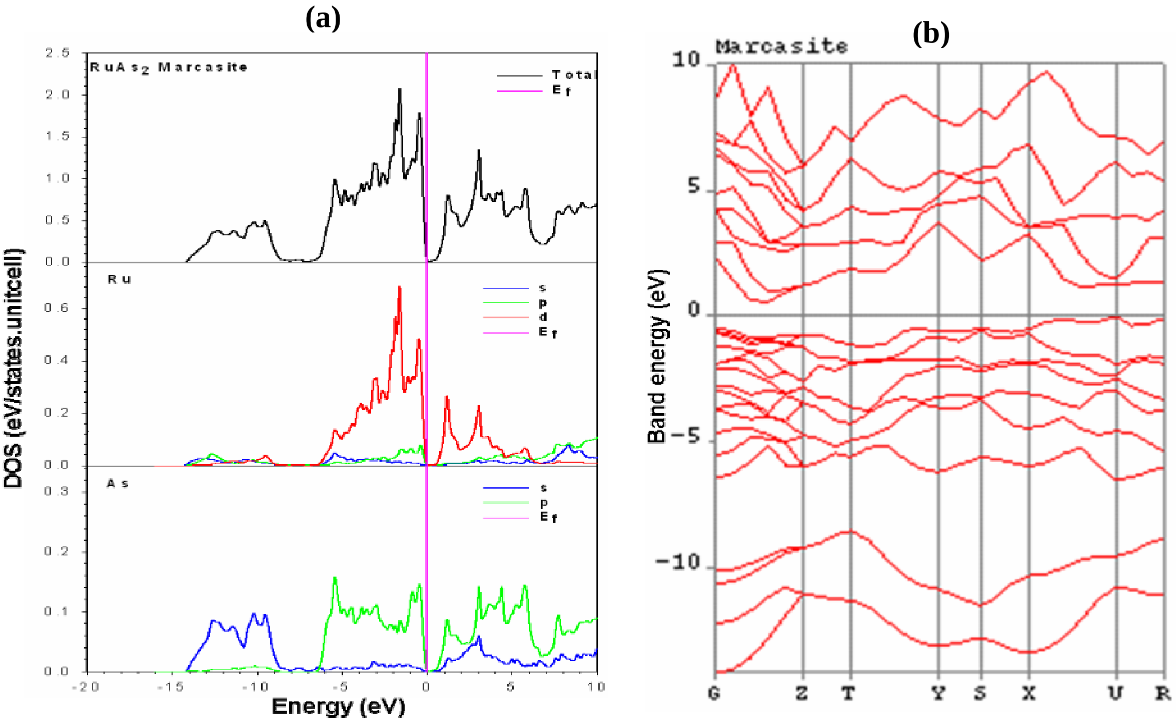

Figure 4.6: (a) Total and partial density of states and (b) energy band structure for marcasite-type RuAs$_2$. The Fermi level is taken as energy zero (E_F = 0).

The total and partial DOS together with the band structure of pyrite- and marcasite-type structures for RuS_2 are shown in Figure 4.7 and 4.8 respectively. RuS_2 pyrite-type DOS plot (Figure 4.7 (a)) depicts a semiconducting behaviour with the energy band gap of 0.577 eV at Fermi energy which is in excellent agreement to within 3 % to the one reported by Raybaud et al [Raybaud et al, 1997]. Our calculated energy gap underestimated 0.84 eV reported by Holzwarth et al [Holzwarth et al, 1985] to within 31 %. Higher peaks are observed at about -1.5 eV below the Fermi energy corresponding to the contribution of Ru 4d states and the contribution of S 3p states are observed from energy of about -7.0 eV to -2.5 eV, with 3p states shifted above the Fermi energy. Again, we note that S 3s orbitals contributed to the peaks at about -15.0 eV and -12.0 eV. Figure 4.7 (b) shows the corresponding band structure for the pyrite-type RuS_2, confirming the energy band gap observed from the DOS plot, with the band structure partitioned into about five groups of bands similar to that in Figure 4.3 (b).

Similar trend is observed for the marcasite-type RuS_2 DOS and band structure in figure 4.8 as those of pyrite-type RuS_2 (Figure 4.7) discussed above, with their energy band gaps giving a difference of about 0.18 eV.

In summary, the converted pyrite-type structures $OsAs_2$ and $RuAs_2$ give no energy band gap at E_F which shows a metallic behaviour unlike the naturally occurring marcasite-type structures $OsAs_2$ and $RuAs_2$. On the other hand, the converted marcasite-type structures OsS_2 and RuS_2 depict bigger energy band gaps than the naturally occurring pyrite-type structures OsS_2 and RuS_2 showing semiconducting behaviour.

The energy band gaps for the TMA and TMS systems in both pyrite- and marcasite-type structures are given in table 4.1. The values for the naturally occurring pyrite-type

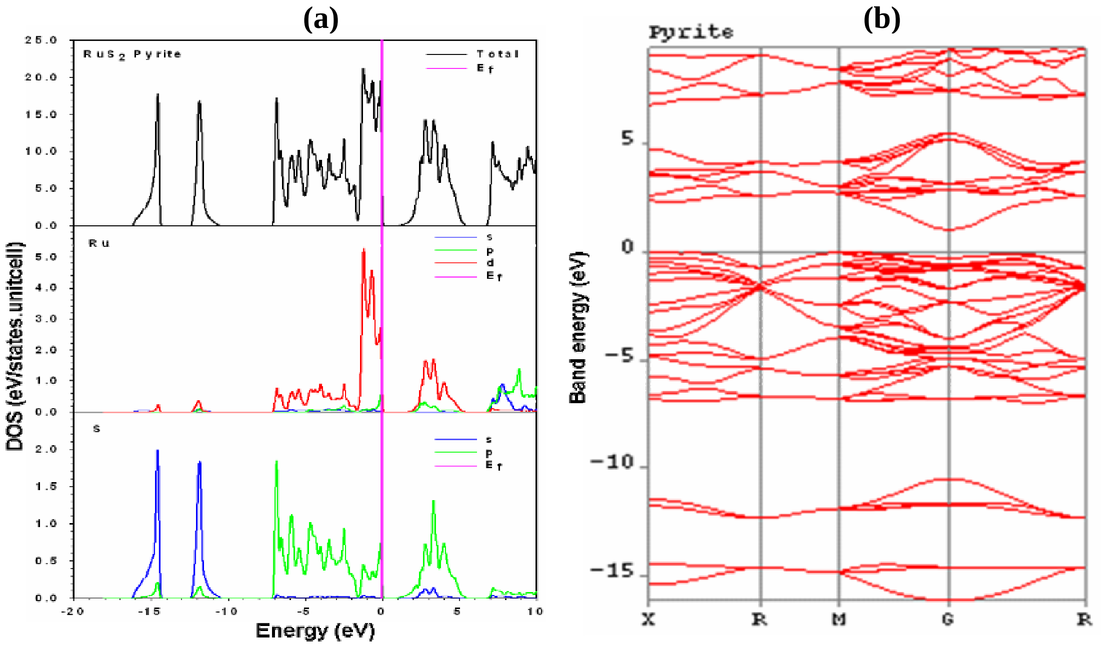

Figure 4.7: (a) Total and partial density of states and (b) energy band structure for pyrite-type RuS_2. The Fermi level is taken as energy zero ($E_F = 0$).

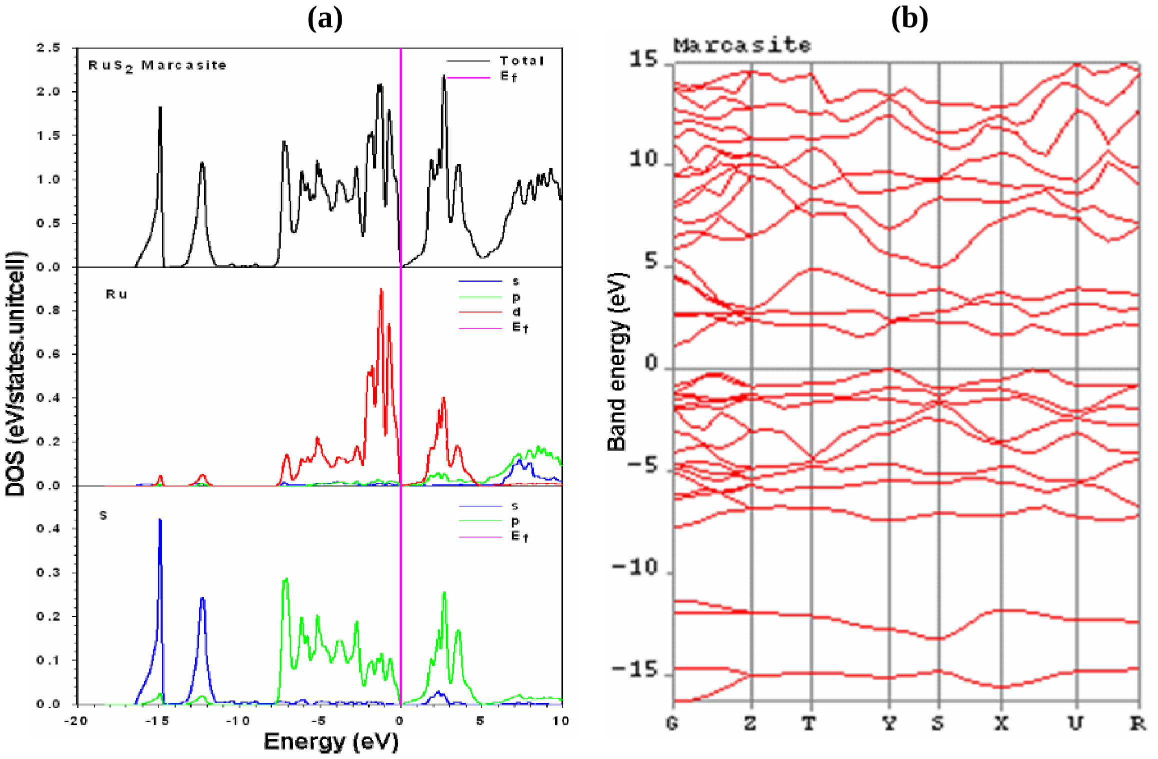

Figure 4.8: (a) Total and partial density of states and (b) energy band structure for marcasite-type RuS_2. The Fermi level is taken as energy zero ($E_F = 0$).

structures OsS_2 and RuS_2 agrees to within 13 % and 3 % respectively as compared to those reported by Raybaud et al [Raybaud et al, 1997]. We also note that $OsAs_2$ and $RuAs_2$ does not have a band gap (metallic behaviour) and hence they are not comfortable as pyrite-type structures, whereas the OsS_2 and RuS_2 structures showing various band gaps (semiconducting behaviour) are comfortable as marcasite-type structures with larger band gaps than as pyrite-type structures.

Table 4.1: Energy band gaps for TMA and TMS using CASTEP code, compared with available data where possible.

Structure	Composition	Energy gap (eV)
$OsAs_2$	**Pyrite**	0.000
	Marcasite	0.412
$RuAs_2$	**Pyrite**	0.000
	Marcasite	0.289
OsS_2	**Pyrite**	0.096(0.110*)
	Marcasite	0.477
RuS_2	**Pyrite**	0.577 (0.560*)
	Marcasite	0.757

* Raybaud et al, 1997

Figure 4.9 shows a comparison of the total DOS for both pyrite- and marcasite-type plotted in one panel (row) for each structure. The Fermi level is taken as the energy zero ($E_F = 0$), and we observe the presence of energy band gap (E_b) with respect to E_F more precisely. In order to show the trend of DOS at E_F, we reduced the energy scale from -5 to 5 eV. The DOS for the naturally occurring pyrite-type (OsS_2 and RuS_2) and the converted marcasite-type (OsS_2 and RuS_2) structures show similar trend and we observe energy band gaps near the E_F. This validates the fact that the pyrite- and marcasite-type (OsS_2 and RuS_2) have good semiconducting behaviour. The contribution of the 5d Os atom and the S atom on OsS_2 reduces the energy band gap and the contribution of the 4d Ru atom with the S atom on RuS_2 increases the energy band gap in both pyrite- and marcasite-type structures.

The naturally occurring marcasite-type structures ($OsAs_2$ and $RuAs_2$), with energy band gaps at E_F and the converted pyrite-type structures ($OsAs_2$ and $RuAs_2$), with no energy band gaps at E_F, show different trends as we observe higher peaks for pyrite-types and lower peaks for marcasite-types at energies ranging from -2.50 eV to -1.0 eV. This implies that marcasite-type ($OsAs_2$ and $RuAs_2$) are good semiconductors and pyrite-type ($OsAs_2$ and $RuAs_2$) are good in metallic applications. The 5d Os atom, with the As atom contributions on $OsAs_2$ increases the energy band gap and the 4d Ru atom, with the As atom contributions on $RuAs_2$ reduces the energy band gap for both pyrite- and marcasite-type structures.

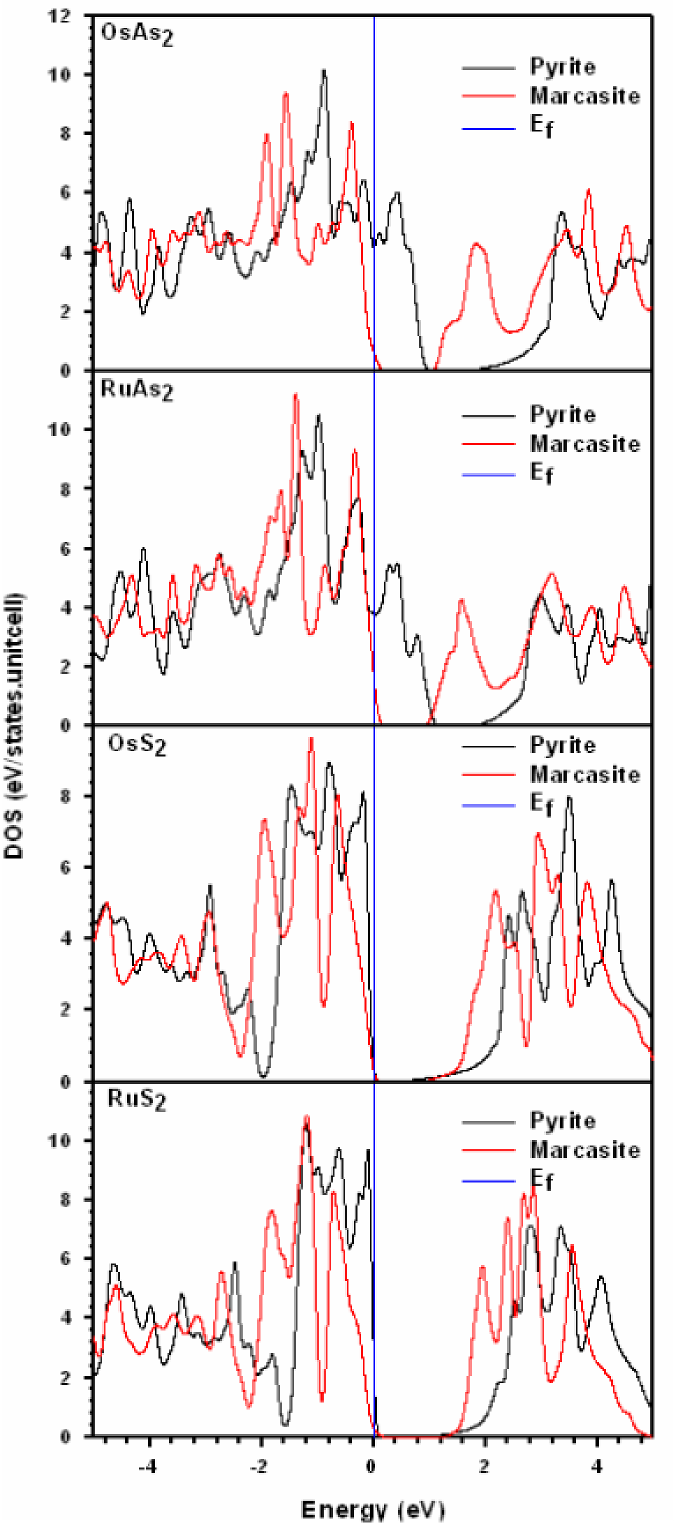

Figure 4.9: Total density of states for pyrite- and marcasite-type structures. The Fermi level is taken as energy zero ($E_F = 0$).

4.2 Charge density

The electronic charge density and charge density differences for the TMA and TMS systems in both pyrite- and marcasite-type have been calculated using the plane wave pseudopotential code CASTEP. The contour plots were chosen from the planes which contain the nearest-neighbours M-M, M-X, X-X (M = Os, Ru and X = S, As) bonds for all structures. The charge density plots would highlight the concentration/ population of charges around individual atoms while the charge density difference plots will predict the nature of bonding between any pair of two atoms that exists in a material. In order to capture all types of bonding, we analyse the slides for the pyrite-type structures in the [110] direction in a plane containing (110) axes while the marcasite-type structures are analysed in the [0 01] direction in a plane containing (001) axes.

Note that we will only discuss the charge density and charge density difference for one naturally occurring and one converted pyrite- and marcasite-type structures since all the bonding behaviour and trend are represented. Their charge densities and charge density difference plots are shown in Figures 4.10 to 4.13 respectively. In these plots the red colour indicates a high density of electronic charge (charge gain), the green colour signifies a neutral region between the atoms and the blue colour shows a less density of electronic charge (charge loss) around an atom.

Figure 4.10 shows the charge density and charge density difference plots for the naturally occurring pyrite-type RuS_2 structure. From the total charge density plot (figure 4.10), we observe a zig-zig bonding pattern between the nearest-neighbours Ru-S and S-S bonds. This observation is consistent with those exhibited from the valence charge density for pyrite-type RuS_2 in a plane containing (110) and (001) axes by Holzwarth et al

[Holzwarth et al, 1985]. The charge density (Figure 4.10 (a)) shows a higher concentration of charge around the Ru atoms (red colour) and more charges which are less concentrated around S atoms with regions between Ru atoms showing small amount of charges. The charge density difference (Figure 4.10 (b)) shows directionality of bonding between Ru-S, S-S and Ru-Ru. The Ru d-orbitals are clearly visible and we note a strong bonding between Ru-S which signifies some oval shape directionality of Ru charge elongating towards the S atom, hence showing covalent bond between Ru and S atoms. However, the interaction Ru-Ru shows an ionic bonding because the formation of bond is spherical with the S-S bond been less spherical and depicting weak ionic bonding within the dimer pair.

The naturally occurring pyrite-type OsS_2 structure gives similar trends as the RuS_2 and also bonding between Os-S, Os-Os and the dimmer pairs S-S looks similar to the Ru-S, Ru-Ru and S-S and it was convenient to show only the plots for one structure i.e. RuS_2. Moreover, a mixture of covalent and weak ionic bonding was observed for pyrite-type OsS_2 similar to the RuS_2 structure.

The charge density and charge density difference plots for the converted pyrite-type structure $OsAs_2$ are shown in Figure 4.11. We realize that Os-As, As-As and Os-Os bonding occurs in a zig-zig pattern similar to the naturally occurring pyrite-type structures RuS_2 charge density plot. The charge density plot (Figure 4.11 (b)) depicts that there is a high concentration of charge shown by the red colour around the Os atoms and less concentration of charges around the As atoms. From the charge density difference plot, we note that the As-As dimer pairs been less spherical which implies weak ionic bonding. The Os-As region indicates some oval shape directionality of Os charge

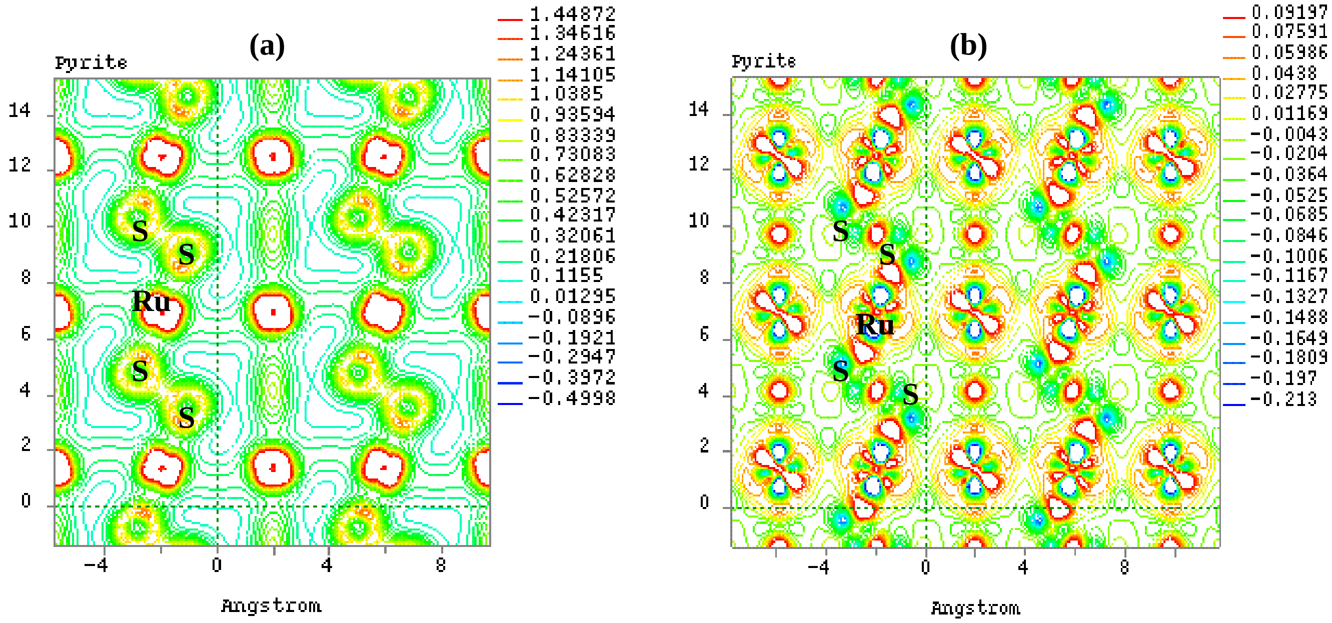

Figure 4.10: Electronic (a) charge density and (b) charge density difference for pyrite-type RuS_2 projected in the (110) plane.

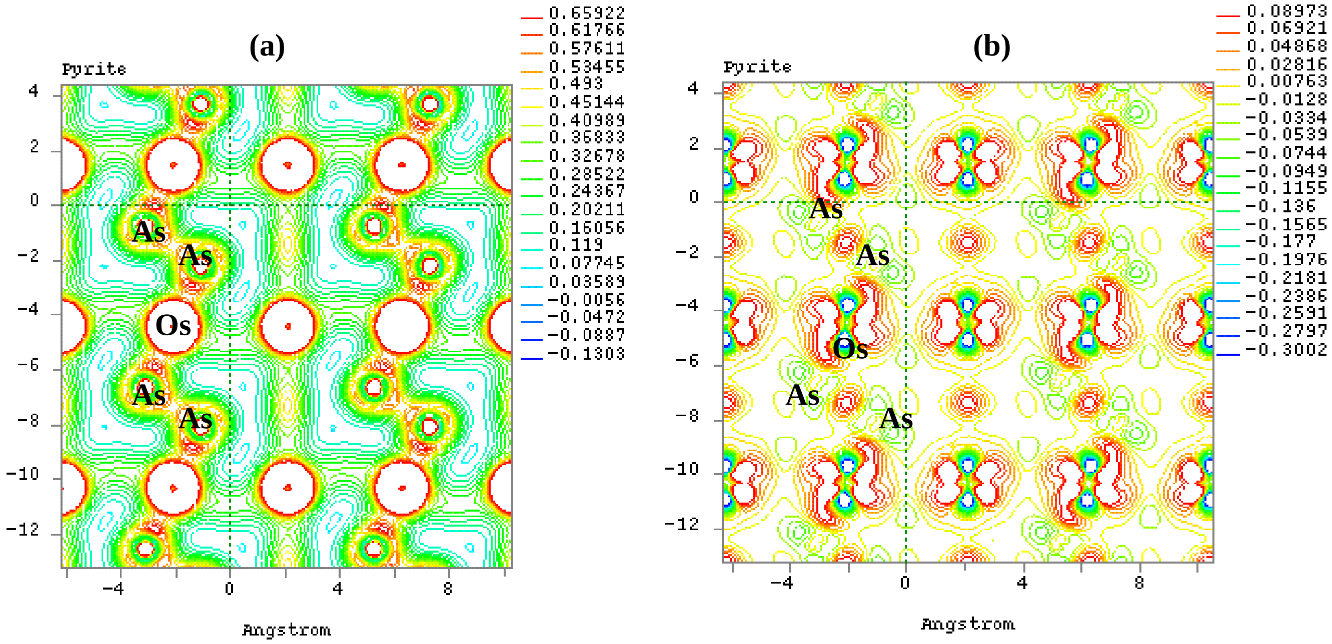

Figure 4.11: Electronic (a) charge density and (b) charge density difference for pyrite-type $OsAs_2$ projected in the (110) plane.

elongating towards the As atom, hence prompting the covalent bond between the two ions. The interaction Os-Os is an ionic bonding since there is a spherical formation of the bond between the Os atoms. Thus $OsAs_2$ pyrite-type structure depicts covalent bonding along the Os-As and weak ionic bonding between As-As pairs and ionic bonding within the Os-Os ions. Hence the structure has a complex mixture of bonding (covalent, ionic and weak ionic). On the other hand, the converted pyrite-type structure $RuAs_2$ predicted similar trends as $OsAs_2$ for the charge density and charge density difference, with the nature of bonding occurring between the Ru-As, Ru-Ru and As-As for the $RuAs_2$ structure similar to $OsAs_2$ structure.

The charge density and charge density difference for the naturally occurring marcasite-type structure $OsAs_2$ are shown in Figure 4.12. From the plots, we are capable of analyzing the bonding pattern and the nature of bonding between the Os-Os, Os-As and As-As. The charge density plot (Figure 4.12 (a)) shows that there is a zig-zig bonding pattern between the Os and As atoms. Furthermore, the charge density depicts that there is a blue colour around the Os atoms which implies a charge loss and the red colour around the As atoms is depicted which signifies charge gain. From the charge density difference (Figure 4.12 (b)), we observe that the region Os-As show the oval shape directionality of Os charge extending towards the As, hence implying a covalent bond between the two ions. However, the As-As bond is less spherical, indicating weak ionic bonding in the dimmer pairs. The Os-Os region shows a depleted formation of bond between the two transition metals and we can say that there is no bonding between Os atoms. Similar trend for the charge density and charge density difference plots for the naturally occurring marcasite-type structure $RuAs_2$ were observed. We notice that a

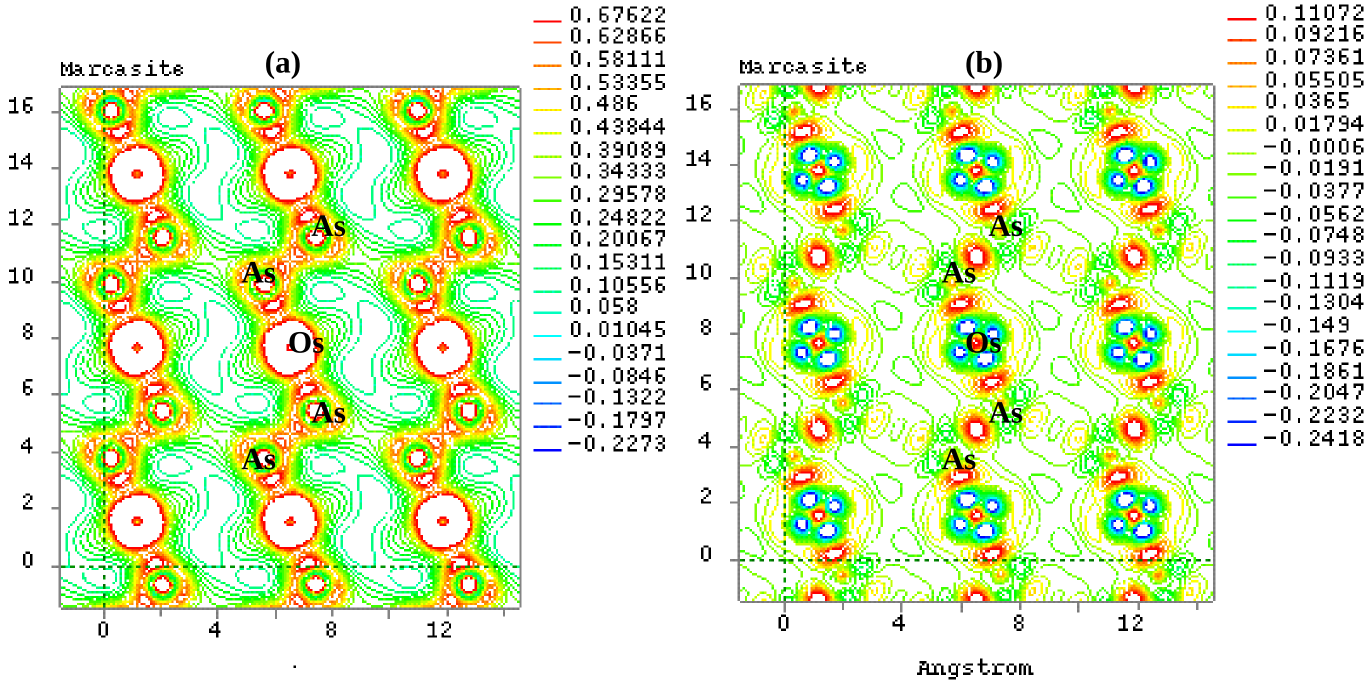

Figure 4.12: Electronic (a) charge density and (b) charge density difference for marcasite-type $OsAs_2$ projected in the (001) plane.

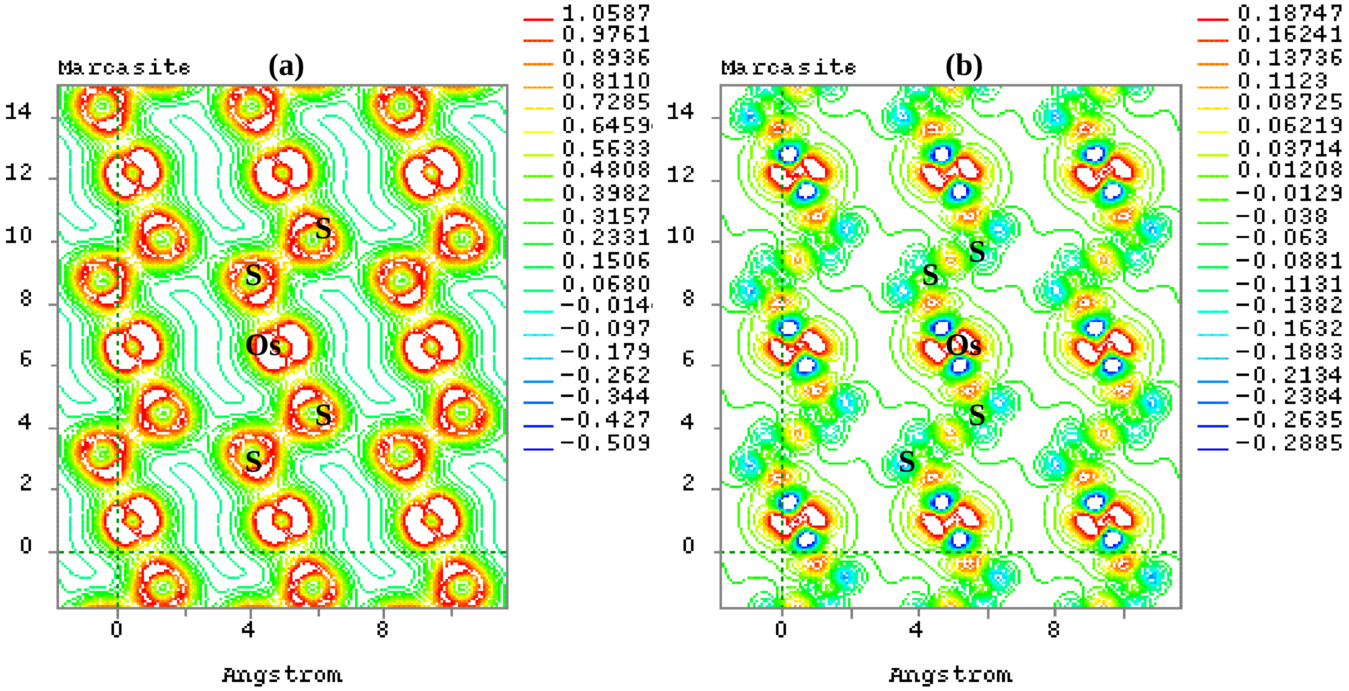

Figure 4.13: Electronic (a) charge density and (b) charge density difference for marcasite-type OsS_2 projected in the (001) plane.

mixture of bonding (covalent and weak ionic) occurs for this naturally occurring marcasite-type structures.

Figure 4.13 shows the charge density and charge density difference plots for the converted marcasite-type structure OsS_2. We observed similar pattern of bonding as the naturally occurring marcasite-type $OsAs_2$ from the charge density plot which clearly indicates bonding Os-S and the dimer pairs S-S. The charge density plot (Figure 4.13 (a)) depicts that S atoms gained some charges due to the red colour around them and the Os atoms seems to have lost charges to the S atoms with the blue colour surrounding them. Charge density difference plot (Figure 4.13 (b)) shows that region Os-S has some covalent bonding because of the oval shape directionality of Os charge towards S atom. The S-S bonding is less spherical, which signifies weak ionic bonding. We note that there is no bonding between the Os atoms from the plot as in the $OsAs_2$ structure.

However, RuS_2 converted marcasite-type structure shows the same trend in bonding and also in the nature of bonding with OsS_2 structure. As such it was worthy enough to show only the plots for the OsS_2.

Generally we can conclude that bonding in marcasite-type structures is mainly covalent between the Os-As, Os-S, Ru-As and Ru-S pairs, with a mixture of weak ionic bonding within As-As and S-S regions.

CHAPTER 5

OPTICAL PROPERTIES

In this chapter, we discuss the optical properties for the TMA and TMS systems under study, in particular the absorption and reflectivity spectra in both pyrite- and marcasite-type. Furthermore, we will also investigate the influence of pressure on the absorption and reflectivity spectra for these structures.

Background

Generally, the difference in the propagation of an electromagnetic wave of the minerals through vacuum and some other materials can be described by a complex refractive index,

$$N = n + iK \ . \tag{5.1}$$

In vacuum the refractive index, N is real and equal to unity. It is purely real for the transparent materials and the imaginary part being related to the absorption coefficient by,

$$\eta = \frac{2k\omega}{c} \tag{5.2}$$

the fraction of energy lost by the wave on passing through a unit thickness of the material concerned. For the simple case of normal incidence on a plane surface, the reflection coefficient can be obtained by matching both the electric and magnetic fields at the surface as,

$$R = \left|\frac{1-N}{1+N}\right|^2 = \frac{(n-1)^2 + K^2}{(n+1)^2 + K^2} \ . \tag{5.3}$$

However, when performing calculations of optical properties it is common to evaluate the complex dielectric constant, and then other properties would be expressed in terms of it. The complex dielectric constant $\varepsilon(\omega)$ is given by

$$\varepsilon = \varepsilon_1 + i\varepsilon_2 = N^2 \tag{5.4}$$

where ε_1 and ε_2 are the real and imaginary constants respectively. Hence the relation between the real and imaginary parts of the refractive index and dielectric constants is,

$$\begin{aligned} \varepsilon_1 &= n^2 - K^2 \\ \varepsilon_2 &= 2nK\ . \end{aligned} \tag{5.5}$$

Furthermore a frequent form of optical properties is the optical conductivity given by the expression,

$$\sigma = \sigma_1 + i\sigma_2 = -i\frac{\omega}{4\pi}(\varepsilon - 1)\,. \tag{5.6}$$

Mostly, this is useful for metals. Furthermore, a property which may be calculated from the complex dielectric constant is the loss function, which describes the energy lost by a point electron passing through a homogeneous dielectric material, and is given by,

$$\mathrm{Im}\left(\frac{-1}{\varepsilon(\omega)}\right). \tag{5.7}$$

In experiment, the absorption $\eta(\omega)$ and the reflection $R(\omega)$ coefficients are the most accessible optical parameters. In principle, given the knowledge of both the real and imaginary parts of N can be determined. However, in practice, the experiments are more complicated than the case of the normal incidence considered above. Polarization effects should be accounted for, and the involvement of the geometry can be quite considerable (for example, transmission through multi-layered films or incidence at a general angle).

Only transitions between properly selected bands are allowed i.e. only bands with the same sign of spin [Phillip, 1977].

We describe the interaction of a photon with the electrons for the TMA and TMS under study in terms of the time dependent perturbations of the ground state electronic states. The electric field of the photon leads to the transition between occupied and unoccupied states (the magnetic field effect is weaker by a factor of v/c). The collectiveness of these excitations is referred to as plasmons (which are most easily observed by the passing of a fast electron through the system rather than a photon, in a technique known as Electron Energy Loss Spectroscopy (EELS) [Fischer et al, 1985], since transverse photons do not excite longitudinal plasmons). The transitions are known to be single particle excitations when they are independent. These excitations result in spectra which can be thought of as a joint density of states between the valence and conduction bands, weighted by appropriate matrix elements.

5.1 Absorption and reflectivity spectra

The absorption curves against frequency energy for the naturally occurring (RuS_2 and OsS_2) and converted ($OsAs_2$ and $RuAs_2$) pyrite-type structures are shown in Figure 5.1. The naturally occurring absorption curves are compared in Figure 5.1 (a) together with the experimental plot for RuS_2 by Vaterlaus et al [Vaterlaus et al, 1985]. The absorption curves show similar trend as the experimental and increases as the frequency energy increases, despite their absorption and frequency range being slightly different. The absorption curve for the converted phase of $OsAs_2$ and $RuAs_2$ are shown in Figure 5.1 (b) and (c) respectively. We see that their absorption is higher up to 10^8 and 10^9 cm^{-1} whereas for the naturally occurring pyrite-types is at 10^5 cm^{-1}. This suggests that $OsAs_2$

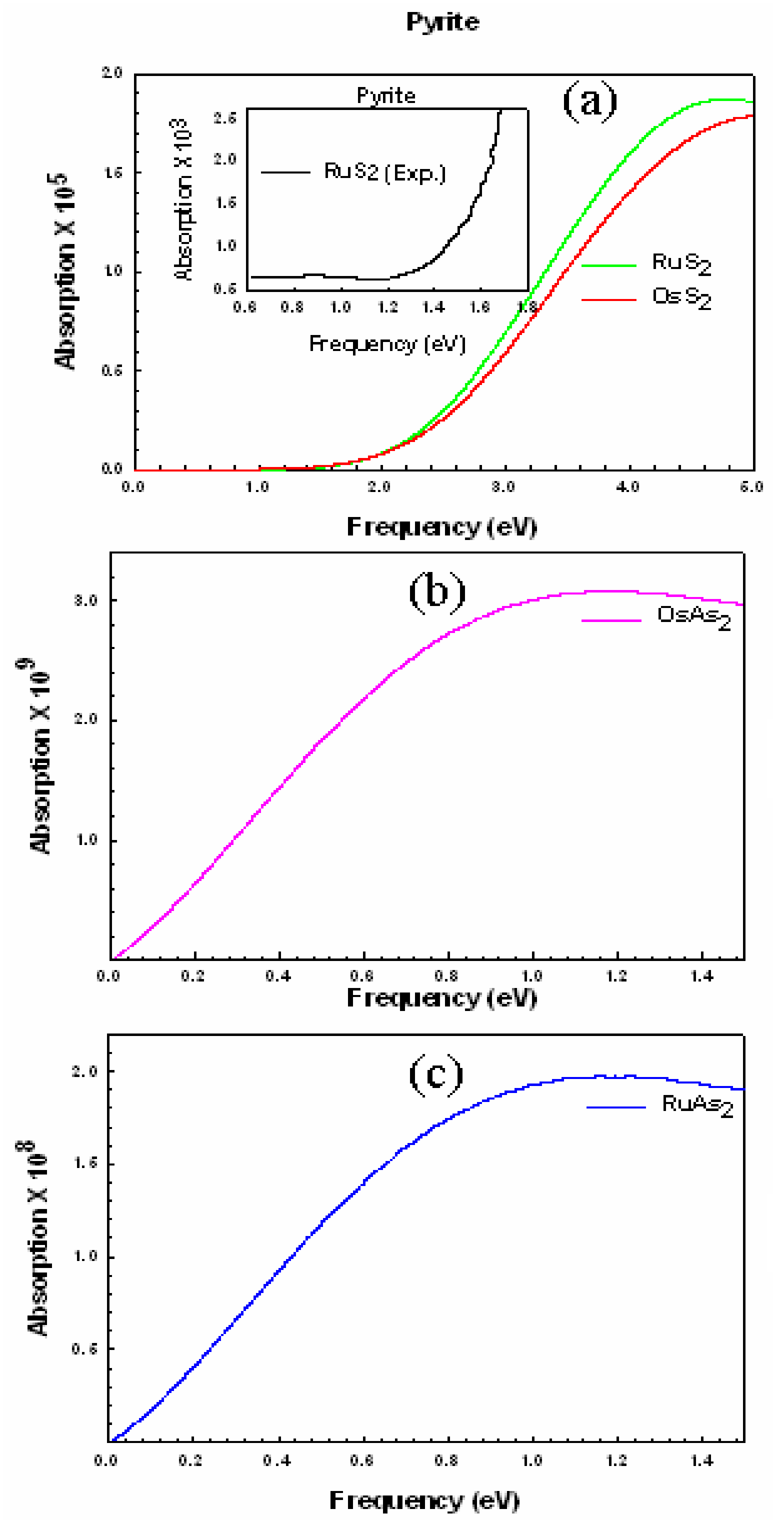

Real

Converted

Converted

Figure 5.1: Absorption spectra in units of cm^{-1} against frequency (eV) for pyrite-type structures.

and $RuAs_2$ are less stable as pyrite-types since they are highly absorbing. Furthermore, we observe that RuS_2 and OsS_2 absorption curves reaches a maximum at frequency energy of about 4.5 and 4.9 eV respectively with the later being predominant. The experimental [Vaterlaus et al, 1985] absorption curve reaches a maximum by 1.6 eV much less compared to our predicted spectra. RuS_2 show high absorption at frequency energy of about 4.5 eV with a difference of about 2.9 eV compared to the experimental. However, OsS_2 show higher absorption at high frequency energy (4.9 eV) than RuS_2 and these correspond with the high peaks at low energies from the DOS predictions in the previous chapter.

Recently the optical properties of the pyrite RuS_2 structure have been investigated using different approaches owing to its band gap being the subject of much controversy. Originally the band gap of 1.8 eV was accepted which was based on diffuse optical reflection measurements on the powdered samples [Hulliger, 1963]. However, our calculated absorption spectra for both RuS_2 and OsS_2 structures (Figure 5.1 (a)) predict the energy band gap of about 1.4 eV and 1.0 eV respectively. On the other hand Bichsel et al (1984), estimated the energy gap of a single crystal to be 1.3 from the optical absorption measurements with the reflection coefficient being assumed to be constant [Bichsel et al, 1984] while Guittard et al suggested a value of 1.3 eV to 1.5 eV [Guittard et al, 1980]. This is evident that our predicted band energy gap of 1.4 eV from the RuS_2 absorption curve agrees well with most experimental values.

Figure 5.2 shows the reflectivity curve against the frequency energy for the naturally occurring (RuS_2 and OsS_2) and converted ($OsAs_2$ and $RuAs_2$) pyrite-type structures. In Figure 5.2 (a), we compare the reflectivity spectra of RuS_2 and OsS_2. The spectra show

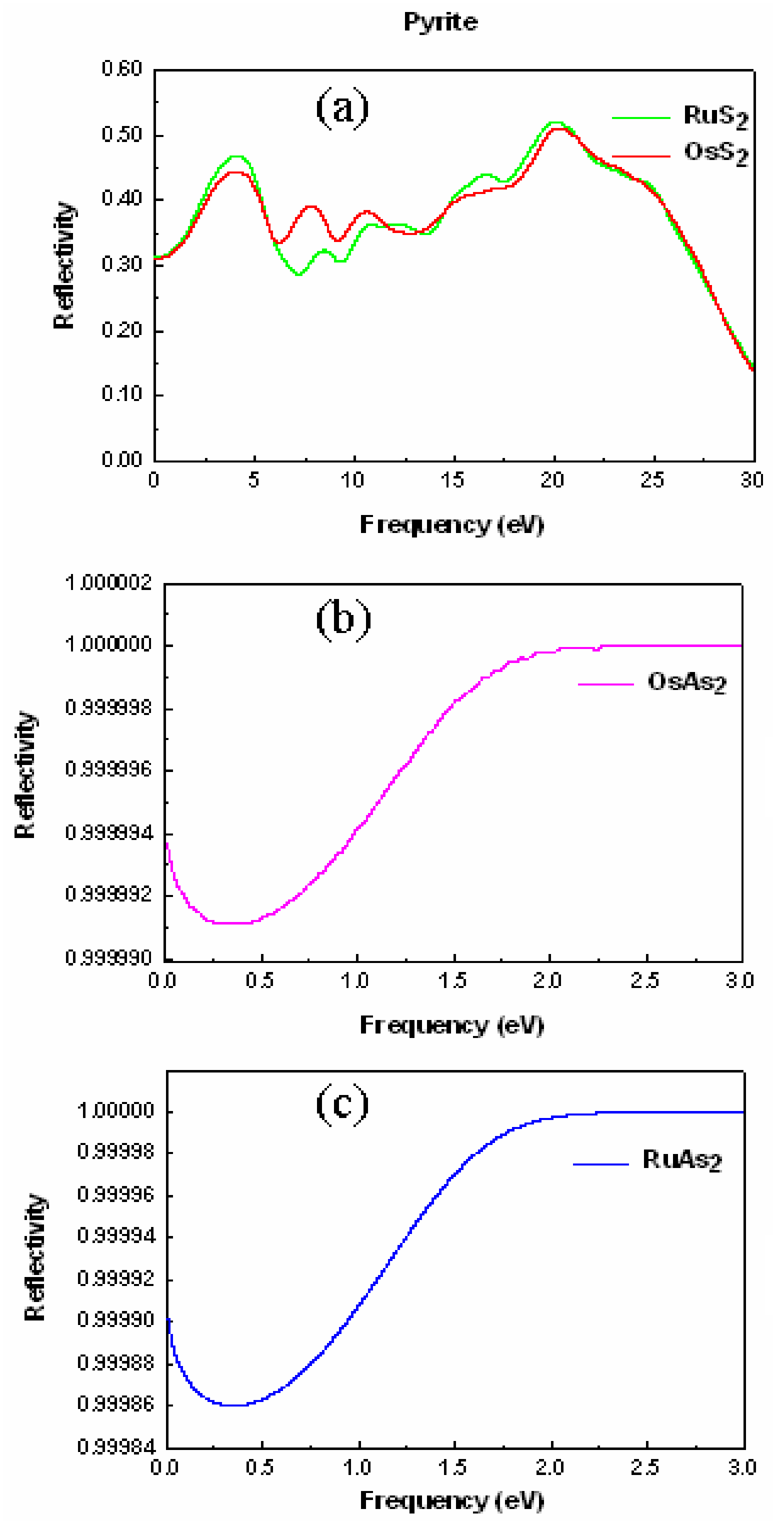

Real

Converted

Converted

Figure 5.2: Reflectivity spectra in units of 10^2 % against frequency (eV) for pyrite-type structures.

high reflectivity at lower and higher frequency respectively, where we observe higher peaks at around 3.5 eV corresponding to the reflectivity of about 47.0 % and 44.0 % for RuS_2 and OsS_2 respectively. A maximum reflectivity peak is observed at 20.0 eV with high reflectivity of about 51.0 % and 50.0 % for RuS_2 and OsS_2 respectively. However, at frequency energies higher than 20.0 eV, the reflectivity falls off rapidly with OsS_2 and RuS_2 showing similar reflection. The reflectivity spectra of the converted pyrite-type structures ($OsAs_2$ and $RuAs_2$) are shown in Figure 5.2 (b) and (c) respectively. We note a completely different behaviour between the naturally occurring and the converted reflectivity spectra for these pyrite-type structures. The converted pyrite-types show typical metallic reflectivity spectra with high reflectance at low frequency. Both spectra show reflection of 99.9 % at frequency of about 0.3 eV and fully reflected (100 %) at frequency of about 2.0 eV.

Figure 5.3 (a) shows the predicted absorption and reflectivity spectra against frequency energy for the marcasite-type structures. We see that both naturally occurring and converted marcasite-type structure show similar absorption curves. However, the naturally occurring marcasite-types have lower absorption than the converted phases and this is consistent with the stability as discussed in chapter 3 above. Unfortunately, no experimental optical spectra have been reported yet to our knowledge. The naturally occurring marcasite-type structures $OsAs_2$ and $RuAs_2$ predicts maximum absorption peak (of about 2.7×10^5 and 2.5×10^5 cm^{-1}) at frequency of about 8.0 eV and 9.0 eV respectively. At higher frequency of 15 eV, both structures have the same absorption of about 2.7×10^5 cm^{-1}. However, the converted marcasite-type structures OsS_2 and RuS_2 predict a maximum absorption of 3.6×10^5 and 3.8×10^5 cm^{-1} at frequency of about 15.0

eV respectively. The absorption spectra for the converted marcasite-type structures show more absorption than the naturally occurring structures at higher frequencies between 10.0 eV and 20.0 eV and the naturally occurring marcasite-type structures show more absorption at lower frequencies between 0.8 eV and 8.0 eV. Moreover, at frequency energies higher than 17.5 eV, the absorption falls off rapidly with OsS_2 and RuS_2 (converted structures) still showing more absorption than $OsAs_2$ and $RuAs_2$ (naturally occurring structures).

Figure 5.3 (b) shows the reflectivity spectra against frequency energy for both naturally occurring ($OsAs_2$ and $RuAs_2$) and converted (RuS_2 and OsS_2) marcasite-type structures. The naturally occurring phases of $RuAs_2$ and $OsAs_2$ show high reflectivity at energies above 5.0 eV. We observe two peaks at energies 6.6 eV and 10.2 eV for $RuAs_2$ which corresponds to the reflectance of about 47.0 % and 38.0 % respectively. A maximum peak at energy of about 9.5 eV for $OsAs_2$ corresponding to the reflectivity of 44.0 % is observed. The converted marcasite-type structures OsS_2 and RuS_2 are dominant (high reflectivity) at lower frequency (2 to 3 eV) and at higher energies (12 to 30 eV) than the naturally occurring structures $OsAs_2$ and $RuAs_2$. We observe maximum reflectivity peaks at lower frequency energies of about 4.2 eV and 3.0 eV which correspond to the reflectivity of about 47.5 % and 44.5 %. While a maximum reflectivity peak at higher frequency energies 19.5 eV and 19.8 eV enhancing the reflectivity of about 48.0 % and 46.0 % are observed for RuS_2 and OsS_2 respectively. Furthermore, at frequency energies higher than 20.0 eV, the reflectivity falls off rapidly with OsS_2 and RuS_2 still showing more reflection than $OsAs_2$ and $RuAs_2$. This suggests that the converted marcasite-type structures are less stable than the naturally occurring marcasite-type structures.

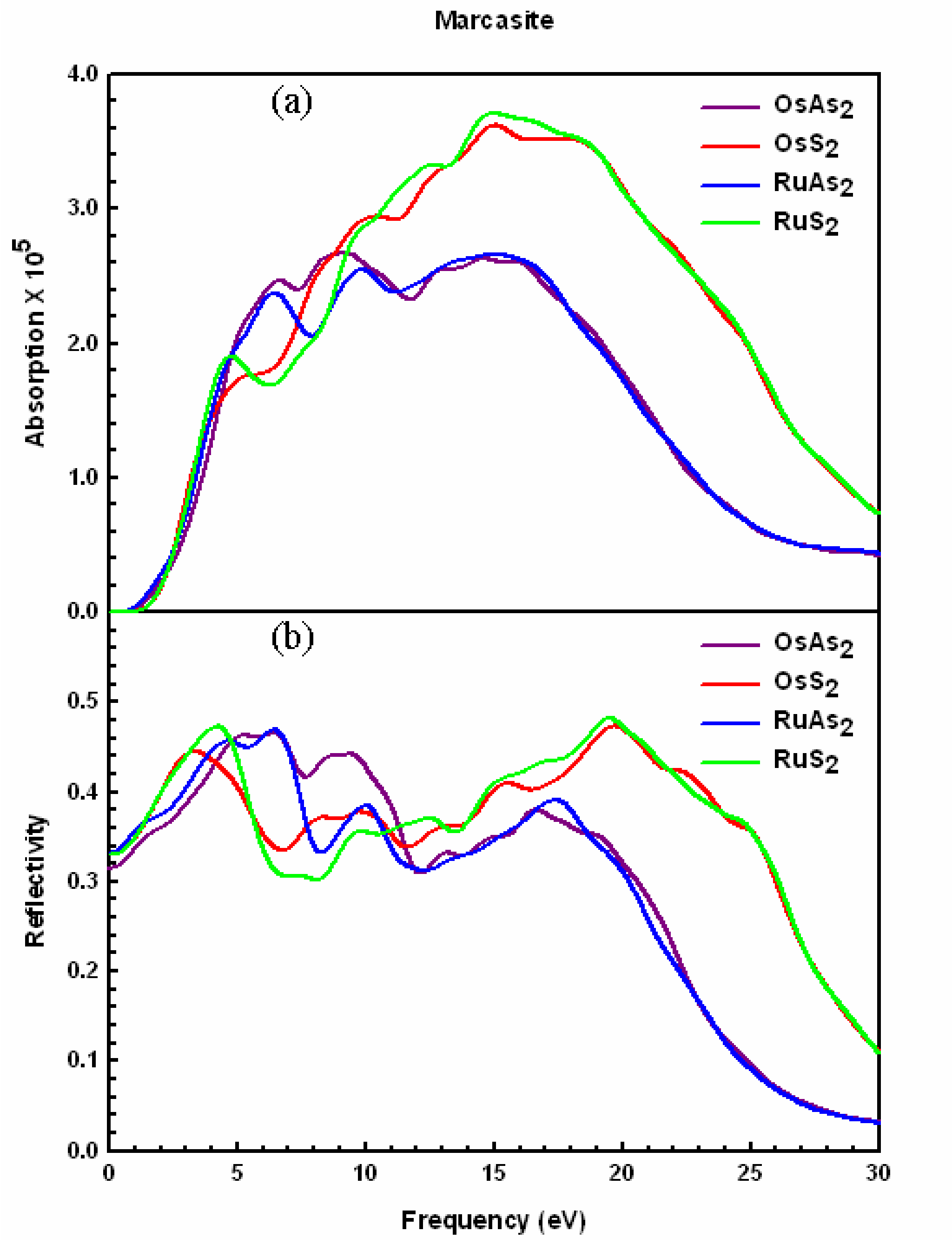

Figure 5.3: (a) Absorption coefficient in units of cm^{-1} and (b) reflectivity in units of 10^2 % against frequency energy for the marcasite-type.

5.2 Influence of pressure on the optical properties.

In this subsection, we discuss the influence of applied hydrostatic pressure on the absorption and reflectance spectra of both pyrite- and marcasite-type structures. The calculations were performed at varied pressure from -10 GPa to 10 GPa at the interval of 5 GPa. We will only discuss the naturally occurring structures in both pyrite- and marcasite-type.

Figure 5.4 shows the absorption and reflectance spectra for the naturally occurring pyrite-type structures. We see that our predicted absorption spectra show similar trends as the pressure is varied from -10 GPa to 10 GPa. Figure 5.4 (a) shows that as the pressure increases, the frequency energy is increased while the absorption remains constant for OsS_2, while for the RuS_2 is different. At frequency below 2.2 eV (0.5 X10^5 cm^{-1}), the 0 GPa curve show less frequency range than the other spectra. However, at high frequency above 3.0 eV (1.0 X 10^5 cm^{-1}), it gives similar trend as OsS_2. This implies that when varying the pressure, there is always a change in frequency energy for both RuS_2 and OsS_2 (i.e. as pressure is increased, the frequency increase while absorption remains unchanged).

Figure 5.4 (b) show reflectivity against frequency spectra for the pyrite-type RuS_2 and OsS_2 structures. We observe that the reflectivity spectra show similar trends as pressure is varied from -10 GPa to 10 GPa. The maximum reflectivity of about 52.0 % is observed, corresponding to higher frequency energy of about 20.0 eV for both RuS_2 and OsS_2 structures. We also notice that the low reflectivity of about 48.0 % and 44.0 % at lower frequency energy of about 3.0 eV is observed for RuS_2 and OsS_2 respectively. Again, we note a considerable difference in reflectivity with the 10 GPa being more dominant and -10 GPa being the lowest at frequency energy around 11.0 eV for both RuS_2 and OsS_2. Generally, as the reflectivity decays, the 10 GPa is more

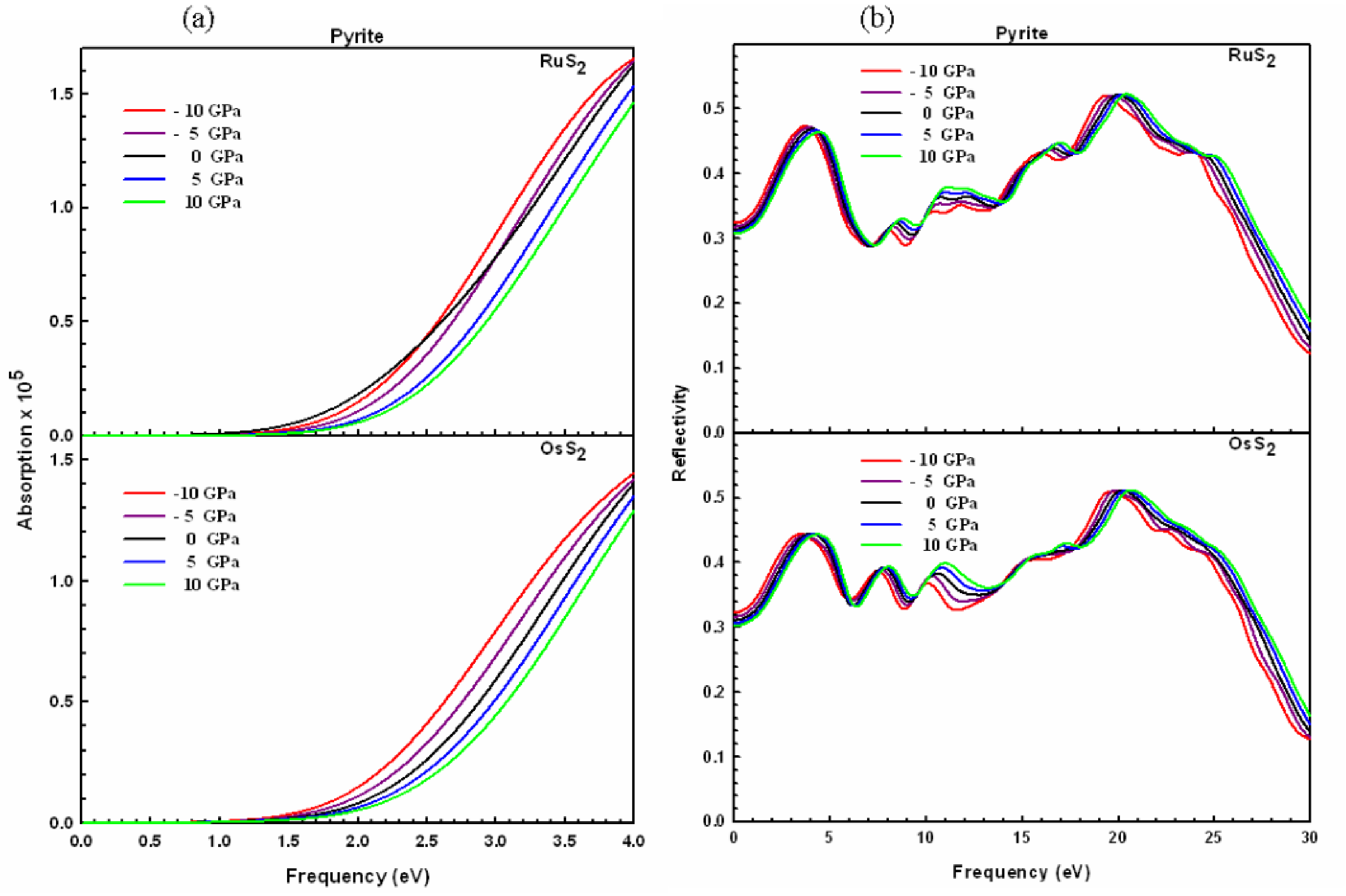

Figure 5.4: (a) Absorption coefficient in units of cm^{-1} and (b) reflectivity in units of 10^2 % against frequency for the pyrite-type at applied hydrostatic pressures.

dominant and as the reflectivity increases the -10 GPa becomes more dominant for both RuS_2 and OsS_2 structures.

Figure 5.5 shows absorption and reflectivity versus frequency energy spectra for the naturally occurring marcasite-type structures $OsAs_2$ and $RuAs_2$ as pressure is increased from -10 GPa to 10 GPa. It is evident from this Figure 5.5 (a) that the absorption peaks increases with increase in pressure. We observe that at higher pressure (10 GPa), the absorption spectra are dominant at frequency energy range above 5.0 eV for both $OsAs_2$ and $RuAs_2$.

The reflectivity spectra for the naturally occurring marcasite-type structures $OsAs_2$ and $RuAs_2$ at lower and higher pressures are shown in Figure 5.5 (b). We observe similar trend for the spectra with higher reflectivity of about 48.0 % at lower frequency energies up to 6.0 eV, where -10 GPa is dominant and 10 GPa being the lowest for both $OsAs_2$ and $RuAs_2$ structures. As the frequency increases to about 10.0 eV, reflectivity decreases to 44.0 % and 38.0 % for $OsAs_2$ and $RuAs_2$ respectively showing more dominance of 10 GPa with -10 GPa being the lowest.

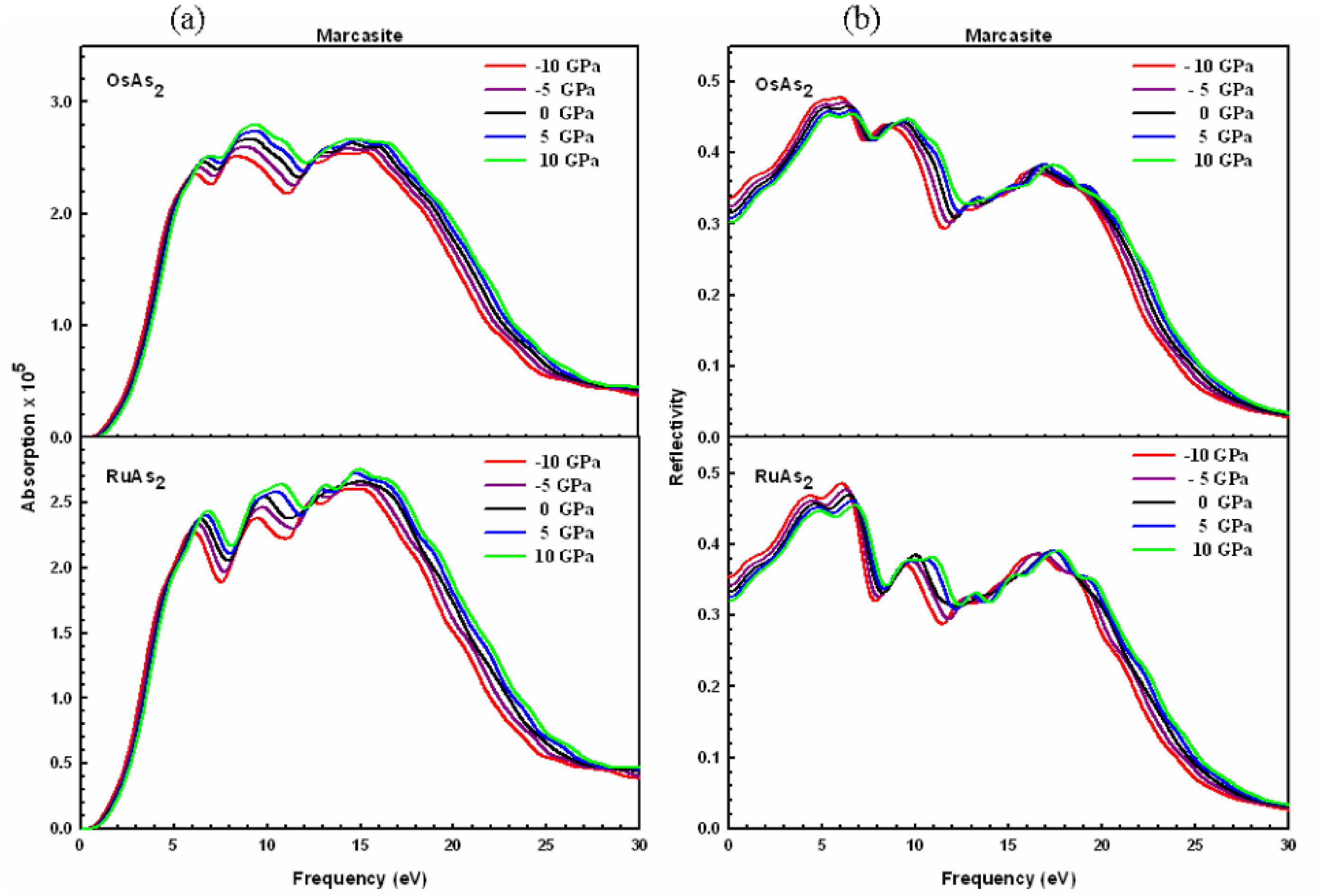

Figure 5.5: (a) Absorption coefficient in units of cm^{-1} and (b) reflectivity in units of 10^2 % against frequency for the marcasite-type at applied hydrostatic pressures.

CHAPTER 6

SUMMARY AND CONCLUSIONS

We have successfully employed the plane-wave pseudopotentials method from the two codes CASTEP and VASP to study the TMA ($OsAs_2$, $RuAs_2$) and TMS (OsS_2 and RuS_2) as pyrite- and marcasite-type structures.

Our predicted equilibrium lattice parameters are in good agreement with the experimental values. The heats of formation predict that the naturally occurring pyrite and marcasite structures are energetically favourable than the converted ones. Only RuS_2 pyrite structure agrees reasonably well with the experimental data and other structures have no experimental data for comparison.

Bond lengths were also investigated at equilibrium and the predictions for the naturally occurring pyrite and marcasite structures show a good correlation with the experimental values and there is no information on experimental data for the converted structures.

The equation of states (EOS) allowed us to determine the Bulk modulus which correlated well with predicted values from elastic constants. The Young's moduli and Shear moduli are also calculated which depict the converted pyrite-type structures to have less values compared to other structures. This leads the ratio of Bulk modulus to Shear modulus to predict the converted pyrite-type structures as ductile and all other structures show brittleness behaviour. It is evident from our predicted anisotropies that the naturally occurring structures are more stable as compared to the converted structures.

Furthermore, the hydrostatic pressure was applied and the structural properties i.e. lattice parameters, bond length and the internal parameters for the marcasite-type were most reduce as pressure is increased. The pyrite-type structures show similar trend for the lattice parameters on pressure variations plot which is the case for the marcasite-type structures. Bond lengths decrease as pressure is increased for the pyrite- and marcasite-type structures. All the pyrite-type structures show increasing internal parameter, u, as the pressure is increased except for $RuAs_2$. Whereas the marcasite-type structures show a decreasing internal parameter, u, as pressure is increased; the internal parameter, v, increases for converted structures and decreases for naturally occurring structures as pressure is increased.

The electronic properties were also predicted from the density of states and the corresponding energy band structures for the optimized structures at 0 GPa. There is a good correlation of the predicted energy band gap from the band structures and the energy gap from the DOS. Fortunately our predictions for RuS_2 structure on the band gap agrees well with previously reported data. The naturally occurring pyrite-type structures show a semiconducting behaviour, whereas the converted pyrite-type structures show a metallic behaviour. All the marcasite-type structures are predicted as semiconductors. Our results revealed that the naturally occurring structures are more stable as we observed energy gap at Fermi level.

Furthermore, we analysed bonding from the appearance of charge densities and how the charge is redistributed with respect to central atoms from the charge density differences. The plots of the charge densities and density differences showed different trends and distribution of charges for the pyrite- and marcasite-type structures. We noted a mixed bonding (i.e. covalent, ionic and weak ionic) for pyrite-type structures and only covalent and weak ionic bonding for marcasite-type structures.

The optical spectra for the TMA and TMS systems were investigated and we observed that the naturally occurring pyrite-type structures show less absorption compared to the converted pyrite-type structures and the spectra for the naturally occurring pyrite-type show similar trend with the experimental one for RuS_2. We also observed that there is less reflectivity for the naturally occurring than the converted pyrite-type structures. Furthermore, the naturally occurring marcasite-type structures showed more absorption at lower frequencies (0.8 to 8.0 eV) and the converted marcasite-type structures indicate more absorption at higher frequencies (10 to 20 eV). The reflectivity spectra for the naturally occurring marcasite-type structures are dominant at frequencies between 5 eV and 10 eV and the converted marcasite-type structures show higher reflectivity at higher frequencies above 10 eV.

We further observe that at a constant absorption, the frequency increases as pressure is increased for the naturally occurring pyrite-type RuS_2 and OsS_2. The reflectivity against frequency spectra at various pressures show similar trend with the 0 GPa spectrum for the naturally occurring pyrite-type RuS_2 and OsS_2. The naturally occurring marcasite-type structures $OsAs_2$ and $RuAs_2$ show that as pressure is increased, absorption and reflectivity increases at frequencies above 5 eV, depicting a similar trend as at 0 GPa.

APPENDIX A

PRESENTATIONS

1. Computational simulation study of marcasite group structure $OsAs_2$, 49th Annual Conference for South African Institute of Physics, University of Free State (2004).

2. Computational simulation studies of marcasite and pyrite group structures Materials Modelling Meeting, University of Limpopo (Turfloop Campus) (2005).

3. Computational simulation studies of marcasite and pyrite group structures ($OsAs_2$, $RuAs_2$, OsS_2 and RuS_2), 50th Annual Conference for South African Institute of Physics, University of Pretoria (2005).

4. Computational simulation study of marcasite and pyrite group structures ($OsAs_2$, $RuAs_2$, OsS_2 and RuS_2), Materials Modelling Meeting, University of Limpopo (Turfloop Campus) (2006).

5. Computational simulation studies of marcasite and pyrite group structures ($OsAs_2$, $RuAs_2$, OsS_2 and RuS_2), 51st Annual Conference for South African Institute of Physics, University of Western Cape (2006)

6. Computational studies of the properties of pyrite- and marcasite-type structures ($OsAs_2$, $RuAs_2$, OsS_2 and RuS_2), 52nd Annual Conference for South African Institute of Physics, University of the Witwatersrand (2007)

REFERENCES

Andersen O.K., Phys. Rev. B 12 (1975) 3060.

Ashcroft N. W. and Mermin N. D., Solid State Physics, Saunders College, Philadelphia (1976).

Bachelet G.B., Hamann D.R. and Schlüter M., Phys. Rev. B 26 (1982) 4199.

Becke A.D., Phys. Rev. A 38 (1988) 3098.

Bichsel R., Levy F. and Berger H., J. Phys. C: Solid State Phys. 17 (1984) L19.

Blöch P.E., Phys. Rev. B 50 (1994) 17953.

Born M. and Oppenheimer J.R., Ann. der Phys. 84 (1927) 457.

Brostigen G. and Kjeskus A., Acta Chem. Scand. 23 (1969) 2137.

Buerger M.J., Am. Mineralogist 16 (1931) 361.

Buerger M.J., Krist. 97 (1937) 504

Bullet D.W., J. Phys. C: Solid State Phys. 15 (1982) 6163.

Car R. and Parrinello M., Phys. Rev. Lett. 55 (1985) 2471.

Milman V., Winkler B., White J.A., Pickard C.J., Payne M.C., Akhmatskaya E.V., Nobes R.H., Int. J. Quant. Chem. 77 (2000) 895.

Chadi D.J. and Cohen M.L., Phys. Rev. B 8 (1973) 5747.

Chauke H.R., PhD Thesis, University of Limpopo (2005), Unpublished.

Chianelli R.R., IFP. 61 (2006) No. 4, 507.

Cohen M.L. and Heine V., Solid State Phys. 24 (1970) 37.

Cohen M.L. and Heine V., Solid State Phys. 24 (1970) 250.

Deer W.A., Howie R.A. and Zussman J., An introduction to them rock forming minerals, Longman, Harlow, UK (1992).

De Vita A., Gillan M. J., Lin J. S., Payne M. C., Štich I. and Clarke L. J. Phys. Rev. B 46 (1992) 12964.

Ennaoui A. and Tributsch H., Solar Cells 13 (1984) 197.

Ezzaouia H., Heindl R., Parsons R. and Tributsch H., J. Electroanal. Chem. 145 2 (1983) 79.

Fischer J.E., Phys. Rev. B 31 (1985) 4773.

Fermi E., Z. Phys. 48 (1928) 73.

Finklea S.and Cathey L., Acta Crystallogr. A 32 (1976) 529.

Fock V., Z. Phys. 61 (1930) 126.

Gibson M.C., Brand S. and Clark S.J., Phys. Rev. B 73 (2006) 125120.

Goodenough J.B., J. Solid State Chem. 3 (1971) 26.

Gou H., Hou L., Zhang J., Sun G., Gao L. and Gao F., State Key Lab. of Metastable Mat. Sci. and Tech., Department of Chem. Yanshan University (2007).

Grillo M.E., Smelyanski V., Sautet P., and Hafner J., Surface Sci. 439 (1999) 163.

Guittard R., Heindl R., Parsons R., Redon A.M. and Trri-butsch H., J. Electoanal. Chem. 11(1980) 401.

Hafner J., Wolverton C., Ceder G. and Bulletin MRS., 31 (2006) 659.

Hartree D.R., Proc. Cambridge. Philos. Soc. 24 (1928) 89.

Hann T., International Tables for Crystallography, 2nd Ed. Vol. A (1989).

Hohenberg P. and Kohn W., Phys. Rev. B136 (1964) 864.

Holse H.O., Pearson’ Handbook of Crystallographic Data, Journal of American Chemical Society. AA4. 22 (1968) 3284.

Holzwarth N.A.W., Harris S. and Liang K.S., Phys. Rev. B 32 (1985) 3745.

Howard R., MacIntosh mine, Transvaal, South Africa. BM AM 56: (1971) 1501, MM 47: (1983) 465, R: 821, ABI: 149.

Huang J.H. and Rowson N.A., Mineral Engineering 14 (2001) 1113.

Huang Ying-Sheng and Chen Yang-Fang, Phys. Rev. B 38 (1987) 7997.

Hulliger F., Nature (London) 200 (1963) 1064.

Hulliger F. and Mooser E., J. Phys. Chem. Solids 26 (1965) 429 –Prog. Solid State Chem. (1965b) 2330.

Hyde B. and O'Keeffe M., Aust. J. Chem. 49 (1996) 867.

Jaegermann W., Tributsh H., J. Appl. Electrochem. 13 (1983) 743.

Jennifer Banta, http://www.minerals.net/mineral/sulfides/pyrite. (2007).

Joannopoulos J.D. and Cohen M.L., J. Phys. C. 6 (1973) 1572.

Khan H.A., J. Phys. C: Solid State Phys. 9 (1974) 81.

Kleinmann L. and Bylander D.M., Phys. Rev. Lett. 48 (1982) 1425.

Koelling D.D. and Arbman G.O., J. Phys. F. 5 (1975) 2041.

Kohanoff J. and Gidopoulos N.I., Molecular Phys. and Quantum Chem. (ISBN 0 471 62374 1) 2 (2003) 532.

Kohn W. and Rostoker N., Phys. Rev. 94 (1954) 1111.

Kohn W. and Sham L.J., Phys. Rev. 140 (1965) 1133.

Korringa J., Physica 13 (1947) 392.

Kresse G. and Hafner J., Institute for Material Physics and Centre for Computational Materials Science, University Vienna A-1090 (2002).

Labanowski J. and Andzelm J., editors, Density Functional Methods in Chemistry, Springer- Verlag, New York (1991).

Lacroix M., Boutarfa N., Guillard C., Vrinat M. and Breysse M., Catal. 120 (1989) 473.

Li E.K, Johnson K.H., Eastman D.E. and Freouff J.L., Phys. Rev. Lett. 32 (1974) 470.

Linda P.J., Harrison N.M., and Gillan M.J., Phys. Rev. Lett. 80 (1998) 762.

Mattsson A.E., Schultz P.A., Desjarlais M.P., Mattsson T.R. and Leung K., Modelling

Simul. Mater. Sci. Eng. 13 (2005) R1.

Milmann, V., Winkler B., White J.A., Pickard C.J., Payne M.C., Akhmatskaya E.V. and Nobes R.H., International Journal of Quantum Chemistry 77 (2000) 895.

Monkhorst H.J. and Park J.D., Phys. Rev. B 13 (1976) 5188.

Murnaghan F.D., Proc. Natl. Acad. Sci. 30 (1944), 244.

Muscat J., Hung A., Russo S. and Yarovsky I., Phys. Rev. B 65 (2002) 054107.

Nordstrom D.K., Acid Sulphate Weathering, Spec. Pub. No. 10 Soil Sci. Amer., Madison WI (1982).

Ouyang C.Y., Europhys. Lett. 67 (2004) 28.

Pauling L. and Huggins M.L.Z., Krist. 87 (1934) 205.

Pasquarello A., Hybertsen, M.S. and Car R., Nature (London) (1998) 396.

Payne M.C., Teter M.P., Allan D.C. Arias T.A. and Joannopoulos J.D., Reviews of Modern Physics 64 (1992) 1045.

Pecoraro T.A. and Chianelli R.R., J. Catal. 67 (1981) 430.

Perdew J.P., Phys. Rev. B 33 (1986) 8822.

Perdew J.P., Burke K. and Ernzerhof M., Phys. Rev. Lett. 77 (1996) 3865.

Perdew J.P., Burke K. and Ernzerhof M., Phys. Rev. Lett. 78 (1997) 1396.

Perdew J.P., Chevary J.A., Vosko S.H., Jackson K.A., Perderson M.R., Singh D.J. and Fiolhais C., Phys. Rev. B 46 (1992) 6671.

Perdew J.P. and Wang Y., Phys., Rev. B. 33 (1986) 8800.

Perdew J.P. and Wang Y., Phys. Rev. B 45 (1991) 13244.

Phillip H.R., Phys Rev. B 16 (1977) 2896.

Phillips J.C., Phys Rev. 112 (1958) 685.

Raybaud P., Hafner J., Kresse G. and Toulhoat H.; J. Phys.: Condens. Matter, 9 (1997) 11107.

Saada D., Thesis, Phys. Comp.Technikon. 31 (2000)13k.

Schlegel A. and Wachter P., J. Phys. Chem: Solid State Phys. Vol. 9 (1976).

Segall M.D., Ab Initio Study of Biological Systems [LO] [RO, LE], BST (1997).

Segall M.D., Lindan L.D., Probert M.J., Pickard C.J., Haspin P.J., Clark S.J. and Payne M.C., J. Phys. Cond. Matt. 14(11) (2002) 2717.

Sithole H.M., PhD Thesis, University of the North (2000), Unpublished.

Sithole H.M., Ngoepe P.E. and Wright K., Phys. Chem Minerals 30 (2003) 615.

Slater J.C., Phys Rev. 35 (1930) 210.

Sutar O., Pearson's Handbook of Crystallographic Data, Canadian Journal of Chemistry (American Group) 45 (1967) 1391.

Sutarno O., Knop O. and Reid K.I.G., Can. J. Chem. 45 (1967) 1391.

Temmerman W.M., Durham P.J. and Vaughan D.J., Phys. Chem. Minerals 20 (1993) 248.

Thomas L.H., Proc. Cambridge. Philos. Soc. 23 (1927) 542.

Toulhoat H., Raybaud P., Kasztelan S., Kresse G. and Hafner J., Symp. On Advances and Apllications of Computational Chemical Modelling to Heterogeneous Catalysis (San Francisco, CA) (New York: American Chemical Society) (1997).

Tossel J.A., Chem. Phys. 66 (1977) 5712.

Tossel A., Vaughan D.J. and Burdett J.K., Phys. Chem. of Minerals Vol. 7 (Berlin: Springer) (1977) 177.

Vanderbilt D., Phys. Rev. B 41 (1990) 7892.

Vaterlaus H.P., Bichsel R., Le'vy F., and Berger H., J. Phys. C: Solid State Phys. (1985) 63.

Http://en.wikipedia.org/wiki/marcasite (2007).

Wilson J.A., Adv. Phys. 21 (1972) 143.

Wimmer E., Krakauer H. and Freeman A.J., in Electronics and Electron Physics, ed. by Hawkes P.W., Academic Press, Orlando Vol. 65 (1985) 357.

Xiong K., Robertson J., Gibson M.C. and Clark S.J., App. Phys. Lett. 87 (2005) 183505.

Yin M. T. and Cohen M. L., Phys. Rev. B 25 (1982) 7403.

Zhao G.L., Callaway J. and Hayashibara M., Phys. Rev. B 48 (1993) 15781.